공학박사학위논문

전기자동차 다중 레벨 열관리 시스템과 운영 전략에 관한 연구

Study on the multi-level thermal management system in electric vehicle and its operating strategies

2023 년 2 월

서울대학교 대학원

기계공학부

이 상 욱

전기자동차 다중 레벨 열관리 시스템과 운영 전략에 관한 연구

Study on the multi-level thermal management system in electric vehicle and its operating strategies

지도교수 김 민 수

이 논문을 공학박사 학위논문으로 제출함

2022 년 10 월

서울대학교 대학원
기계공학부
이 상 욱

이상욱의 공학박사 학위논문을 인준함

2022 년 12 월

위 원 장 : ________________ (인)

부위원장 : ________________ (인)

위 원 : ________________ (인)

위 원 : ________________ (인)

위 원 : ________________ (인)

Ph.D. Dissertation in Mechanical Engineering

Study on the multi-level thermal management system in electric vehicle and its operating strategies

전기자동차 다중 레벨 열관리 시스템과 운영 전략에 관한 연구

February 2023

Graduate School of Mechanical Engineering
Seoul National University

SANGWOOK LEE

Abstract

Study on the multi-level thermal management system in electric vehicle and optimization of its operating strategies

Sangwook Lee
Department of Mechanical Engineering
The Graduate School
Seoul National University

As many global regulations restricts CO_2 emission and fuel economy of automobiles, electric vehicles (EVs) have attracted great attention as a promising zero-emission vehicle. However, EVs suffer from the range loss at cold ambient temperature due to increased power consumption on cabin heating and low performance of lithium-ion battery. Therefore, heat pumps are widely adopted as an energy-efficient heating device replacing the positive temperature

coefficient heater. However, the performance of heat pumps deteriorates at low ambient temperature so that the waste heat from electric devices is recovered to supplement the insufficient heating capacity in winter. In this study, I suggest a multi-level thermal management system (MLTMS), which utilizes the subdivided temperature levels recovering the waste heat.

Firstly, the effect of temperature levels on the heat pump system was investigated. The vapor injection technique enables the recovery of waste heat at an intermediate temperature level. As the refrigerant absorbs waste heat at intermediate temperature level, larger heating capacity is provided to the cabin. Experiments were conducted in three modes: non-waste heat recovery, conventional waste heat recovery, and multi-level waste heat recovery. The performance of each mode was investigated under different operating conditions, including the ambient air temperature, compressor speed, and amount of waste heat. Results show that multi-level waste heat recovery augments heating capacity up to 72.5% in the coldest condition of -20 °C while maintaining the temperature of the energy storage system within an appropriate operating range.

Likewise, the waste heat recovery at high temperature level was evaluated. The floating loop manages the thermal state of power electronics and electric motors by utilizing the liquid refrigerant at the condenser outlet. This loop recovers the waste heat in winter and enhances the cooling performance in summer through the superior cooling performance of evaporative heat transfer. Configurations of heat pump and thermal management system are presented with operating schematic in summer and winter. To verify the performance of the suggested system, the heat pump and thermal management system model is established based on experimentally validated heat pump component models and electric device models. The result shows that the heat pump system utilizing a floating loop can save power consumptions in winter up to 27.7% and 5.8% in summer while maintaining the thermal state of electric devices within the appropriate range.

Secondly, the performance of multi-level thermal management system was estimated from the cold-start condition. As aforementioned results demonstrate, the temperature level, at which the waste heat is recovered, affects the performance of the heat pump system. However, the conventional waste heat recovery strategy (WHRS) simply depends on one temperature level, even though the optimal temperature level changes depending on the operating conditions. The performance of the WHRSs, recovering heat at different temperature levels, was investigated. Temperature levels of WHRSs were divided into three: conventional (low), multi-level (intermediate), and direct (high). Experiments were conducted to examine the dynamic behavior of the heat pump system, and a transient model was established based on the experimental data. The electric device thermal model was consolidated into the integrated thermal management system model. The model evaluated heating performance and power consumption of WHRSs from various start-up conditions. Results show that the optimal WHRS saves the power consumption up to 13 % compared with conventional WHRS at the ambient temperature of -20°C under Artemis highway driving profile.

Thirdly, as the MWHR depends on the vapor injection technique, the port hole design critically affects the system performance. However, none of existing injection port is designed to be used with MWHR. The effect of port design on the MWHR system was investigated. A novel injection model was established, considering the continuously increasing pressure in the injected chamber and jet impingement behavior. The scroll compressor model with the injection process was integrated into a transient heat pump model. The effect of injection port location and size were investigated with the integrated thermal management system model under cold-start conditions. The optimal port hole design was suggested as the dual-port at 600 ° with a radius of 2 mm from the perspective of total energy consumption. We anticipate that this study proposes a reference data and an optimization methodology in designing the port hole in the MWHR system.

Lastly, an active battery thermal management strategy (BTMS), which uses the secondary loop in an electric vehicle heat pump, is suggested. When an energy storage system (ESS) operates in cold conditions, the power and capacity of the battery critically fade with high internal resistance. Therefore, appropriate BTMS is essential to prevent severe driving range loss at low ambient temperatures. To derive optimal BTMS, the trade-off between performance enhancement by ESS heating and additional energy consumption on the heating needs to be evaluated from the perspective of an integrated thermal management system (ITMS). We established a battery thermal model by combining a pack-level thermal model and a cell-level performance model. The battery thermal model was integrated with a transient heat pump model to estimate the performance of three BTMSs: self-heating, active heating, and heat recovery. Active heating of the battery augmented the driving range of EV up to 18.8%, whereas the heat recovery saved state-of-charge (SOC) decrease in non-depleted conditions. Furthermore, battery preheating with the heat pump achieved a temperature rise of 20 °C within an hour, consuming 38.4 % less power of the battery, compared with electric heater preheating.

I expect that this study provides an insight on MLTMS and promote broad adoption of MWHR as a solution to EV range reduction.

Keyword: Electric vehicle (EV), Integrated thermal management system, Vapor injection technique, Temperature level subdivision, Multi-level heat pump, Waste heat recovery, Capacity augmentation, Cold-start

Identification Number: **2018-28030**

Contents

Abstract ii

Contents viii

List of Figure...xi

List of Table ...xix

Nomenclature...xx

Chapter 1. Introduction ...1

1.1. Background of the study...1

1.2. Literature survey...8

1.2.1. Adoption of heat pumps in electric vehicle ... 8

1.2.2. Recent technologies to improve heating performance of EVHP. 12

1.2.3. Integrated thermal management system (ITMS)... 16

1.3. Objectives and scopes...19

Chapter 2. Effect of temperature level on the waste heat recovery performance ...23

2.1. Introduction ...23

2.2. Waste heat recovery at intermediate temperature level ...27

2.2.1. Experimental setup... 27

2.2.2. Accuracy of measuring devices and uncertainty analysis ... 35

2.2.3. Test procedure ... 38

2.2.4. Results and discussion... 40

2.3. Waste heat recovery at high temperature level 57
2.3.1. System description 57
2.3.2. Model description... 65
2.3.3. Results and discussion.. 83
2.4. Summary...96
Chapter 3. Multi-level waste heat recovery system 99
3.1. Introduction 99
3.2. Model description 101
3.2.1. Scroll compressor modeling.. 101
3.2.2. System modeling 113
3.2.3. Electric device modeling.. 123
3.3. Results and discussion 126
3.4. Summary..142
Chapter 4. Port design optimization of multi-level waste heat recovery system..144
4.1. Introduction 144
4.2. Results and discussion 146
4.3. Summary..161
Chapter 5. Active battery thermal management strategy 163
5.1. Introduction 163
5.2. Battery model descprtion 163
5.2.1. Battery performance experiment at low temperatures............... 164
5.2.2. Battery heating strategies 172

5.3. Results and discussion 175

5.4. Summary 186

Chapter 6. Concluding remarks 188

Reference 192

Abstract (in Korea) 219

List of Figure

Figure 1.1 (a) Passenger car CO_2 emission standards [14] and (b) global EV vehicle stock by transport mode [13] 2

Figure 1.2 Effect of ambient temperature on (a) EV energy consumption [20] and (b) available range [21] 5

Figure 1.3 Performance of EV heat pump system at different ambient temperature [44]...11

Figure 1.4 Technologies to augment the heating capacity: (a) waste heat recovery [51] and (b) vapor injection technique [62] 15

Figure 2.1 Simplified system configuration: (a) conventional waste heat recovery system (CWHR) and (b) multi-level waste heat recovery (MWHR) system with vapor injection compressor..................... 31

Figure 2.2 Pressure-enthalpy diagram of heat pump system with CWHR and MWHR modes. 32

Figure 2.3 Schematic diagram of experimental apparatus 33

Figure 2.4 Experimental apparatus in psychrometric calorimeter................ 34

Figure 2.5 Performance of the non-WHR, CWHR, MWHR system with different outdoor air temperatures; (a) heating capacity and power consumption of compressor, (b) total and injected mass flow rate (with compressor speed of 4,000 rpm and waste heat amount of 1 kW) 49

Figure 2.6 Performance of the non-WHR, CWHR, MWHR system with different outdoor air temperatures; (b) COP and (c) condensing, evaporating, and intermediate pressures (with compressor speed of 4,000 rpm and waste heat amount of 1 kW). 50

Figure 2.7 Temperature trend of (a) coolant passing through WHX and estimated ESS temperature and (b) air provided in cabin with different outdoor temperature in non-WHR, CWHR, and MWHR mode (with compressor speed of 4,000 rpm and waste heat amount of 1 kW).amount of 1 kW).. 51

Figure 2.8 Performance of the non-WHR, CWHR, MWHR system with different compressor speed; (a) heating capacity and power consumption of compressor and (b) COP (with ambient temperature of -10°C and waste heat amount of 1 kW).............. 52

Figure 2.9 Performance of the non-WHR, CWHR, MWHR system with different compressor speed; (a) condensing, evaporating, and intermediate pressures, and (b) total and injected mass flow rate (with ambient temperature of -10°C and waste heat amount of 1 kW). 53

Figure 2.10 Performance of the non-WHR, CWHR, MWHR system with different amount of waste heat; (a) heating capacity and power consumption of compressor and (b) COP (with ambient temperature of -10°C and compressor speed of 4,000 rpm). 54

Figure 2.11 Performance of the non-WHR, CWHR, MWHR system with different amount of waste heat; (c) condensing, evaporating, and intermediate pressure, and (d) total and injected mass flow rate (with ambient temperature of -10°C and compressor speed of

4,000 rpm).. 55

Figure 2.12 Temperature change of (a) coolant passing through WHX and estimated ESS temperature and (b) air provided in cabin with waste heat amount in non-WHR, CWHR, and MWHR modes (with ambient temperature of -10°C and compressor speed of 4,000 rpm).. 56

Figure 2.13 Schematic of (a) conventional heat pump and thermal management system and (b) floating loop heat pump and thermal management system.. 62

Figure 2.14 System configuration and fluid flows of CHPTMS when operating in (a) summer and (b) winter and FLHPTMS when operating in (c) summer and (d) winter 63

Figure 2.15 System configuration and fluid flows of (a) CRLTMS when operating in (b) summer and (c) winter 64

Figure 2.16 Compressor model validation in (a) power consumption, (b) mass flowrate and with 10% error line 77

Figure 2.17 Thermal schematic of (a) motor and (b) battery 78

Figure 2.18 Validation results of (a) averaged battery temperature and (b) motor coil temperature with 10% error line................................ 79

Figure 2.19 Flowchart of the simulation in (a) CHPTMS and (b) FLTMS ... 80

Figure 2.20 System performance and thermodynamic state of CHPTMS, FLTMS and CRLTMS with different ambient temperature condition in winter: (a) Total power consumption, (b) mass flowrate of compressor 90

Figure 2.21 System performance and thermodynamic state of CHPTMS, FLTMS and CRLTMS with different ambient temperature condition in winter: (a) pressure and (b) motor coil temperature 91

Figure 2.22 PEEM evaluation as a heat source with (a) exergy transfer rate of CHPTMS, FLTMS and CRLTMS and (b) battery temperature of CHPTMS and FLTMS in winter 92

Figure 2.23 System performance and thermodynamic state of CHPTMS, FLTMS and CRLTMS with different ambient temperature condition in summer: (a) compressor power consumption, (b) temperature of air provided in cabin 93

Figure 2.24 System performance and thermodynamic state of CHPTMS, FLTMS and CRLTMS with different ambient temperature condition in summer: (a) heat exchanger efficiency and (b) motor coil temperature 94

Figure 2.25 Thermodynamic state of CHPTMS, FLTMS and CRLTMS in summer: (a) mass flowrate of compressor (upper) and chiller (lower) and (b) pressure of condenser (upper) and evaporator (lower).. 95

Figure 3.1 Two multi-level heat pump system on pressure-enthalpy diagram: (a) two-stage, (b) vapor-injection... 107

Figure 3.2 Schlieren experiment (a) apparatus and (b) schematic diagram. 108

Figure 3.3 Schlieren image of (a) initial injection process and (b) continuously decaying injection flow due to continuously increasing pressure in the chamber 109

Figure 3.4 Validation results of scroll compressor with injection: (a) total mass flow rate and (b) injected mass flow rate 110

Figure 3.5 Validation results of scroll compressor with injection: (a) compressor work, and (b) discharge temperature 111

Figure 3.6 Scroll compressor with two injection holes in (a) enlarged size and (b) normal size 112

Figure 3.7 Refrigerant properties and its notation at each node in heat exchanger 119

Figure 3.8 Flowchart of the simulation in (a) CHPTMS and (b) FLTMS ... 120

Figure 3.9 Dynamic behavior of heat pump experiment and model estimation of MWHR; (a) pressure, (b) mass flow rate, and (c) temperature 121

Figure 3.10 Schematic of motor model; (a) thermal components and structure of electric motor and (b) thermal resistance circuit of motor..... 125

Figure 3.11 Transient behavior of heat pump system in CWHR, MWHR, and DWHR mode; (a) pressure, (b) heat transfer rate. Heat pump operated with constant vehicle speed of 100 km/h, ambient temperature of 0 °C, and 100% recirculation of cabin air. (evaporating pressure of DWHR and MWHR are overlapped.) 135

Figure 3.12 Transient behavior of heat pump system in CWHR, MWHR, and DWHR mode; (a) mass flow rate, and (b) PEEM coolant temperature. Heat pump operated with constant vehicle speed of 100 km/h, ambient temperature of 0 °C, and 100% recirculation of cabin air.. 136

Figure 3.13 Power consumption by (a) components and (b) total power consumption of heat pump system at instantaneous and time averaged domain in CWHR, MWHR, and DWHR mode. 137

Figure 3.14 Transient behavior of heat pump system with different vehicle speed; (a) total mass flow rate (b) recovered heat from PEEM (c) time averaged power consumption. 138

Figure 3.15 Transient behavior of total power consumptions at different ambient air temperatures in each mode..................................... 139

Figure 4.1 Scroll wrap with injection ports with (port angle from 360° to 780°) 153

Figure 4.2 Schematic of different waste heat recovery systems................. 154

Figure 4.3 Scroll wrap with injection ports with (port angle from 360° to 780°) 155

Figure 4.4 Time-averaged power consumption of MWHR with different (a) port size and (b) port angle. (The port was located at 480 ° and had radius of 2 mm in (a) and (b), respectively.) 156

Figure 4.5 System performances with different port geometries: (a) injected mass flow rate and (b) absorbed heat from PEEM with various port sizes; (c) injection pressure and (d) temperature of coolant from PEEM with various port angles.. 157

Figure 4.6 System performance variation with different port geometries: (a) time-averaged power consumption and cross point and (b) injected mass flow rate with different port areas; and (c) time-averaged power consumption and cross points and (d) injection pressure and suction mass flow rate with different port angles. 158

Figure 4.7 The effect of vehicle velocity on the (a) power consumption and (b) cross points. 159

Figure 5.1 Battery capacities with different temperature and power consumptions: (a) 0.2W, (b) 0.5 W, (c) 1 W, and (d) 2 W.......... 169

Figure 5.2 Schematic diagram of (a) thermal components and (b) thermal resistance circuit of ESS 170

Figure 5.3 Validation results of the ESS thermal model. Minimum and maximum temperatures of the ESS were compared, and bumpy profiles were obatined due to the discrete time steps in the measurement. (RMSE: root mean square error, AME: absolute mean error)... 171

Figure 5.4 Schematic diagram of three BTMSs; (a) self-heating, (b) active heating, and (c) heat recovery.. 174

Figure 5.5 System performances of three BTMSs: (a) ESS temperaure, (b) heat transfer and generaion, (c) operating pressure, and (d) power consumption. (Soaking temperautre: -15 °C, initial SOC: 0.65, vehicle speed: 100 km/h) 182

Figure 5.6 Battery status of three BTMSs: (a) cell voltage and (b) SOC and accumulated current... 183

Figure 5.7 System performances of three BTMSs: (a) SOC and accmulated current, (b) cell voltage, (c) power consumption, and (d) ESS temperature. (Soaking temperautre: -5 °C, initial SOC: 0.6, vehicle speed: 50 km/h)... 184

Figure 5.8 Preheating performance of heat pump system: (a) power consumption, heat transfer, and COP and (b) operating pressure and ESS temperaure 185

List of Table

Table 1.1 Thermal requirements of each EV components 7

Table 2.1 Accuracies of measuring devices 37

Table 2.2 Experimental conditions 39

Table 2.3 Thermal properties of materials in TMS 81

Table 2.4 System modeling conditions 82

Table 3.1 Correlations and conditions used in heat transfer coefficient calculation 122

Table 3.2 Averaged speed and duration of standardized driving profiles 140

Table 3.3 Optimal WHRSs and power savings of different driving profiles and ambient temperatures 141

Table 4.1 Simulation conditions 160

Nomenclature

a	thermal coefficient of resistance [1/°C]
A_{du}	DuBois body surface area [m^2]
Bo	boiling number [-]
B	magnetic flux density [T]
C	clearance volume ratio
C_d	drag coefficient [-]
c_p	specific heat capacity [J/kg]
d_h	hydraulic diameter [m]
$\mathrm{Dn_m}$	Dean number
E	energy [J]
$\boldsymbol{f}$	external force vector [N]
F	Faraday constant [A/mol]
F_l	fin length [m]
F_p	fin pitch [m]
G	mass flux [m^2/s]
h	specific enthalpy [kJ/kg]
h_m	mass transfer coefficient [kg/s·m^2]
h_t	heat transfer coefficient [W/m2K]
I	current [A]
Δi_l	latent heat [J/kg]
j	Colburn j-factor [-]
k	polytropic index

k_f	thermal conductivity of fin [W/m·K]
k_h	hysteresis coefficient [-]
k_e	eddy current coefficient [-]
L	tube length [m]
L_l	louver length [m]
L_p	louver pitch [m]
Le	Lewis number
M	metabolic heat generation in each passenger [W/person]
$\dot{m}$	mass flow rate [kg/s]
n	polytropic index [-]
N_{CB}	convective boiling number
Nu	Nusselt number [-] ($= hL/k$)
P	pressure [Pa]
Pr	Prandtl number [-] ($= c_p\mu/k$)
$\dot{Q}$	total heat transfer rate [W]
$\boldsymbol{q}$	heat conduction [W]
q''	heat flux [W/m^2]
R	electrical resistance [K/W]
Re	Reynolds number [-] ($= \rho v L/\mu$)
Δs	entropy change [J/kg·K]
T	temperature [°C]
T_d	tube depth [m]
T_p	tube pitch [m]
UA	overall heat transfer coefficient [W/K]

V	volume of refrigerant [m^3]
V_{swept}	swept volume [m^3]
$\dot{W}$	electirc work of compressor [W]
w	absolute humidity [kg/kg]
$\mathrm{X_{tt}}$	Lockhart-Martinelli parameter
x	vapor quality [-]

Greek Letters

α	thermal diffusivity [m^2/s]
β	volumetric thermal expansion coefficient [K^{-1}]
γ	aspect ratio
η_m	mechanical efficiency
η_v	volumetric efficiency
η_f	fin efficiency
μ	viscosity [Pa/s]
ν	kinematic viscosity [m^2/s]
$\boldsymbol{\sigma}$	stress vector [Pa]
ρ	density [kg/m^3]
ω	rotor frequency [Hz]

Subscripts

0	reference state

a	air
amb	ambient
$cool$	coolant
ch	cooling jacket channel
d	discharge
dw	downstream
eqv	equivalent
g	gas state
inj	injected
l	liquid state
w	winding
ref	refrigerant
rev	reversible
s	suction
sa	saturation
up	upstream

Abbreviations

BMS	battery management system
BTMS	battery thermal management strategy
COP	coefficient of performance
CHP	conventional heat pump

EEV	electric expansion valve
ESS	energy storage system
EV	electric vehicle
IDHX	indoor heat exchanger
ITMS	integrated thermal management system
PTCH	positive temperature coefficient heater
PEEM	power electronics and electric motors
SOC	state of charge
WEG	water/ethylene glycol
WHX	waste heat exchanger
WHRS	waste heat recovery strategy
CWHR	conventional waste heat recovery
MWHR	multi-level waste heat recovery
DWHR	direct waste heat recovery
CHPTMS	conventional heat pump and thermal management system
FLTMS	floating loop heat pump and thermal management system
CRLTMS	complete refrigerant loop heat pump and thermal management system
AHTMS	active heating thermal management strategy
SHTMS	self-heating thermal management strategy
HRTMS	heat recovery thermal management strategy

Chapter 1. Introduction

1.1. Background of the study

Intergovernmental Panel on Climate Change (IPCC) reported that the averaged temperate of the globe have risen 1 °C since the pre-industrial era [1]. IPCC declared that the global warming was caused by cumulative CO_2 emission from human activities and must be limited to 1.5 °C to prevent climate-related risks. As shown in Figure 1.1 (a), many national authorities enacted policies [2] on CO_2 emission [3–5] from various sector, among which transportation sector occupies 27% of total emission [6]. The regulations on the transportation restricts the CO_2 emission values as 59 g/km in 2020 [7] based on the new European driving cycle (NEDC), corresponding to the mileage of 39.3m/L, which cannot be satisfied with conventional internal combustion engine vehicle (ICEV) alone. To avoid huge amount of monetary penalty or benefit from the credits, automotive industry accelerates the electrification of vehicles. Along with regulations, policy incentives are stimulating the purchase of zero-emission vehicle [2, 8–12]. As presented in Figure 1.1 (b), global EV stock reached 10 million on the world's road at the end of 2020 [13]. Furthermore, the registration of EV shows rapidly increasing trend, which increased by 41%

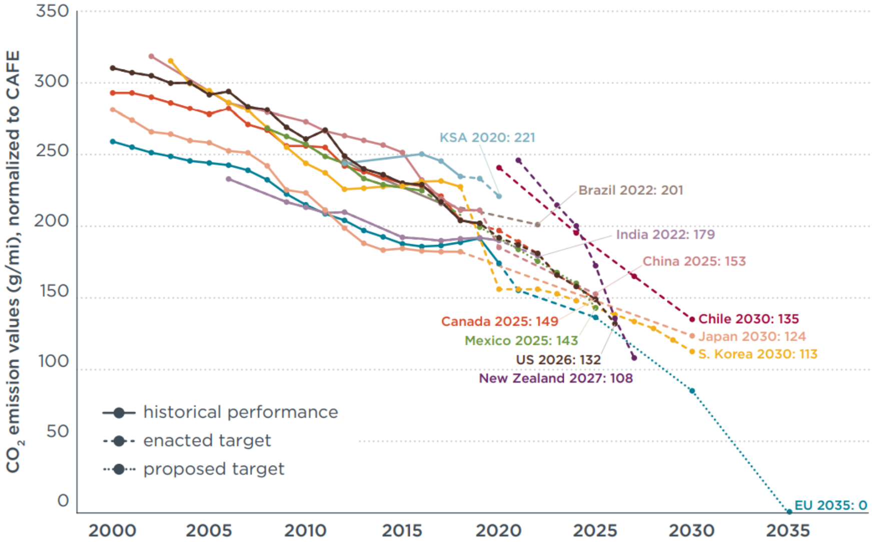

(a)

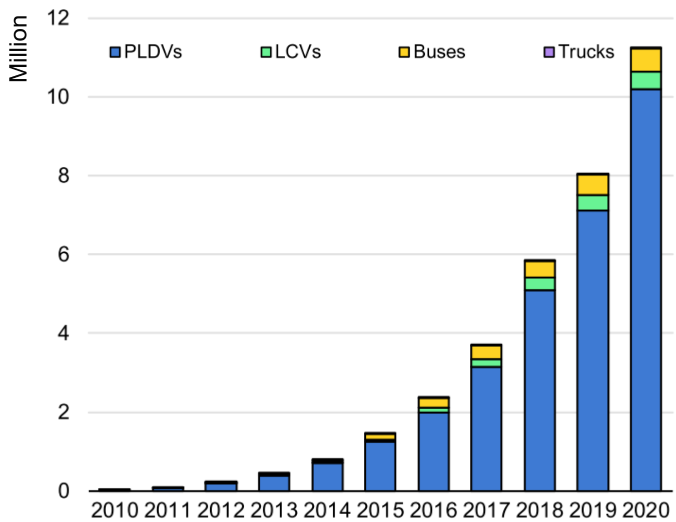

(b)

Figure 1.1 (a) Passenger car CO_2 emission standards [14] and (b) global EV vehicle stock by transport mode [13] in 2020, and is expected to soar with leveraged momentum of the extensive global supports [9, 15].

Among various zero- and low-emission vehicles (ZLEV), EV emerges a most prominent ZLEV, having advantages such as instantaneous control through immediate response of motor, high efficiency operation with less losses, high torque at the low speed, and simplified power train structure [16]. However, there are several problems preventing wider spread of EV. First of all, the main difference between EV and ICEV lies at the energy density of different power sources; lithium ion-battery and fossil fuels, respectively. As the gasoline and diesel have approximately 20 times higher power and energy density than the lithium-ion battery [17, 18], EV requires much larger and heavier battery and related systems. The powertrain in ICEV only costs one fourth of that in EV with the battery system occupying 42% of total manufacturing cost [19]. It means that the EV cannot compete with ICEV in the aspect of price without subsidy from government.

Apart from the price, the driving range of EV is limited by the total amount of energy carrier, lithium-ion battery, with low energy density. This limited driving range diminishes even shorter when the additional energy is required in cabin heating or cooling. Conventionally, ICEV utilizes the waste heat from internal combustion engine in the cabin heating at low ambient temperatures.

However, EV lacks abundant waste heat from powertrain, which consists of motor and inverter having a high efficiency. As shown in Figure 1.2, the electric energy from the lithium-ion battery is consumed in cabin conditioning, resulting in shorter driving range. Range anxiety represents a fear that insufficient range could strand the passenger, which still refrains potential customers from purchasing EVs [20]. The range problem even deteriorates in severely cold outdoor conditions with extra power consumption of positive temperature coefficient (PTC) heater. Lohse-Busch et al. [21] and Jeffers et al. [22] presented that range reduction problems of Nissan Leaf and Ford Focus under ambient air temperature of -7°C and -5°C condition reach 48% and 47% in urban dynamometer driving schedule (UDDS) cycle. Leighton [23] conducted a similar investigation on the mid-sized sedan, in which the driving range decreases by 53% under -12°C ambient air condition. Heat pump is suggested as a solution to these problems [24–26] which shows that heat pump requires less power consumption up to 71% than PTC heater, which has a maximum efficiency of 1.

On the other hand, EV has entirely different powertrain with ICEV in the aspect of thermal management. The proper operating temperature of lubricant oil in an internal combustion engine is around 100 °C - 110 °C [27, 28], whereas

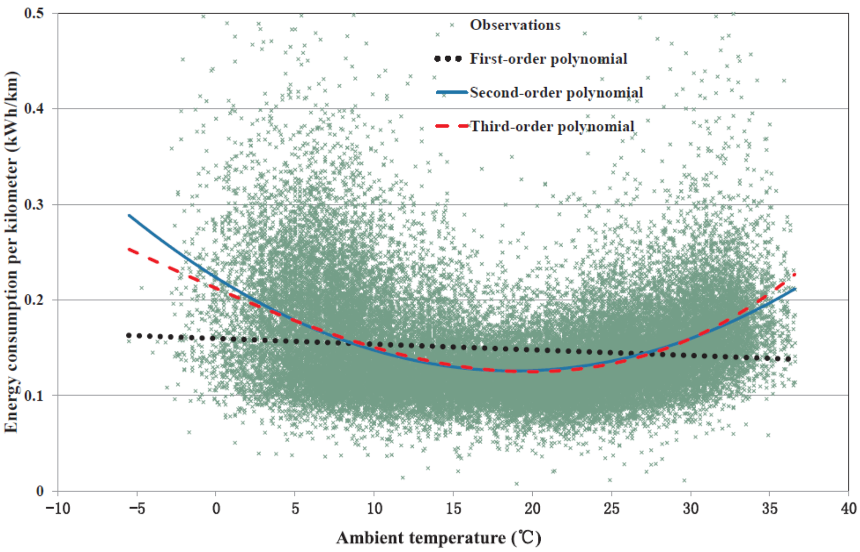

(a)

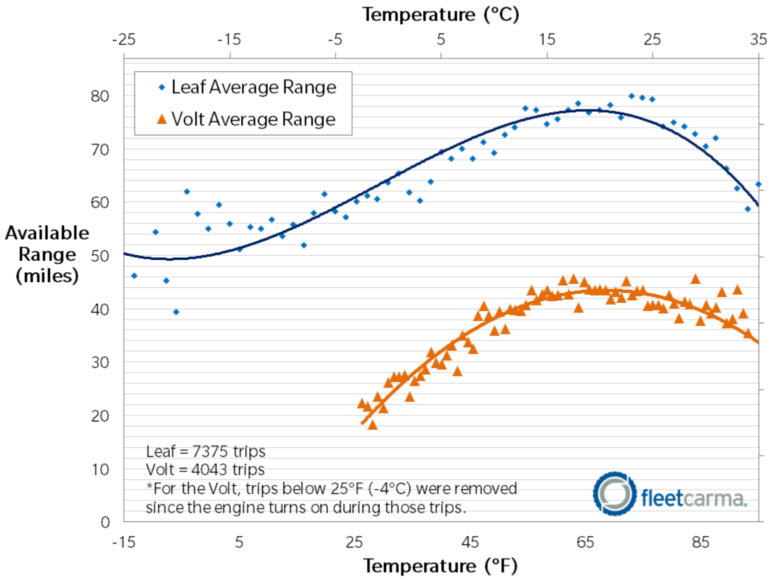

(b)

Figure 1.2 Effect of ambient temperature on (a) EV energy consumption [29] and (b) available range [30] powertrain components in EV has their own thermal requirements. The powertrain of EV mainly consists of three: motor, inverter, and battery. The power electronics and elector motor (PEEM) denotes motor and inverter and energy storage system (ESS) stands for the lithium-ion battery pack. PEEM has an upper-temperature limit of 150 °C [31, 32] and ESS has an optimal operating temperature range of around 15 - 35 °C [33]. Therefore, separate thermal management is required by delicate operation of integrated thermal management system (ITMS).

Table 1.1 Thermal requirements of each EV components

Component	Thermal requirements
Battery	15 °C – 45 °C Temperature difference within 5 °C
Electric Motor	Under 150 °C (copper coil)
Inverter	Under 150 °C (IGBT Junction)
Cabin	Around 25 °C

1.2. Literature survey

1.2.1. Adoption of heat pumps in electric vehicle

In cold climate conditions, positive temperature coefficient (PTC) heater in EVs consumes a significant amount of energy from the battery on cabin heating, because EVs lack waste heat, abundant in internal combustion engine vehicles. Therefore, the driving range of EVs critically deteriorated [21–23, 34], causing a fear called ‘range anxiety’ which is considered as an obstacle to EV market extension [20, 35]. An electric vehicle heat pump (EVHP) appears to be a solution to this problem, as it has a better coefficient of performance (COP) than PTC heater.

Kim et al. [36] presented that the combined system of heat pump and PTC heater has superior heating capacity and coefficient of performance (COP) up to 59% and 100%, respectively, compared with the conventional PTC heater based system. The benefits of adopting heat pumps in EV were also confirmed in various regional contexts by Zhang et al. [37]. Even though the performance enhancement with heat pumps varies with different cities, the heat pumps saved 41% of average energy consumption. Yu et al. [24] evaluated the energy consumption of heating ventilation and air-conditioning (HVAC) system and its impact on the range of EV. They concluded that the heat pump systems are capable of reducing power consumption of HVAC between 41% and 72% with different scenarios. Other studies also verified similar power savings effects of EVHP with different configuration and conditions [24–26, 38, 39].

However, heating performance of heat pump sharply declines under severely cold conditions [40], as presented in Figure 1.3. This phenomenon originates from the low suction density and high pressure-ratio of the heat pump system operating at low temperature. As the evaporator in the heat pump system absorbs heat from the ambient air, the evaporating temperature is lower than the ambient temperature. The low evaporating temperature accompanies low pressure and density of refrigerant, entering the compressor. The compressor displaces certain volume to the condenser so that the inlet density determines mass flow rate through the whole system. The decreased mass flow rate of total system entails decreases in the heating capacity, requiring additional use of PTC heater.

On the other hand, the pressure ratio between condensing and evaporating pressure increases due to decrease in the evaporating pressure at low ambient temperatures. The COP of EVHP sharply decreases not only with low Carnot efficiency with low heat source temperature, but also the higher power consumption of compressor. As the ideal compression process is isentropic process, the outlet temperature from the compressor increases with high pressure-ratio. The overheated refrigerant reduces the reliability of the system and degrade the lubricating oil [41].

Many studies demonstrated the performance degradation of EVHP in severely cold conditions. Qin et al. [26] experimentally showed the 33% of decrease in heating capacity when the outdoor air temperature drops from -10 °C to -20 °C. The decrease in heating capacity requires auxiliary power consumption of the PTC heater with COP of 1, resulting in inefficient HVAC system operation and increase in the net power consumption. Lee et al. [25] investigated the performance of EVHP by changing the compressor frequency with ambient temperature. Results showed the decrease in the heating COP and increase in heating capacity with the rise of ambient temperature. As the heating capacity critically affects the power consumption of HVAC system than COP, result implies that the performance of EVHP is deteriorated at low ambient temperature. Similar results were also reported by other studies [42, 43], urging a novel methodology to enhance low temperature performance of EVHP.

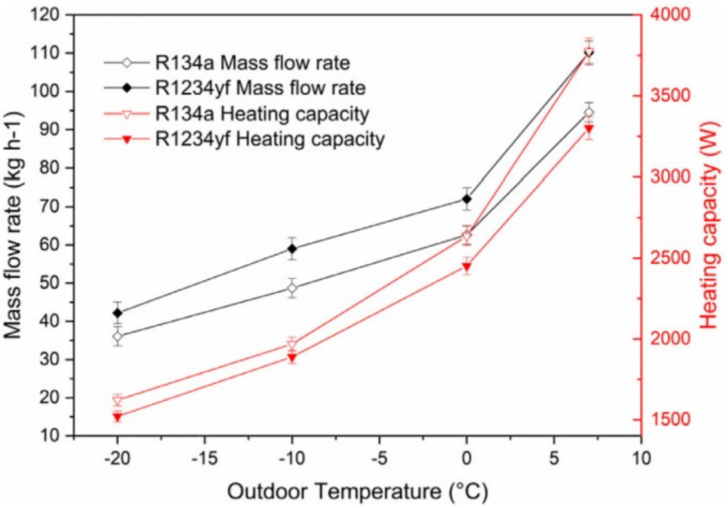

Figure 1.3 Performance of EV heat pump system at different ambient temperature [44]

1.2.2. Recent technologies to improve heating performance of EVHP

Several researches on EVHP at low ambient temperature focused that problems in cold climate fundamentally originate from the increased heating demand of cabin, most of which are occupied by ventilation load. Nielsen et al. [34] experimentally verified that the ventilation load accounts for approximately 50% of heating load in Volvo S60 in cold condition. Hirai et al. [45] also presented ventilation heat loss and heat radiation from the body contribute more than 80% of the total heating load . Zhang et al. [46] developed a model predicting EV climate control load and concluded that ventilation load occupies more than 70% of overall heating load in cold climate condition. According to the literature above, reducing ventilation load seems a reasonable approach to the climate load problem. Ventilation load, conditioning outdoor air to a desirable state to maintain thermal comfort, could be dramatically decreased in recirculation (RC) mode. Rugh et al. [47] numerically compared outdoor air (ODA) mode with recirculation mode, in which 72.1% heating load is saved. Zhang et al. analyzed the climate control load of air conditioning (AC) system, concluding that recirculation mode can save up to 48% of AC energy compared with outside air mode [46]. From a thermodynamic point of view, it is necessary to operate the heat pump in RC mode. However, recirculation mode requires an additional dehumidification process where human-emitting moisture, which causes fogging that interferes with clear vision of the driver and perturbs safe driving condition, should be removed [48]. The dehumidification includes subsequent cooling and heating process through the indoor evaporator and indoor condenser or PTC heater [45]. This process entails an inevitable inefficiency, which occurs during the subsequent dehumidification and reheating process.

On the other hand, other studies have focused on the performance enhancement of the heat pump system itself. Among various solutions, vapor injection (VI) technique and waste heat recovery (WHR) from PEEM had presented notable results. Qin et al. [49] investigated heating performance enhancement of VI cycle up to 31% compared to conventional heat pump system at -20 °C outdoor temperature condition. Kwon et al. [50] analyzed the heating capacity improvement of a VI heat pump system from the thermodynamic and geometric aspects of scroll compressor. However, an additional internal heat exchanger or flash tank is required to utilize VI technique. A heat pump system with WHR is suggested by Ahn et al. [51], estimating performance enhancement of dual-source heat pump with ambient temperature from -10°C to 7°C and maximum waste heat amount of 2.5 kW. Results showed an increase in heating capacity and COP by 9.3% and 31.5% respectively. Tian et al. [52] thermodynamically evaluated electric vehicle thermal management system with WHR in energy, exergy and thermo-economy, presenting operation cost of €249.44 and payback period of 6.77 years could be saved.

Considering the absence of an abundant waste heat from the case of internal combustion engine, EV requires delicate utilization of waste heat from electric devices. Many researchers suggested novel TMS structures [39, 48, 53, 54], integrating thermal management system (TMS) with heat pump system. Leighton et al. [23] suggested combined fluid loop system, using secondary fluid system to modularize the heat pump and strengthen the thermal connectivity. Other studies [55–58] were conducted on the effect of waste heat recovery on the heat pump system, but the waste heat was recovered at only two temperature levels: condensing temperature and evaporating temperature. The difference between the two temperature levels widens in cold condition so that the waste heat recovery at either high [59] or low temperature [51, 52, 60] became less efficient. Lee at al. [61] subdivided the temperature into three levels with vapor injection technique and experimentally demonstrated that the heating capacity increases up to 72% when the waste heat is recovered at the intermediate temperature level.

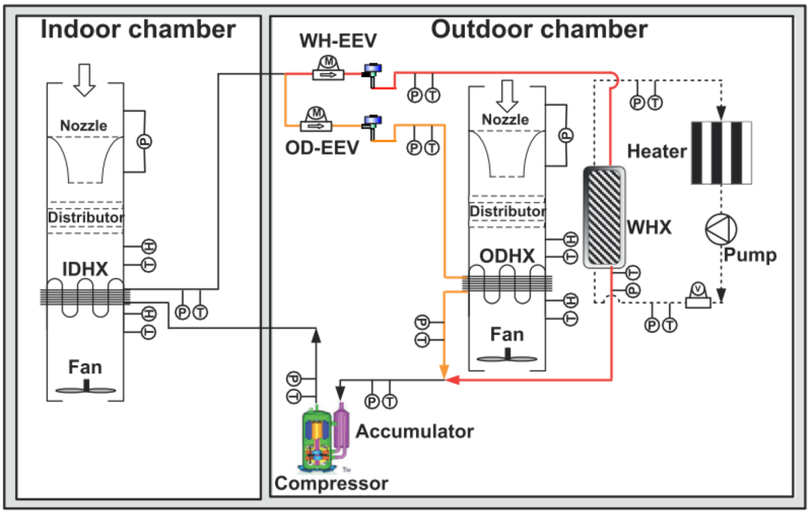

(a)

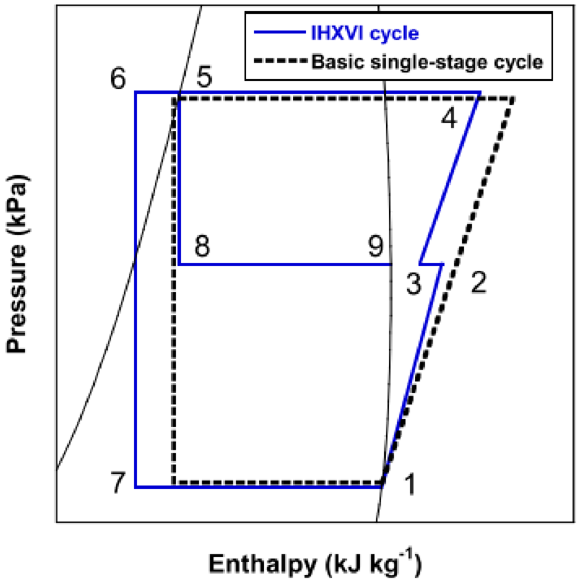

(b)

Figure 1.4 Technologies to augment the heating capacity: (a) waste heat recovery [51] and (b) vapor injection technique [62]

1.2.3. Integrated thermal management system (ITMS)

As mentioned above, EV requires a sophisticated ITMS to satisfy sensitive thermal requirements of many thermal objects. EV components, including energy storage system (ESS), power electronics and electric motor (PEEM), and cabin, have their thermal requirements. Whereas PEEM has an upper-temperature limit of 150 °C [31, 32], the lithium-ion battery has an optimal operating temperature range of around 15 - 35 °C [33].

The optimal temperature range is determined by two conflicting effects of temperature on the battery. At high temperatures, a battery encounters a decrease in life cycle and self-discharge, causing a thermal failure [63, 64]. On the other hand, the power and capacity of the battery fade at low temperatures due to the low ionic conductivity of the electrolyte and large charge transfer resistance [65–68]. Therefore, many studies were conducted on novel battery thermal management systems. The air cooling method was widely investigated because of its simplicity and low cost [69]. Pesaran et al. [70] compared air cooling design with parallel and series structures, and Sabbah et al [71]. presented the limitation of air cooling at high ambient temperatures. Many EVs adopted liquid-based cooling methods to manage the thermal state of ESS [72, 73]. However, conventional liquid-based BTMS did not heat the battery under cold-start conditions as a significant amount of energy is required to raise the temperature of the ESS. Instead, conventional BTMS used the self-heating of the battery, depending on the reversible heat generation from electrochemical reaction and Joule heating with internal resistance [59]. Few studies focused on the preheating method [38, 74, 75] including internal heating with alternating or pulse current, and external heating with air, liquid, or heat pipe.

On the other hand, as the powertrain of EV has entirely different thermal characteristics [31, 76, 77], a conventional internal combustion engine TMS with a radiator cannot simply replace the electric vehicle thermal management system (EVTMS). The powertrain of EV is composed of two major parts; PEEM and ESS, and appropriate thermal management on each electric device is essential to safe and energy-efficient driving [78, 79].

Many researches have been conducted on the effective TMS design. Park et al. [53] presented three vehicle cooling system architectures with different cooling tower design concepts. For battery electric vehicle, Leighton et al. [23] suggested a combined fluid loop system, which integrates vehicle TMS and heat pump system into a single coolant-based loop, showing driving range increase by 9% in experimental condition. Hamut et al. [80] optimized hybrid vehicle TMS using a multi-objective evolutionary algorithm. Heat pump systems are also broadly investigated to improve performance in a severe condition. Tian et al. [52] studied the performance of waste heat recovery EVTMS in thermodynamic and thermo-economic perspective.

The aforementioned researches were fundamentally based on EVTMS, utilizing waste heat from the electric devices (PEEM and ESS) to enhance driving range in winter. However, those systems require an auxiliary coolant-to-refrigerant heat recovery device, which inefficiently conveys waste heat from electric devices through the thermal resistance of the heat exchanger and working fluid. Recent studies on PEEM [48, 81–83] target higher energy density and integrity, which would cause thermal failure with the conventional coolant-based cooling method in summer. As a solution to these problems, the floating loop concept, directly utilizing liquid refrigerant in the condenser to cool down PEEM, was devised [84–86]. The high heat transfer coefficient of evaporative cooling and thermal uniformity of refrigerant were verified with previous researches [87–89].

1.3. Objectives and scopes

For the wider spread of EV, it is necessary to alleviate the range reduction at low temperatures, caused by excessive power consumption of HVAC system and poor electrochemistry of lithium-ion battery. The objective of this study lies at the establishment of MLTMS, which delicately integrates the PEEM and ESS with EVHP. The MLTMS achieves the range extension by two methods: efficient utilization of the waste heat from PEEM by subdividing the heat recovery temperature into multiple levels, and sophisticated thermal management of ESS considering the electrochemical characteristics of the lithium-ion battery. The outline of this study is as follows.

In Chapter 2, I analyzed the effect of temperature levels, recovering waste heat, on the EVHP system. The temperature levels were divided into three: condensing (high), evaporating (low), and intermediate. The waste heat recovery at intermediate temperature level was achieved by the vapor injection technique, which injects the refrigerants into the compressor chamber during compression process. Experimental studies were conducted to analyze the performances of EVHP, including heating capacity, COP, and the thermal state of the electric devices generating heat. Similarly, the heat recovery at high temperature were examined with numerical analysis. The system utilized a floating loop concept, which uses a liquid refrigerant at the outlet of condenser to absorb heat from PEEM. This concept enables a compact and efficient heat recovery with the high heat transfer coefficient of two-phase refrigerant. This chapter targets to demonstrate the effect and significance of the temperature level at which the waste heat is recovered.

In Chapter 3, I established an ITMS model including transient heat pump model and electric device models. As the EV operates from the cold-start conditions, the performance should be evaluated considering the dynamic behavior of EVHP and electric devices. A transient heat pump system model was established and validated with the experimental results. The heat pump model was integrated with the PEEM model and ESS model. PEEM model and ESS model included the heat generations of each component and the heat transfers between the components. Bench test results validated the accuracy of the models. Based on the ITMS model, the performance of multi-level waste heat recovery strategy (MWHRS) was evaluated. This chapter aims to clarify the necessity of utilizing different temperature levels in MLTMS depending on the operating conditions.

In Chapter 4, I investigated the effect of port geometries on the performance of MWHR. As the MWHR depends on the vapor injection technique, port hole geometries affect the performance of MWHR. The pressure of refrigerant recovering the waste heat is affected by the timing when injection port starts to open. As the pressure designates the saturation temperature of refrigerant, injection hole directly determines the intermediate temperature level of heat recovery. The trade-offs on the MWHR lies between the heating capacity enhancement through elevated temperature level and heat required to raise the temperature of the waste heat source. Therefore, the aforementioned ITMS model should evaluate the performance of MWHR with different port sizes and locations. I expect to derive the optimal port geometry minimizing the net power consumptions of MLTMS.

In Chapter 5, I suggested an active battery thermal management strategy. As the electrochemistry of a lithium-ion battery is critically affected by the operating temperature, proper battery thermal management is necessary. However, a heating of battery requires additional energy from ESS, where the trade-off between battery heating and performance enhancement with heating should be weighed. A battery thermal model based on the low-temperature performance experiment examined the battery performance, and the ITMS model was integrated with the battery thermal model to evaluate the whole power consumption with the systematic perspective. Furthermore, the preheating strategy to heat up the battery in advance of driving was proposed as a power saving strategy. The objective of this chapter is to demonstrate the necessity of an active battery thermal management based on the deriving condition.

In Chapter 6 , the overall results of this study are summarized.

Chapter 2. Effect of temperature level on the waste heat recovery performance[1,2]

2.1. Introduction

Previous studies on WHR systems have concentrated on the amount of waste heat without considering the temperature range. However, electric devices have specific thermal requirements. In particular, energy storage system (ESS) in EV, including lithium-ion battery, has the optimal operating temperature range of 15-35°C [33, 90–92]. Battery rapidly degrades when operating at high temperatures and power decreases at low temperatures [93, 94]. Recovering heat at the evaporating pressure accompanies the low performance of the ESS; and at condensing pressure, the temperature of the ESS exceeds its upper temperature limit. Therefore, the heat pump system in an EV requires the intermediate temperature level, which can be achieved using vapor injection technique. None of the WHR studies have utilized VI as a multi-level heat recovery device to the best of our knowledge, not as a simple integration [55].

[1,2] The contents of chapter 2 were published in *Energy Conversion and Management* on 2022. [59, 99]

This study proposes a heat pump system that absorbs waste heat from an ESS using the VI technique, which recovers heat from the ESS at an intermediate temperature and pressure. This multi-level waste heat recovery (MWHR) system can enhance the heating capacity by elevating the temperature level of the WHR while operating the ESS within an appropriate temperature range. In addition, the proposed system overcomes the difficulties in controlling a conventional EV VI heat pump system with a flash tank [95, 96] by adopting the superheat control method suggested by Wang et al. [97]. The battery thermal model from Chung et al. [98] was utilized to estimate the temperature level of the ESS with an equal volume flow rate and coolant temperature under the experimental conditions. The experimental setup for the MWHR heat pump system was built into a calorimeter to verify the heating performance and COP at various ambient temperatures, compressor speeds, and waste heat amounts.

On the other hand, researches on EVTMS utilized waste heat from the electric devices (PEEM and ESS) to enhance driving range in winter. However, those systems require an auxiliary coolant-to-refrigerant heat recovery device, which inefficiently conveys waste heat from electric devices through the thermal resistance of the heat exchanger and working fluid. Recent studies on PEEM [48, 81–83] target higher energy density and integrity, which would cause thermal failure with the conventional coolant-based cooling method in summer. As a solution to these problems, the floating loop concept, directly utilizing liquid refrigerant in the condenser to cool down PEEM, was devised [84–86]. The high heat transfer coefficient of evaporative cooling and thermal uniformity of refrigerant were verified with previous researches [87–89]. However, these studies were mainly focused on the performance of each concept. Waste heat recovery through TMS and heat pump simply assumed a certain amount of heat through auxiliary recovery device and researches on the floating loop only showed the heat transfer characteristics, rather than systematically integrating those advantages through thermal integration.

In this research, the performance enhancement of EVTMS and heat pump system with the floating loop is suggested and analyzed in systematic perspective: utilizing floating loop as an advanced PEEM cooling loop in summer and effective waste heat recovery system in winter. The heat pump and TMS model was established based on the experimentally validated component models to estimate the power consumption and heating or cooling performance of the floating loop TMS. Performance of the suggested system is presented with different ratios of the outdoor heat exchanger (ODHX) and the low-temperature radiator (LTR) within the finite total heat exchange volume to investigate the effect of heat exchange allocation when the thermal load from PEEM is shifted from LTR to ODHX. This study aims to enhance thermal connection between TMS and heat pump system through the floating loop. This thermal integration is beneficial in terms of effective waste heat recovery without auxiliary device in winter and enhanced thermal management of PEEM in summer through superior performance of evaporative heat transfer.

The contents of this chapter are published in the Energy Conversion and Management [59, 99].

2.2. Waste heat recovery at intermediate temperature level

2.2.1. Experimental setup

The heat pump systems operated in 3 modes; MWHR, CWHR and non-WHR. In MHWR mode, refrigerant discharged from the electric compressor entered the condenser, and dissipated heat to the secondary fluid passing through the plate heat exchanger (PHX), conveying heat to the indoor heat exchanger (IDHX). Refrigerant from condenser split into WHR loop and evaporator, both of which absorbed the heat obtained in the outdoor heat exchanger (ODHX) and WHR loops. The ODHX took heat from the ambient air with a secondary fluid, which heated up the low-pressure refrigerant in the evaporator. In the WHR loop, the heat absorption process occurred equally except that the refrigerant in the waste heat exchanger (WHX) directly absorbed heat from the coolant, which conveys the heat generated from electric heater. The WHR process occurred under the intermediate pressure condition and the refrigerant was injected into the VI compressor. The low-pressure refrigerant in evaporator flows to the compressor after passing through the accumulator and intermediate temperature refrigerant in the WHX was injected into the compression chamber of scroll compressor. The MWHR system fundamentally works similarly with the two-stage compression [100]. The two-stage compression system can efficiently recover the heat from the heat sources having different temperature level. However, the MWHR system requires only one compressor and scroll head with injection port, whereas the two-stage compression system consists of two compressors. Considering that the compressor is the most expensive device in the EV heat pump system, the MWHR can achieve an equivalent performance as the two-stage compression system with much less cost and system complexity.

CWHR mode follows equal process with MWHR mode except that WHR occurs at low temperature and outlet refrigerant from WHR loop and evaporator merged before entering accumulator. Non-WHR mode operated only with ambient air heat source. Figure 2.1 illustrates the simplified configuration of each waste heat recovery system, where the refrigerant passing through the waste heat recovery device is incorporated into suction pipe in the CWHR system and injected into the VI compressor in the MWHR system.

Figure 2.2 presents pressure-enthalpy diagram of heat pump systems in CWHR and MWHR mode. As shown in the figure, the MWHR system recovers waste heat at the intermediate temperature level, which is higher than the evaporating temperature. Therefore, the injected refrigerant with higher enthalpy augments additional amount of heating capacity on the MWHR system, compared with the CWHR system.

Figure 2.3 shows a schematic diagram of the MWHR heat pump experimental setup. The test bench resides in a calorimeter with a capacity of 10 RT (38.6 kW), which has two chambers: outdoor chamber is designed to maintain the air temperature from -30 °C to 60 °C and relative humidity from 10% to 90%, and indoor chamber maintains air temperature and relative humidity ranging from 0 °C to 30 °C and 10% to 90%, respectively.

The heat pump system included a primary refrigerant loop and a secondary coolant loop. The primary loop consisted of a VI compressor, three PHXs, two electronic expansion valves (EEVs), and a WHR system. VI compressor is a scroll compressor with a vapor injection port, and the pressure difference between injection port and compression chamber derives mass flow of the injected refrigerant. The three PHXs function as a condenser, evaporator WHX. The brazing-type PHXs have plate dimensions of 285 mm in length, 105 mm in width and 0.026 m^2 of heat transfer area per each plate, and the condenser, evaporator and WHX have 33, 27, and 19 plates, respectively. EEVs control the opening area in 2,000 steps with unipolar step motor and are designed to be installed in the heat pump system having a capacity of 1.5 RT (5.8 kW). WHR system includes electric Joule heater that provides heat of up to 2 kW and a coolant reservoir. The secondary loop delivers heat obtained from the primary refrigerant loop to the air with a secondary working fluid, a mixture of water and ethylene glycol with equal volume. Three centrifugal pumps, whose frequencies can be controlled by an external voltage signal, drive the secondary working fluid. The IDHX and ODHX are coolant to air heat exchangers with fan and frontal vane regulating exhaust velocity. IDHX is a louvered-fin tube heat exchanger of 215 mm in height, 87 mm in width, and 44 mm in depth. ODHX is a fin-tube heat exchanger with 410 mm in height, 430 mm in width, and 250 mm in depth and the attached fan has a volumetric flow rate of 1,060 m^3/h. An exhaust fan, having a maximum capacity of 90 m^3/min, compensated the differential pressure developed through the duct based on the pressure difference between the chamber and exhaust air from the nozzle.

Figure 2.4 shows the heat pump system in the outdoor chamber. The temperature and humidity of the air in the chamber were measured using an air-sampling unit, and the thermodynamic states of the refrigerant and coolant were measured using pressure, temperature and mass flow rate sensors.

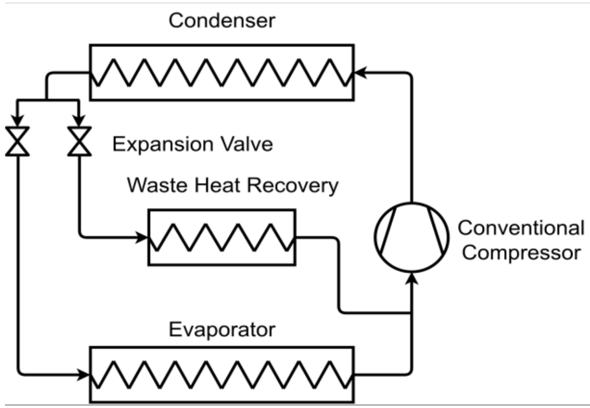

(a) CWHR

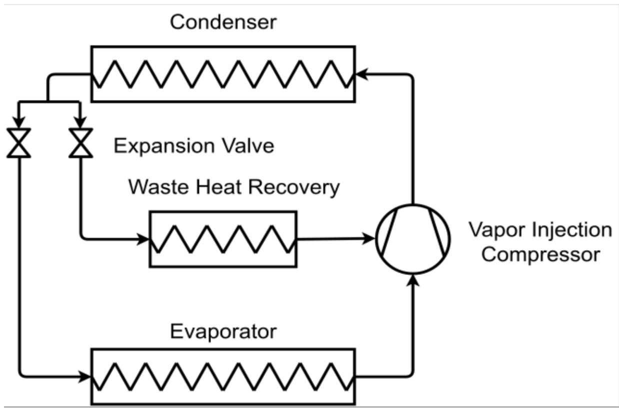

(b) MWHR

Figure 2.1 Simplified system configuration: (a) conventional waste heat recovery system (CWHR) and (b) multi-level waste heat recovery (MWHR) system with vapor injection compressor.

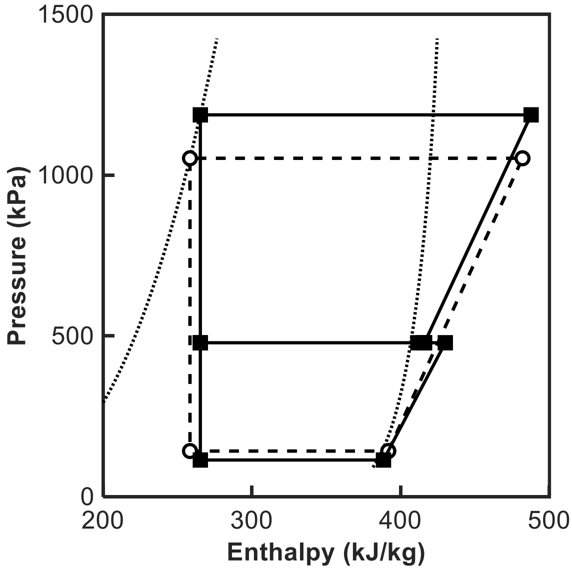

Figure 2.2 Pressure-enthalpy diagram of heat pump system with CWHR and MWHR modes.

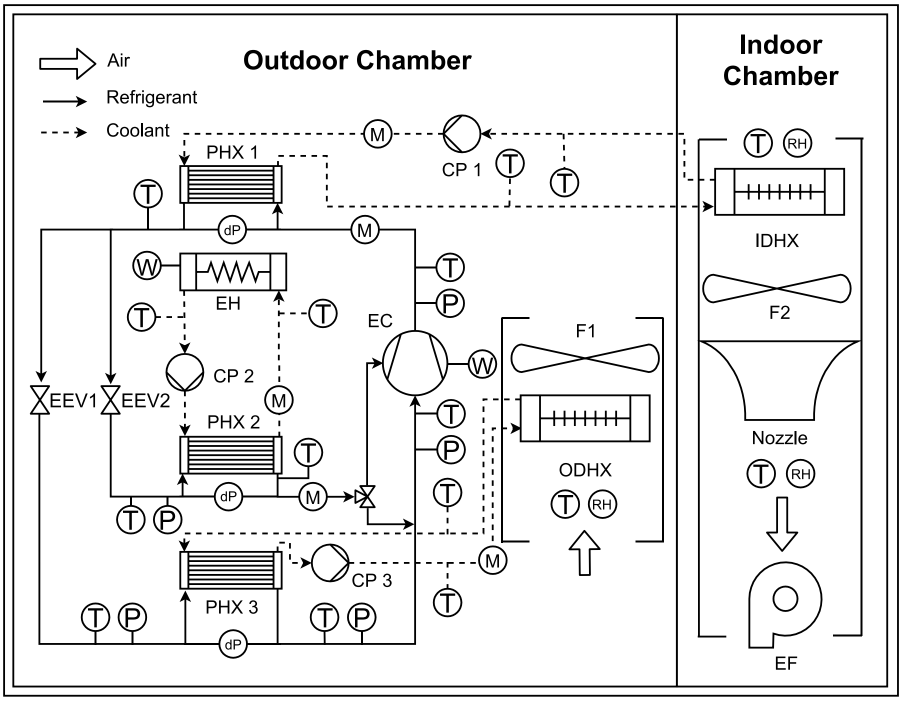

ODHX	Outdoor heat exchanger	**F**	Fan	**CP**	Coolant pump
IDHX	Indoor heat exchanger	**EEV**	Electronic expansion valve	**EC**	Electric compressor
PHX	Plate heat exchanger	**EH**	Electric heater	**EF**	Exhaust fan

Figure 2.3 Schematic diagram of experimental apparatus

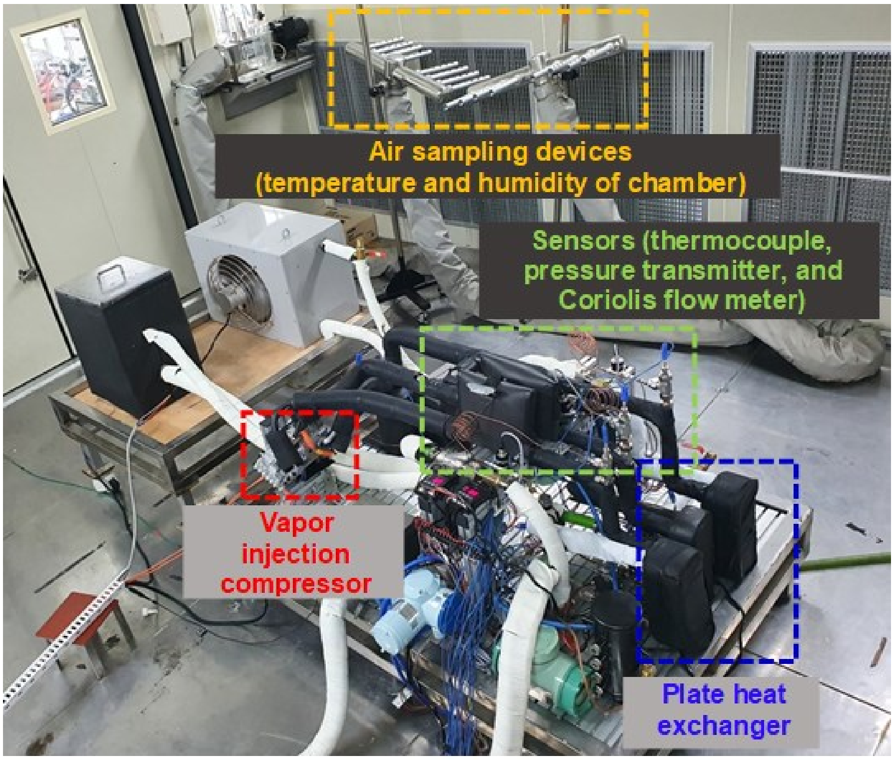

Figure 2.4 Experimental apparatus in psychrometric calorimeter.

2.2.2. Accuracy of measuring devices and uncertainty analysis

The enthalpy difference between the incoming and outgoing air was calculated from the temperature and relative humidity. Dry-bulb and wet-bulb temperatures of the indoor chamber were measured using platinum resistance thermometers (PRTs) having an accuracy of 0.2%. The air volume flow rate was calculated according to ANSI/AMCA 210 [101] and linearly correlated with the energy balance equation in various operating ranges that the standard does not cover. Differential pressure transducer used to measure pressure difference through nozzle had an accuracy of 0.2%. The main parameters used in the coolant-refrigerant system analysis were the temperature, pressure and flow rate. Temperature and pressure are measured at each inlet and outlet of the three PHXs. T-type thermocouple with grounded junction probe was used as the temperature measuring device with an accuracy of 0.4%. Pressure was measured with pressure transmitter with the accuracy of 0.5%. Two mass flow rates of refrigerant were measured with a Coriolis flowmeter and three volumetric flow rates of coolant are measured with turbine-type flowmeter; the accuracies of each flowmeter are 0.5% and 1.0%, respectively. Two digital power meters measured the net power consumed by the electric compressor and electric heater with the accuracy of 0.6%. Table 2.1 summarizes the accuracy of each sensor. The key indicators of the system performance, heating capacity, and COP, are analyzed using Eq. (2.4) and Eq. (2.5) below.

$$Q_{air} = \rho \dot{V} \Delta h \qquad \text{Eq. (2.4)}$$

$$COP = \frac{Q_{air}}{W_{comp}} \qquad \text{Eq. (2.5)}$$

ASHRAE handbook [102] provided correlations to calculate the enthalpy of air with dry bulb temperature and wet bulb temperature. We calculated the enthalpy difference between inlet and outlet air through IDHX with the

$$\frac{\delta R}{R} = \left[\sum_{1}^{N} \left(\frac{x_i}{R}\right)\left(\frac{\partial R}{\partial x_i}\right)\left(\frac{\delta x_i}{x_i}\right)^2\right]^{\frac{1}{2}} \qquad \text{Eq. (2.1)}$$

$$\frac{\delta Q_{air}}{Q_{air}} = \left[\left(\frac{\delta \dot{V}}{\dot{V}}\right)^2 + \left(\frac{\delta \rho \Delta h}{\rho \Delta h}\right)^2\right]^{\frac{1}{2}} \qquad \text{Eq. (2.2)}$$

$$\frac{\delta COP}{COP} = \left[\left(\frac{\delta Q_{air}}{Q_{air}}\right)^2 + \left(\frac{\delta W}{W}\right)^2\right]^{\frac{1}{2}} \qquad \text{Eq. (2.3)}$$

correlations. The uncertainty of these performances was calculated based on the Moffat theory [103] and the derived Eq. (2.1) to Eq. (2.3) are shown below.

Heating capacity and COP have uncertainties of 5.8% and 5.9%, respectively.

Table 2.1 Accuracies of measuring devices

Sensors	Range	Unit	Accuracy
Platinum resistance thermometers	-200 ~ 250	°C	0.3 °C
T-type thermocouple	-270 ~ 400	°C	1.0 °C
Pressure transmitter	0 ~ 100	bar	0.5%
Coriolis flowmeter	0 ~ 360	kg/h	0.5%
Turbine flowmeter	7.6 ~ 56.8	L/min	1.0%
Differential pressure transmitter	0 ~ 100	mmAq	0.2%
Digital power meter	0 ~ 600	V	0.4%
	0 ~ 20	A	0.4%

2.2.3. Test procedure

The test parameters are presented in Table 2.2. We selected R134a as a refrigerant, which is most commonly used. The outdoor temperature varied from 0 °C to -20 °C and indoor temperature was set a dry bulb temperature of 20°C and wet bulb temperature of 15 °C, which is a standard heating test condition presented by ASHRAE [104]. The amount of waste heat reaches 2.0 kW at maximum as in other studies [51, 105]. The compressor speed was varied from 2,000 rpm to 5,000 rpm, where the heat pump system operated properly without overheating or instability of the degree of superheat (DSH) control. Air flow rate and velocity of IDHX and ODHX are set as 9.0 kg/min and 2.0 m/s based on the SAE J2765 [106] test condition. A constant DSH was maintained in each experiment at 5 K and the DSH of the injected refrigerant was set to 5 K to prevent liquid refrigerant inflow. The opening area of the intermediate EEV controls the mass flow rate of the injected refrigerant to maintain a certain amount of DSH, whereas the primary EEV controls DSH of the refrigerant flowing through the compressor suction port. After two chambers were stabilized to a steady-state, overall heat pump system was initiated and stabilized.

.

Table 2.2 Experimental conditions

Parameter	Values
Outdoor air temperature (°C)	-20/-15/-10/-5/0
Indoor air temperature (°C)	20 (DB)/15 (WB)
Compressor speed (rpm)	2,000/3,000/4,000/5,000
Mass flow rate of indoor air (kg/min)	9.0
Air velocity of outdoor (m/s)	2.0
Volumetric flow rate of coolant (L/min)	10
The amount of waste heat (kW)	0.0/0.5/1.0/1.5/2.0
DSH (°C)	5
Refrigerant charge (g)	2,000

2.2.4. Results and discussion

The results were thoroughly investigated by varying the following key parameters in the heat pump system: outdoor air temperature, the amount of waste heat, compressor speed, and recirculation ratio. The heating performance is presented in terms of heating capacity, power consumption of compressor, supply air temperature, and coefficient of performance (COP). Thermodynamic parameters indicating cycle performance are condensing, evaporating, and intermediate (injected) pressures; total and injected mass flow rate; and coolant temperature, which transfers waste heat to the refrigerant.

Figure 2.5 and Figure 2.6 shows the heating performance of the non-WHR, CWHR, and MWHR system under different outdoor air temperature conditions.

Heating capacities at various outdoor air temperatures are presented in Figure 2.5 (a), which indicates that the heating capacity of the MWHR system is increased up to 33.1% and 72.5%, compared with CWHR and non-WHR systems at the coldest condition. This capacity enhancement originates from the existence of waste heat, which is shown in both the CWHR and MWHR systems, and the elevated temperature level of the injected refrigerant, which contributes to the increased capacity of the MWHR system. Considering that the COP of the PTC heater is 1 at the maximum, less power of the ESS is consumed in MWHR system even with the increased power consumption of the compressor in Figure 2.5 (a), which obtains the heating capacity with a COP greater than 1. Both the MWHR and CWHR systems infuse additional refrigerants into the compressor, increasing the total power consumption of compressor, as well as the heating capacity. Therefore, the COP, which is shown in Figure 2.5 (a), is determined by the proportional change in the heating capacity and compressor work. The decreasing trend with ambient temperature is mainly affected by the Carnot efficiency of the heat pump cycle, which is represented as the ratio of the condensing temperature to the temperature difference between condensing and evaporating temperatures. Notably, a cross point of the COP exists in the MWHR and CWHR systems. This occurs because of the relative insensitivity of the injected mass flow rate in the MWHR system compared with the CWHR system, as shown in Figure 2.5 (b). The injected mass flow rate of the MWHR remained relatively constant, whereas the mass flow rate decreased with decreasing temperature in the CWHR system. As the scroll compressor sweeps a constant volume of refrigerant, the pressure decrease directly affects the mass flow rate of the compressor by decreasing the suction density in the CWHR system. However, the injected mass flow rate in the MWHR system is motivated by the pressure difference between the WHR and compression chamber, such that the pressure decrease in the WHX is compensated by the simultaneous pressure drop in the compression chamber.

Therefore, the COP decreases less rapidly in the MWHR system than in the CWHR and non-WHR systems, which is one of the advantages of MWHR considering the severe range reduction under harsh conditions. As the outdoor air temperature decreased, the heating capacity decreased owing to reduced mass flow rate of the refrigerant in condenser as shown in Figure 2.6 (a). This phenomenon is one of the most critical factors that affects performance deterioration of heat pump system in a severely cold condition. This mass flow rate shortage was supplemented by the injected mass flow rate in both the CWHR and MWHR systems. In quantitative perspective, a greater amount of refrigerant was injected in the CWHR than in the MWHR system. However, the quality of the injected refrigerant was superior in the MWHR system to that in the CWHR system. The pressure and temperature of the injected refrigerant in the MWHR system are higher than those in the CWHR system, resulting in a higher energy level, indicating qualitative the waste heat utilization. The performance enhancement of the CWHR system originates from the existence of dual-source [51], where the ODHX and WHX are equivalent to a heat recovery device at ambient temperature. Therefore, an additional heat transfer area was obtained through the WHX, resulting in lower temperature difference between the heat source temperatures.

In Figure 2.6 (a), the difference between evaporating pressure and injected pressure existed because of the Coriolis type mass flowmeter. Conventionally, the flowmeter is installed at the outlet of compressor, which has high pressure. However, as we already installed a flowmeter at the compressor outlet to measure the total mass flow rate, it was inevitable to place the flowmeter at the injection line to measure the flow rate of injected refrigerant. Especially in CWHR mode, the pressure loss was larger with low operating pressure. The low-pressure trend in Figure 2.6 (a), indirectly increases the mass flow rate through the higher density of the suction refrigerant. However, the mass flow rate of the compressor is separated into ODHX and WHX in the CWHR system so that an imbalance in the mass flow rate may occur, which will be presented in the following section. The temperature level of waste heat is presented in Figure 2.7 (a), ranging from 15 °C to 25 °C in MWHR and -13 °C to -3 °C in CWHR.

The temperature of the ESS was estimated with battery thermal model in a previous study [107], finding the thermal state of the battery, where the heat generated in the battery, corresponding to the amount of waste heat imposed, was rejected to the coolant with equal inlet and outlet temperatures and mass flow rates in the experiments. The result shows that the temperature of ESS resides within an appropriate temperature range of 15 °C to 35 °C [23] in

MWHR. In contrast, the temperature of ESS is lower than 5 °C in CWHR, which accompanies power and capacity fade [63].

The air temperature passing through the IDHX presents similar trend in Figure 2.7 (b) showing higher temperature range in the MWHR system than in the CWHR and non-WHR systems. Therefore, MWHR reduces the power consumption of PTC heater, which provides addition heat to the air from IDHX to reach thermal comfort conditions more rapidly.

The compressor speed is the main control variable for complying with the heating demand. Figure 2.8 with various compressor speeds suggests a reference data for the control strategy depending on the circumstance of the cabin. The compressor speed mainly affects the mass flow rate is, and the compressor sweeps a finite volume at the corresponding frequency.

Figure 2.8 (a) presents the heating capacity of each system showing an increasing trend with compressor speed. This trend suggests that non-WHR cannot provide sufficient heating capacity of 2 kW even with maximum compressor speed when the ambient temperature is lower than -10 °C, requiring utilization of PTC. The CWHR cannot satisfy the heating demand of 3 kW at the maximum compressor speed. Therefore, MWHR is necessary to save the energy consumed by the PTC heater, which requires as much energy as insufficient heating capacity. The COP decreased with the compressor speed as the difference between the condensing and evaporating temperature enlarged, as shown in Figure 2.8 (b).

This originated from the lower heat exchanger efficiency due to larger mass flow rate through a heat exchanger with finite heat transfer area. However, the COP of the non-WHR decreases at compressor speeds lower than 3,000 rpm, at which the heat exchanger cannot absorb or reject a sufficient amount of heat with small mass flow rate. The effect of compressor speed on conventional and vapor injection system was thoroughly investigated by Qin et al [49]. The heating and cycle performance in the research showed similar trend with the experimental results in this study. The COPs of CWHR and MWHR systems show a similar increasing trend with decreasing compressor speed because the -10 °C condition is near the cross point shown in Figure 2.6 (b).

Figure 2.9 (b) shows the total and injected mass flow rate of the refrigerant. Total mass flow rate increased with compressor speed as explained above. However, the injected flow rate exhibits a different trend, and the injected flow rate decreases in the CWHR until an imbalance between heat absorption in WHX and evaporator occurs. When mass flow rate of evaporator cannot match a certain DSH at the evaporator outlet with the smallest opening ratio of EEV, waste-heat only mode operates, which absorbs heat only from the WHX. Therefore, the injected mass flow rate of CWHR increased with decreasing compressor speed because the mass flow rate of compressor flowed entirely through the WHX. In the waste-heat only mode, heat from the ambient air cannot be utilized. However, MWHR does not suffer from the imbalance problem of WHX and evaporator because vapor injection actively forces a refrigerant inflow with pressure difference between the compression chamber and WHX, and does not passively shares a certain portion of the flow as CWHR. The consistent utilization of ambient air is one of the advantages of the MWHR system. The pressures in Figure 2.9 (a) show a general trend, except for the intermediate pressure of the MWHR system, which decreases with increasing compressor speed. This phenomenon is closely related to the injection principle of scroll compressors. The injection hole is located at a certain position on fixed scroll. It opens, and the refrigerant is injected when the orbiting scroll passes through the injection hole. Therefore, the volume of compression chamber, where the injection was initiated, was determined by the position of injection hole. Therefore, the volumetric ratio of the swept volume to the volume of compressor chamber when injection begins is constant over the various compressor speed region. Therefore, the injected pressure follows the evaporating pressure, which decreases with increasing compressor speed because of the higher heat requirement to match the target DSH with a higher mass flow rate, rather than the condensing pressure. However, the injected pressure of the CWHR remains relatively constant with a larger heat transfer area, and the pressure of the WHX follows the evaporating pressure of the ODHX owing to parallel pipe connection. The temperature level of the waste heat and ESS in Figure 2.9 (a) indicates that the thermal requirement of battery is satisfied only in the MWHR system. As the heating capacity increases, the air temperature provided in Figure 2.9 (b) shows an increasing trend with compressor speed.

The amount of waste heat significantly affected the overall system performance. The mass flow rate imbalance problem is clearly shown in Figure 2.10 and Figure 2.11, where the solid or dashed lines for CWHR are disconnected when the heat recovery mode switches from the dual-source mode to waste heat only mode. This problem was also reported in the waste heat recovery study by Ahn et al. [51] and the waste heat from the ambient air source was not utilized when the imbalance between the two heat sources became severe. The mode switch depends mainly on the amount of waste heat. The entire flow motivated by the compressor flows through the WHX owing to the lack of sufficient mass flow rate in the evaporator to obtain the DSH. This entails the incapability of utilizing heat from ambient air source, which downturns the heating performance indicators including heating capacity and COP as presented in Figure 2.10 (a) and (b) with increasing amounts of waste heat. The total mass flow rate declines with more waste heat (1.5 kW) due to its incapability, equal to the total mass flow rate and injected mass flow rate in Figure 2.11 (a). The mass flow rate and other performance indicators increased with increasing waste heat. The problem in the CHWR system does not occur in the MWHR system as shown in Figure 2.11. The MWHR system utilizes ambient air source with any amount of waste heat, and the performance enhancement by increasing waste heat is monotonic and consistent. The maximum heating capacity and COP reach 3.9 kW and 1.98, which are 45.6% and 2.3% greater than those of the CWHR system with the maximum amount of waste heat, which demonstrates that the MWHR system recovers the waste heat more efficiently than the CWHR system. However, a problem occurs with thermal management of the ESS, shown in Figure 2.12 (a). The temperature range of the battery in MWHR exceeds its recommended temperature range from 15 °C to 35 °C, reaching up to 44 °C with the maximum amount of waste heat. In this region, CWHR is recommended to operate as an ESS thermal management mode, in which battery temperature is 19 °C. However, except for the excessive heat generation cases, the MWHR system is superior to the CWHR both in terms of performance as a heat pump as shown in Figure 2.12 (a) and thermal management system presented in Figure 2.12 (b).

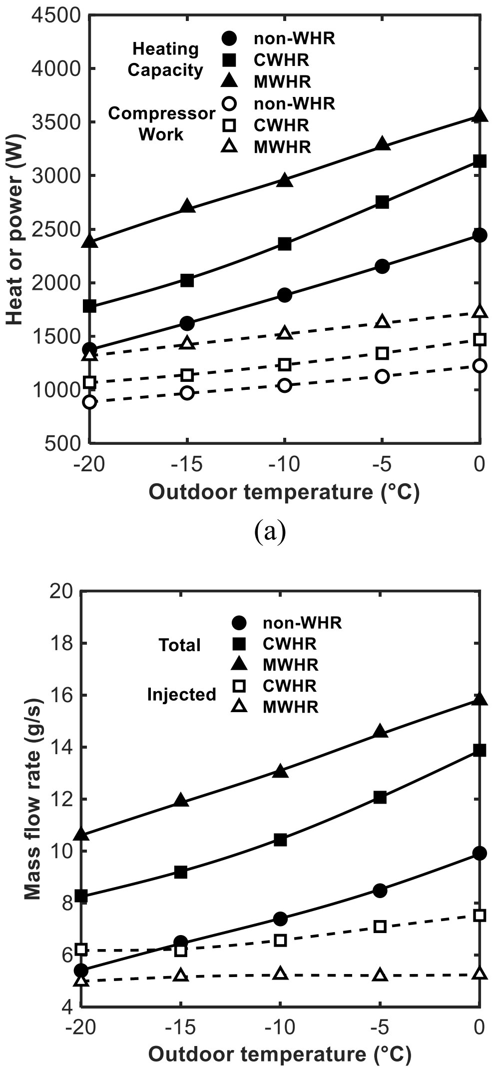

(a)

(b)

Figure 2.5 Performance of the non-WHR, CWHR, MWHR system with different outdoor air temperatures; (a) heating capacity and power consumption of compressor, (b) total and injected mass flow rate (with compressor speed of 4,000 rpm and waste heat amount of 1 kW)

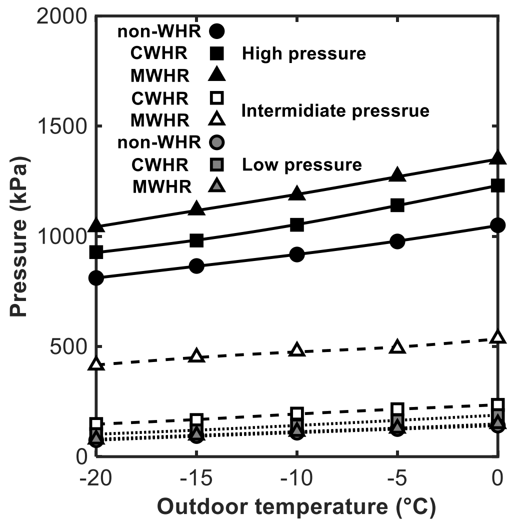

(a)

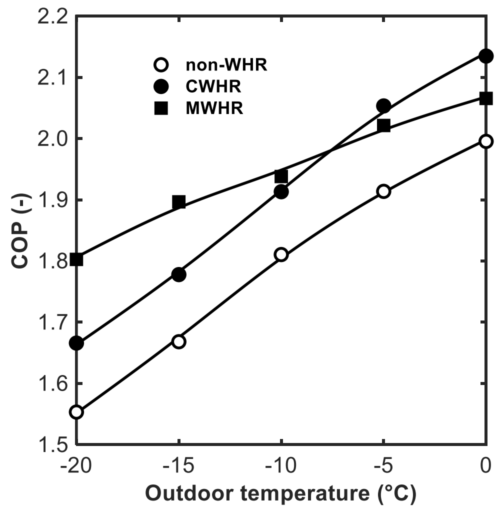

(b)

Figure 2.6 Performance of the non-WHR, CWHR, MWHR system with different outdoor air temperatures; (b) COP and (c) condensing, evaporating, and intermediate pressures (with compressor speed of 4,000 rpm and waste heat amount of 1 kW).

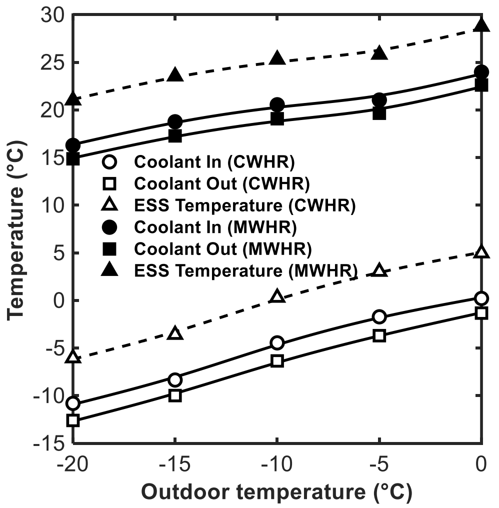

(a)

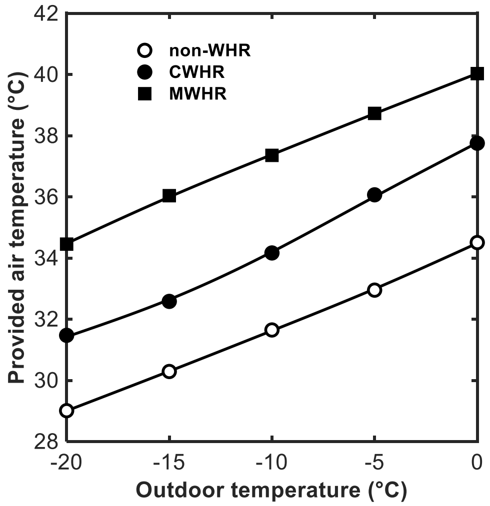

(b)

Figure 2.7 Temperature trend of (a) coolant passing through WHX and estimated ESS temperature and (b) air provided in cabin with different outdoor temperature in non-WHR, CWHR, and MWHR mode (with compressor speed of 4,000 rpm and waste heat amount of 1 kW).amount of 1 kW).

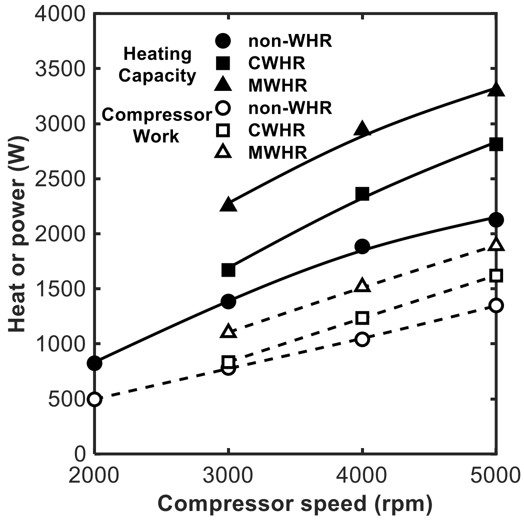

(a)

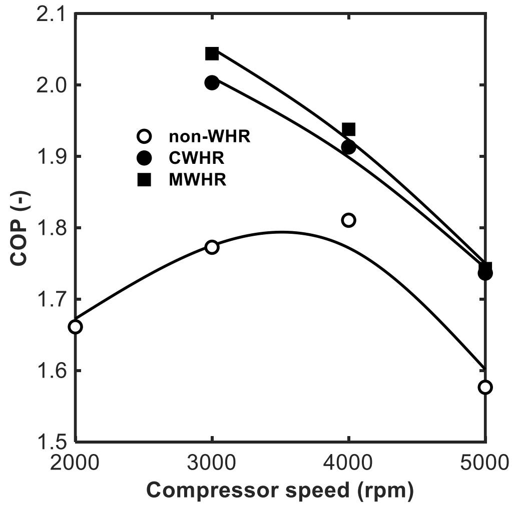

(b)

Figure 2.8 Performance of the non-WHR, CWHR, MWHR system with different compressor speed; (a) heating capacity and power consumption of compressor and (b) COP (with ambient temperature of -10°C and waste heat amount of 1 kW).

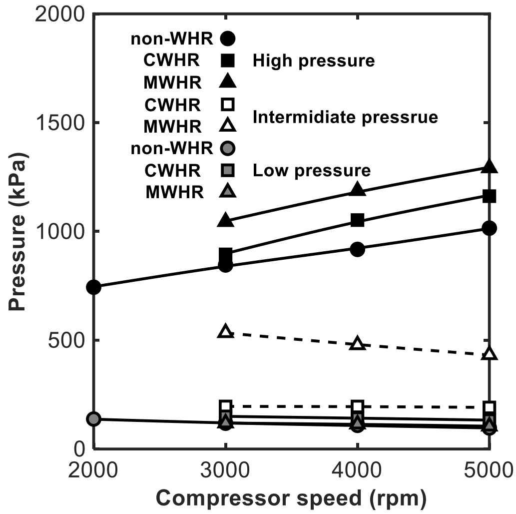

(a)

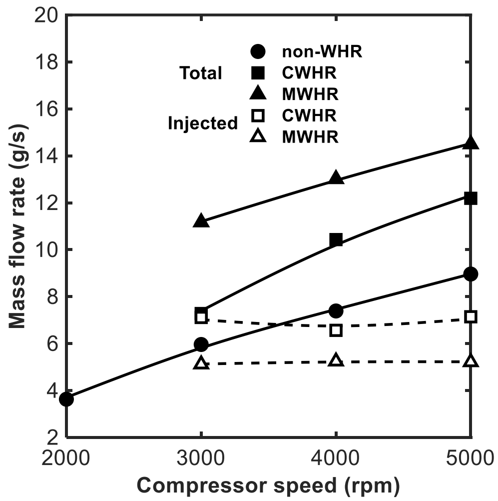

(b)

Figure 2.9 Performance of the non-WHR, CWHR, MWHR system with different compressor speed; (a) condensing, evaporating, and intermediate pressures, and (b) total and injected mass flow rate (with ambient temperature of -10°C and waste heat amount of 1 kW).

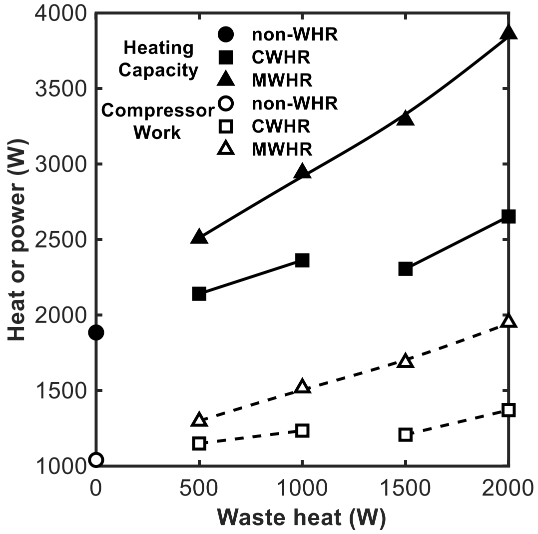

(a)

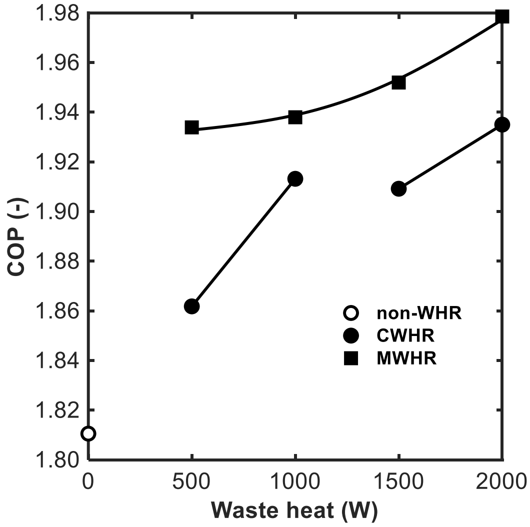

(b)

Figure 2.10 Performance of the non-WHR, CWHR, MWHR system with different amount of waste heat; (a) heating capacity and power consumption of compressor and (b) COP (with ambient temperature of -10°C and compressor speed of 4,000 rpm).

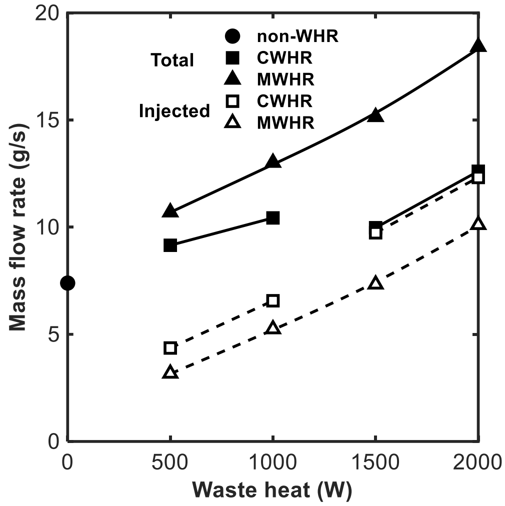

(a)

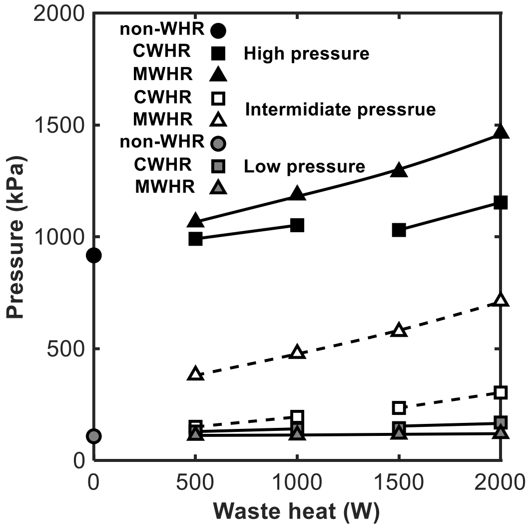

(b)

Figure 2.11 Performance of the non-WHR, CWHR, MWHR system with different amount of waste heat; (c) condensing, evaporating, and intermediate pressure, and (d) total and injected mass flow rate (with ambient temperature of -10°C and compressor speed of 4,000 rpm).

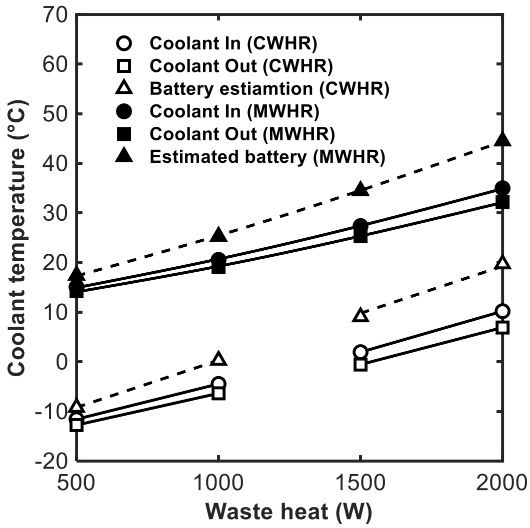

(a)

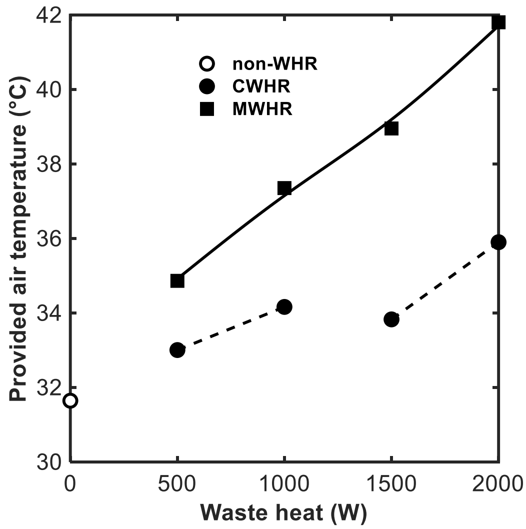

(b)

Figure 2.12 Temperature change of (a) coolant passing through WHX and estimated ESS temperature and (b) air provided in cabin with waste heat amount in non-WHR, CWHR, and MWHR modes (with ambient temperature of -10°C and compressor speed of 4,000 rpm).

2.3. Waste heat recovery at high temperature level

2.3.1. System description

Conventional heat pump and thermal management system (CHPTMS) consists of the refrigerant-based heat pump system and separate coolant-based TMS, as shown in Figure 2.13 (a). The heat pump system in CHPTMS has one electric compressor (EC) and three electric expansion valves (EEVs), which respectively control the throttling area to maintain a certain degree of superheat (DSH) of each heat exchanger. Three heat exchangers consist of two indoor heat exchangers (IDHXs) and one outdoor heat exchanger, which absorb or release heat from or to the air according to operating mode. The air-mix door f

positive temperature coefficient heater (PTCH) or not, depending on the desired thermal state of air provided in the cabin. The refrigerant flow bypasses three EEVs unless the following heat exchanger operates as an evaporator. Conventional TMS has a simple structure, radiating the heat generated from PEEM and ESS through the radiator. When the radiator alone cannot satisfy the thermal requirement of ESS, the ESS cooling loop separates with the PEEM cooling loop and the battery chiller takes the cooling demand of ESS. The floating loop heat pump system and thermal management system (FLTMS) are presented in Figure 2.13 (b). FLTMS similarly works with the CHPTMS except for the PEEM thermal management loop. A refrigerant pump (RP) draws the liquid refrigerant from the refrigerant reservoir (RSV), which utilizes an existing receiver dryer, to circulate in the floating loop. Based on the geometry and thermodynamic property of the refrigerant, the supplementary refrigerant charge on the cooling jacket is about 50 g, which can be considered as the small amount if a liquid line to the RP is short enough. The liquid refrigerant evaporates when absorbing generated heat from PEEM and is injected into the indoor condenser (IDHX 1) inlet. The operating temperature range of the floating loop and LTR loop in summer is similar because both ODHX and LTR have an equal heat sink, the ambient air, to reject heat from the working fluid. The floating loop outperforms the LTR loop in cooling performance due to the higher heat transfer coefficient of two-phase refrigerant, reducing the required mass flowrate of the working fluid and saving pump work. In addition, the floating loop benefits more in winter when the waste heat from PEEM is absorbed by the refrigerant and provides supplementary heat to the cabin through the IDHX 1. Therefore, the floating loop is advantageous in overall outdoor conditions, especially in winter with additional waste heat recovery and in parallel with summer, maintaining the electric devices within allowable temperature range with less power.

In Figure 2.14, system configuration and fluid flows of CHPTMS and FLTMS are presented in two operating modes; cooling mode and heating mode. In cooling mode configuration shown in Figure 2.14 (a), high-temperature refrigerant from compressor rejects heat through the ODHX and sub-cooled liquid refrigerant expands through two expansion valves, EEV 1 and EEV 3. The stream passes through IDHX 2 absorbing heat from ambient air and part of the stream is routed to the battery chiller, which separately operates with PEEM TMS loop when the ESS cannot maintain adequate temperature range with LTR.

Each stream merges in front of the compressor and completes the circuit. Two expansion valves control the DSH of each refrigerant from battery chiller and IDHX 2. IDHX does not convey any heat in summer when the air-mix door is closed. As shown in Figure 2.14 (b), heating mode opens the air-mix door to utilize IDHX 1 as an indoor condenser. The high-temperature refrigerant from compressor provides heat to ambient air and insufficient heating demands are fulfilled with PTCH. The sub-cooled refrigerant expanding through the EEV 2 and absorbs heat from outdoor air through ODHX, which works as an evaporator in contrast with the ODHX in summer and superheated vapor enters the compressor, completing the circuit. In winter, LTR loop is capable of dissipating the generated heat without chiller due to the high temperature difference between low ambient air and the operating temperature range of each electric device. In moderate condition, the coolant pump controls the flowrate to balance the self-heating of electric devices and heat dissipation through LTR. When the ESS temperature increases higher than the upper limit, the LTR loop separates and the battery chiller cools down the ESS, while LTR only manages the heat from PEEM.

Figure 2.14 (c) and (d) show the system configuration and fluid streams of FLTMS in summer and winter. The most distinctive characteristic of this system is the floating loop, where the refrigerant pump circulates the liquid refrigerant from condenser outlet and injects vaporized refrigerant into the condenser inlet, increasing the mass flowrate of refrigerant in condenser. As the operating mode of FLTMS changes, the heat exchanger working as a condenser relocates from IDHX 1 in winter to ODHX in summer. In both modes, refrigerant from condenser enters RSV and RP draws liquid refrigerant from RSV. Cooling mode operation in Figure 2.14 (c) requires three heat rejection processes maintaining appropriate thermal state of cabin, ESS and PEEM. Refrigerant flow from ODHX splits into 3 streams passing through each thermal management object. Temperature ranges for ESS of 15-35°C and for cabin around 25°Care lower than the temperature limit of PEEM, which is around 150°C. Therefore, the former two objects require low-temperature heat sink, the refrigerant expanded through EEV 1 and 3, whereas the latter maintains under temperature limit with relatively high-temperature heat sink, the compressed liquid refrigerant from the ODHX. Absorbed heat from the objects is dissipated through ODHX. In heating mode shown in Figure 2.14 (d), IDHX 1 provides heat absorbed from PEEM and ambient air through floating loop and ODHX and insufficient heating load is supplemented using auxiliary PTCH. Temperature of ESS is managed with self-heating effect and heat rejection through cool enough ambient air in winter.

Complete refrigerant loop heat pump and thermal management system (CRLTMS)in Figure 2.15 (a) is configured as an extended concept of FLTMS, eliminating LTR replaced with enlarged ODHX. LTR is essential to the conventional EVTMS. However, considering the function of LTR in heat-dissipating, ODHX can replace the LTR if the thermal load on LTR is affordable to the ODHX.

In Figure 2.15 (b), the system operates similarly with FLTMS except that the battery chiller manages the temperature of ESS in winter instead of LTR. Figure 2.15 (c) shows operation mode in moderate condition, RP and ODHX in CRLTMS replace coolant pump and LTR in CHPTMS so that liquid refrigerant in RSV sequentially flows the PEEM, battery chiller absorbing generated heat from the electric devices and ODHX rejecting heat to the ambient air. .

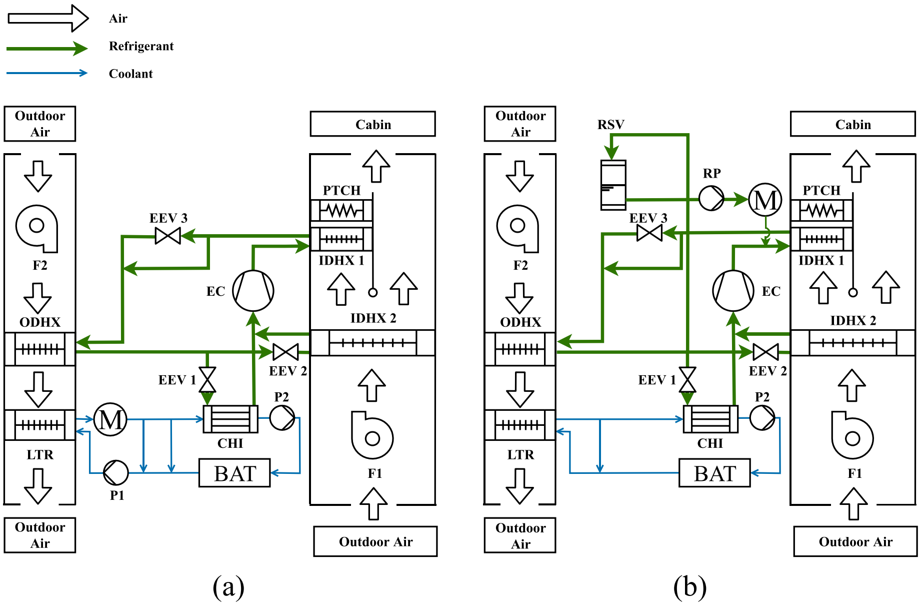

Figure 2.13 Schematic of (a) conventional heat pump and thermal management system and (b) floating loop heat pump and thermal management system

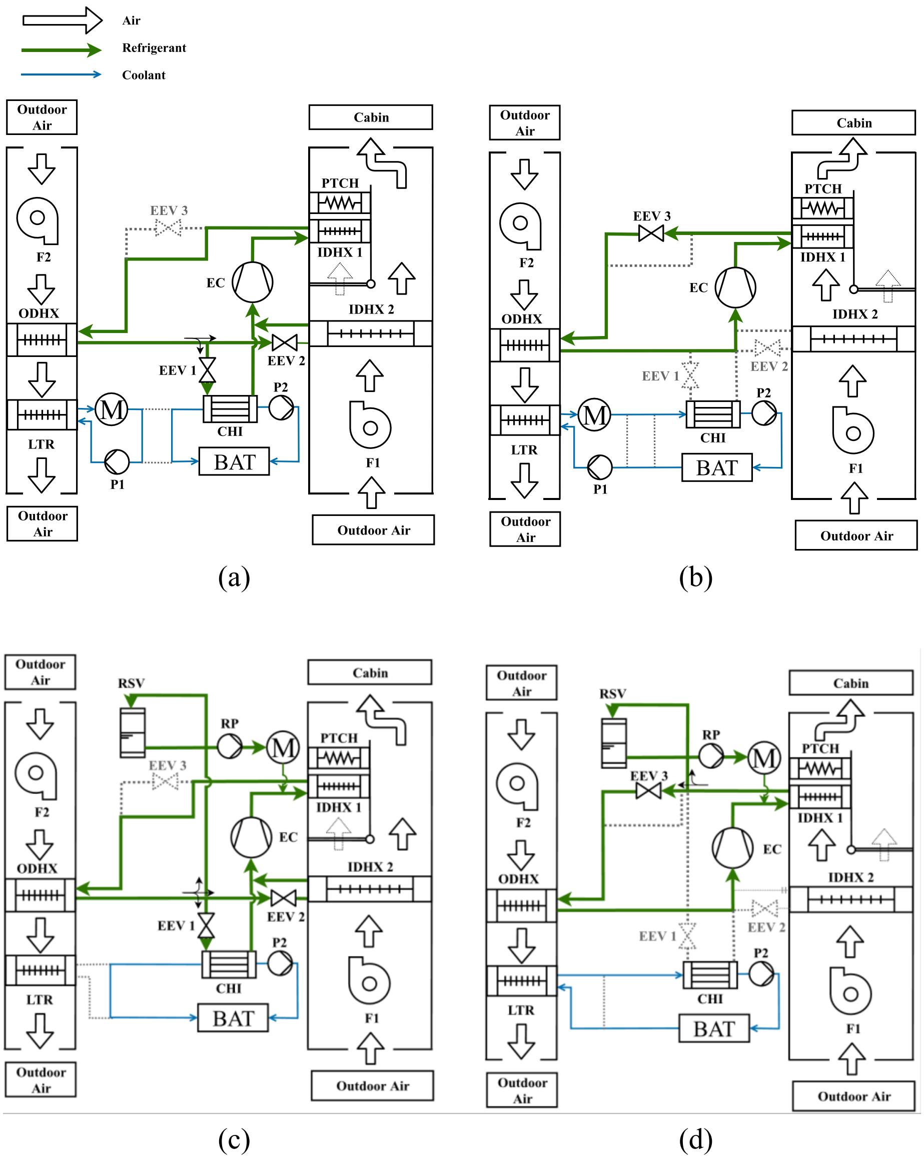

Figure 2.14 System configuration and fluid flows of CHPTMS when operating in (a) summer and (b) winter and FLHPTMS when operating in (c) summer and (d) winter

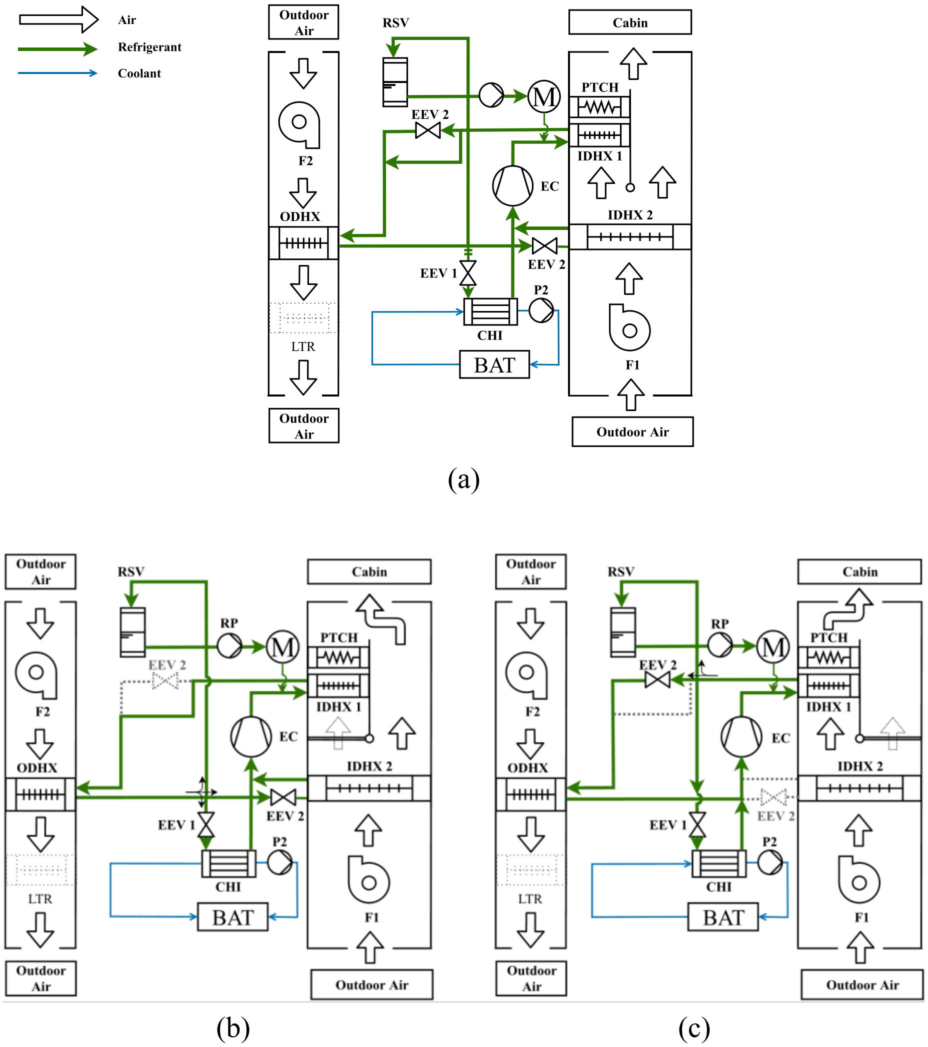

Figure 2.15 System configuration and fluid flows of (a) CRLTMS when operating in (b) summer and (c) winter

2.3.2. Model description

Five System models including CHPTMS, FLTMS and CRLTMS thermally consolidate heat pump model, electric device model and cabin thermal load model; heat pump system manages the thermal state of electric devices while affording the thermal load in cabin. Each model consists of several components. Component models are established based on theoretical and practical approach and validated with experimental data on each component.

Heat pump component model using R134a as a refrigerant are modeled and validated; of which the compressor model and the air-to-refrigerant model on former research [108] are integrated into the heat pump system model. Expansion process is assumed as isenthalpic process and expansion valves are assumed to properly control the opening area matching certain DSH of refrigerant. Thermodynamic properties of R134a are calculated from REFPROP [109].

Scroll compressor model estimates outlet enthalpy, mass flowrate of refrigerant, and electric power consumption. Enthalpy of discharged refrigerant is calculated from the thermodynamic state, suction pressure, and temperature of refrigerant. The compression process is assumed as a polytropic process [110] with a certain polytropic coefficient as presented in Eq. (2.6) where P and V

denote pressure and volume of refrigerant and subscript s and d represents suction and discharge state. n_{poly}, polytropic coefficient, acquired from experimental data. Considering the actual compression process, clearance volume exists so that a volumetric efficiency should be calculated to estimate mass flowrate of refrigerant. As presented in Eq. (2.7), volumetric efficiency η_v is thermodynamically derived with constant clearance volume ratio C, which is attained experimentally. Then, Eq. Eq. (2.8) calculates the actual mass flowrate $\dot{m}$ by multiplying volumetric efficiency and ideal mass flowrate of a compressor, which is calculated with a swept volume V_{swept} of refrigerant, suction density ρ_s, and rotational speed ω. The electric power consumption $\dot{W}$ of a compressor is calculated through mechanical efficiency η_m where the ideal work of compressor is the product of mass flowrate and enthalpy difference between suction and discharge state denoted as $h_d - h_s$ as presented in Eq. (2.9). The estimated value of outlet temperature, mass flowrate, and electric power consumption in various experimental conditions are within reasonable error with experimental data as shown in Figure 2.16.

$$\frac{P_s}{P_d} = \left(\frac{V_d}{V_s}\right)^{n_{poly}} \qquad \text{Eq. (2.6)}$$

$$\eta_v = \{1 - C\left[\left(\frac{P_d}{P_s}\right)^{\frac{1}{k}} - 1\right]\} \qquad \text{Eq. (2.7)}$$

$$\dot{m} = \rho_s \cdot \omega \cdot V_{swept} \cdot \eta_v \qquad \text{Eq. (2.8)}$$

$$\dot{W} = \dot{m}(h_d - h_s)/\eta_m \qquad \text{Eq. (2.9)}$$

Louvered-fin tube heat exchanger is widely used in conventional vehicle as an LTR due to high heat transfer rate in relatively small volume. Heat transfer between air and coolant is analyzed into three processes; convection between air and outer surface of LTR, conduction of LTR aluminum plate and convection between inner surface and coolant. First, convective heat transfer coefficient of air in louvered-fin heat exchanger is derived from Colbrunn j-factor correlation in Eq. (2.11) suggested by Chang and Wang [111]. Colbrunn j-factor is defined as presented in Eq. (2.10) with convective heat transfer rate h_t, mass flux G, specific heat capacity c_p and Prandtl number Pr. Eq. (2.11) correlates Colbrunn j-factor with Reynolds number Re and fin geometry including louver angle θ, fin pitch F_p, louver pitch L_p, fin length F_l, tube depth T_d, louver length L_l, tube pitch T_p and thickness of fin δ_f. Heat transfer area, which is another dominant factor in heat transfer along with heat transfer coefficient, is calculated based on fin efficiency [112] in Eq. (2.12). Fin efficiency η_f is defined as the ratio of actual heat transfer to maximum heat transfer, assuming the fin temperature is equal to the base temperature. Fin efficiency is derived as a function of fin length L_f and m that is defined as presented in Eq. (2.13). Conduction in aluminum plate is simply calculated from the thickness of plate and thermal conductivity of aluminum. Cool ant is a water/ethylene glycol (WEG) mixture with volumetric ratio of 0.5 to prevent freezing in cold condition. Heat transfer coefficient of coolant uses correlation in Eq. (2.14) presented by Kim et al [113], where reference Nusselt number Nu_{ref} in microtube is a function of tube aspect ratio γ as presented in Eq. (2.15). Eq. (2.16) - Eq. (2.18) defines fundamental dimensionless numbers. Then, overall heat transfer coefficient is obtained by integrating three heat transfer coefficients above into thermal resistance circuit. Finite difference method (FDM) is employed to consider the temperature gradient of coolant flowing through LTR. LTR tube is discretized into several elements and each element calculates heat transfer rate and temperature of coolant leaving the element. This process repeats until calculation of all the elements is completed with total heat transfer rate and LTR outlet temperature of coolant.

$$j = \frac{h_t}{Gc_p} Pr^{2/3} \qquad \text{Eq. (2.10)}$$

$$j = Re^{-0.49} \left(\frac{\theta}{90}\right)^{0.27} \left(\frac{F_p}{L_p}\right)^{-0.14} \left(\frac{F_l}{L_p}\right)^{-0.29} \left(\frac{T_d}{L_p}\right)^{-0.23} \left(\frac{L_l}{L_p}\right)^{0.68} \left(\frac{T_p}{L_p}\right)^{-0.28} \left(\frac{\delta_f}{L_p}\right)^{-0.05} \qquad \text{Eq. (2.11)}$$

$$\eta_f = \frac{tanh\left(mL_f\right)}{mL_f} \qquad \text{Eq. (2.12)}$$

$$\mathrm{m} = \sqrt{\frac{2h_t}{\mathrm{k_f}\delta_\mathrm{f}}} \qquad \text{Eq. (2.13)}$$

$$Nu = Nu_{ref} + 0.0499RePr\frac{D}{L} \quad \text{Eq. (2.14)}$$

$$Nu_{ref} = 7.541(1 - 1.969\gamma + 5.664\gamma^2 - 12.866\gamma^3 + 19.349\gamma^4 - 16.197\gamma^5 + 5.510\gamma^6) \quad \text{Eq. (2.15)}$$

$$Re = \frac{\rho VD}{\mu} \quad \text{Eq. (2.16)}$$

$$Nu = \frac{h_t L}{k} \quad \text{Eq. (2.17)}$$

$$Pr = \frac{\mu c_p}{k} \quad \text{Eq. (2.18)}$$

Three air-to-refrigerant heat exchangers, outdoor heat exchanger, indoor condenser, and indoor evaporator, are similarly modeled as louvered-fin tube heat exchangers in section 3.1.2. These models have an equal calculation process with LTR except for the working fluid, R134a, heat transfer coefficient. Yan's correlation [114] in Eq. (2.19) is applied to obtain the heat transfer coefficient of single-phase refrigerant. For condensing refrigerant, Nusselt number is correlated with equivalent Reynolds number Re_{eq} and liquid Prandtl number Pr_l as presented by Yan [115] in Eq. (2.20). Equivalent Reynolds number is defined based on the equivalent mass flux G_{eq} in Eq. (2.22), where $\mathrm{D_h}$ is a hydraulic diameter of tube and x is a quality of refrigerant and subscript l and g represent liquid and gas state.

$$\mathrm{Nu} = 0.2121\mathrm{Re}^{0.78}\mathrm{Pr}^{1/3} \quad \text{Eq. (2.19)}$$

$$\mathrm{Nu} = 4.118\mathrm{Re}_{\mathrm{eq}}^{0.4} \cdot \mathrm{Pr}_{\mathrm{l}}^{1/3}$$ Eq. (2.20)

$$G_{eq} = G[(1-x) + x\left(\frac{\rho_l}{\rho_g}\right)^{0.5}]$$ Eq. (2.21)

$$\mathrm{Re}_{\mathrm{eq}} = \frac{G_{eq}D_h}{\mu_l}$$ Eq. (2.22)

As a heat transfer coefficient of the evaporating refrigerant, Yan et al. [114] presented Nusselt number correlation in Eq. (2.23) with equivalent Reynolds number, liquid Prandtl number, and equivalent boiling number, which is defined in Eq. (2.24) with heat flux q''. In Eq. (2.26), total heat transfer can be divided into the convection heat transfer from the temperature difference between air and evaporator surface, which are denoted as T_a and T_s and latent heat Δi of condensed water moisture, the amount of which is a product of mass transfer coefficient h_m and the absolute humidity ω difference of air and surface. The mass transfer coefficient is derived from Lewis relation [112] in Eq. (2.26), assuming that Lewis number Le is approximately 1 for air. The surface temperature satisfying energy equation is numerically found with bisectional method with upper boundary of air temperature and lower boundary of refrigerant temperature. Results present the heat transfer rate and outlet humidity, of condenser and evaporator in various experimental conditions with reasonable estimation

$$Nu = 1.926 Re_{eq}^{0.5} Bo_{eq}^{0.3} Pr_l^{1/3}$$ Eq. (2.23)

$$Bo_{eq} = \frac{q''}{G_{eq}(h_g - h_l)}$$ Eq. (2.24)

$$q''_{tot} = h_t(T_a - T_s) + h_m(w_a - w_s)\Delta i$$ Eq. (2.25)

$$h_m = \frac{h_t}{c_p Le^{2/3}}$$ Eq. (2.26)

Plate heat exchanger which conveys heat from coolant to refrigerant is utilized as a battery chiller. Heat transfer coefficient of evaporating refrigerant is equally used as presented above and heat transfer coefficient of coolant is calculated through the Nusselt number correlation in rectangular channels suggested by Hartnett and Kostic [116] as presented in Eq. (2.27).

$$\mathrm{Nu}_{cool} = 8.235(1 - 2.0421\gamma + 3.085\gamma^2 - 2.477\gamma^3 + 1.058\gamma^4 - 0.186\gamma^5)$$ Eq. (2.27)

Figure 2.17 shows the thermal schematic of main electric components in PEEM and ESS; motor and battery. The two main purposes of TMS are to remove generated heat from these electric devices and maintain their thermal state within appropriate operating range. Therefore, heat generation model and thermal resistance model of ESS and PEEM are required to assess and compare the aforementioned systems. The thermal properties of materials in TMS are presented in Table 2.3, which were given by Chung et al [98].

PEEM drives the vehicle through electrical energy stored in ESS. Heat generation from PEEM is evaluated as a remainder of electric power input subtracting actual motor power output, which is commonly presented as a motor efficiency map. The motor efficiency depends on the rotating speed and torque of motor and the efficiency map is obtained from performance test. Kim verified the cooling performance enhancement of evaporative refrigerant in curved channel and established a lumped parameter thermal model, which consists of rotor, airgap, coil, stator and coolant as shown in Figure 2.17 (a). Rotor, stator and coil generate heat, which is dissipated through air and surrounding coolant jacket. Energy equation in cylindrical coordinate [112] is applied to properly estimate the temperature distribution of each components in motor with FDM. Kim [89] presented the heat transfer correlation of typical coolant and refrigerant including R134a and R245fa in curved channel with experiments. Heat transfer coefficient of coolant is calculated from the correlation in Eq. (2.29) suggested by Rogers et al. [117], where $\mathrm{d_{ch}}$ is hydraulic diameter of channel and D_{ch} is diameter of cooling jacket. In case of R134a, two correlations [118, 119] in Eq. (2.29) and Eq. (2.30) are used to obtain boiling heat transfer coefficient based on the vapor quality. When vapor quality is lower than 0.4, Chen's correlation in Eq. (2.29) is applied, where $\mathrm{Nu_l}$ is single-phase heat transfer coefficient in Eq. (2.28) and Lockhart-Martinelli parameter X_{tt} is defined in Eq. (2.30). When vapor quality is larger than 0.4, the correlation in Eq. (2.31) with mixture Reynolds number Re_m, convective boiling number N_{CB} and mixture Dean number $\mathrm{Dn_m}$ is defined in Eq. (2.32) – Eq. (2.34), respectively. Figure 2.18 (b) presents estimation results of coil temperature, which is target of PEEM TMS, in different vehicle driving condition, showing reasonable temperature error within 10%.

$$\mathrm{Nu} = 0.0023\mathrm{Re}^{0.8}\mathrm{Pr}^{0.4}\left(\frac{d_{ch}}{D_{ch}}\right)^{0.1} \quad \text{Eq. (2.28)}$$

$$\frac{\mathrm{Nu}}{\mathrm{Nu_l}} = 2.84\left(\frac{1}{X_{tt}}\right)^{0.27} + (46162Bo^{1.15} - 0.88) \quad \text{Eq. (2.29)}$$

$$where\ 0 \le x \le 0.4$$

$$X_{tt} = \left(\frac{1-x}{x}\right)^{0.9}\left(\frac{\rho_g}{\rho_l}\right)^{0.5}\left(\frac{\mu_g}{\mu_l}\right)^{0.1} \quad \text{Eq. (2.30)}$$

$$\mathrm{Nu} = 8.76\mathrm{Re_m^{0.6}}\mathrm{Pr_l^{1/6}}\left(\frac{\rho_g}{\rho_l}\right)^{0.2}\left(\frac{k_g}{k_l}\right)^{0.09}\mathrm{Dn_m^{0.1}}\mathrm{N_{CB}^{-0.414}} \quad \text{Eq. (2.31)}$$

$$\mathrm{Re_m} = \frac{Gd_{ch}}{\mu_l}[1 + \mathrm{x}\left(\frac{\rho_l}{\rho_g} - 1\right)] \quad \text{Eq. (2.32)}$$

$$\mathrm{N_{CB}} = \frac{[1 + \mathrm{x}\left(\frac{\rho_l}{\rho_g} - 1\right)]\left(\frac{\rho_g}{\rho_l}\right)^{\frac{1}{3}}}{\mathrm{Bo}} \quad \text{Eq. (2.33)}$$

$$\mathrm{Dn_m} = \mathrm{Re_m}\left(\frac{d_{ch}}{D_{ch}}\right)^{1/2} \quad \text{Eq. (2.34)}$$

As presented in Figure 2.17 (b), ESS has a structure of battery cell surrounded by insulation case and metal fin, which conveys generated heat from cell to coolant through thermal pad. Thermal model suggested by Chung et al. [98] is applied. Energy equation in Cartesian coordinate [112] is applied considering rectangular shape of battery cell and cooling plate with FDM. Two types of heat generation from lithium-ion battery exist; irreversible heat generation from the internal resistance of battery cell and reversible heat generation from the entropy change in chemical reaction process, as presented in Eq. (2.35). Irreversible heat is derived from the relation that operating voltage V_b decreases from open-circuit voltage E by the product of internal resistance R and operating current I based on the electric circuit of battery. Reversible heat is calculated from entropy change Δs presetnd by Viswanathan et al. [120] and the current-mol relation with Faraday constant F and mole number in reaction n. The heat transfer coefficient of coolant is calculated with correlation in Eq. (2.15). Battery thermal model is validated with experimental data in various driving conditions, presenting temperature error within reasonable range as shown in Figure 2.18 (a).

$$Q_{tot} = Q_{irr} + Q_{rev} = I(E - V_b) + IE\frac{dE}{dT} = I^2R - T\Delta s\frac{\mathrm{I}}{nF} \qquad \text{Eq. (2.35)}$$

Aforementioned models are combined into an integrated heat pump and thermal managements system according to the operating mode of each configuration as presented in Figure 2.19. Cabin model proposed by Zhang et al. [46] estimates thermal load of cabin with given solar radiation, outdoor condition, and passenger information. Bisection method is mainly employed to find a steady-state solution satisfying certain target conditions. For heat pump model, cabin model determines heating or cooling demand of cabin to maintain thermal comfort condition in cabin. First iteration loop begins with DSH 5 K condition of refrigerant entering compressor and matches the DSH of refrigerant from evaporator by adjusting low pressure with bisectional method. Second iteration loop adjusts high pressure of the heat pump cycle to match the target the degree of subcool (DSC) of refrigerant sub-cooled through condenser. Target DSC is 5 K, which is an indicator that the refrigerant is properly charged without unstable expansion from two-phase refrigerant. Third iteration loop finds rotational speed of compressor satisfying the heating or cooling demand calculated with thermal load model. Then, thermal state of TMS is determined from heat pump calculation results. From dynamic electric device models established, steady-state solution is found through Gauss-Seidel method [121], which ensures fast and stable convergence with diagonally dominant condition. Coolant temperature of LTR loop is determined with point-Jacobi method [121]

satisfying energy balance of dissipated heat through LTR and generated heat from electric devices by updating the assumed coolant inlet temperature as calculated returning coolant temperature. The volume flowrate of coolant is set as 10 LPM. Floating loop has constant mass flowrate of 10 g/s. Mass flowrate of refrigerant through battery chiller is controlled to match target battery temperature of 20°C in winter and 30°C in summer. System modeling conditions are summarized in Table 2.4.

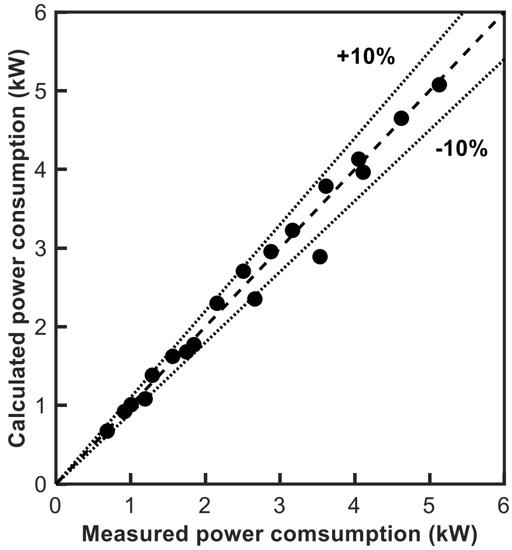

(a)

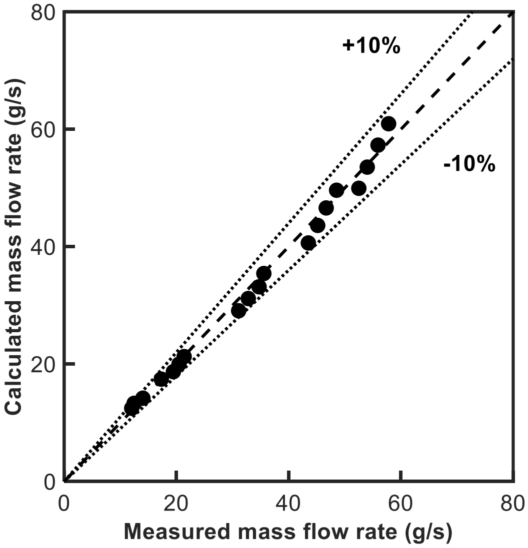

(b)

Figure 2.16 Compressor model validation in (a) power consumption, (b) mass flowrate and with 10% error line .

(a)

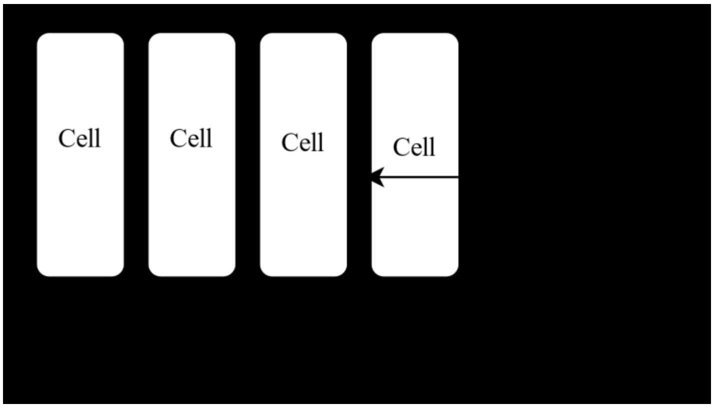

(b)

Figure 2.17 Thermal schematic of (a) motor and (b) battery

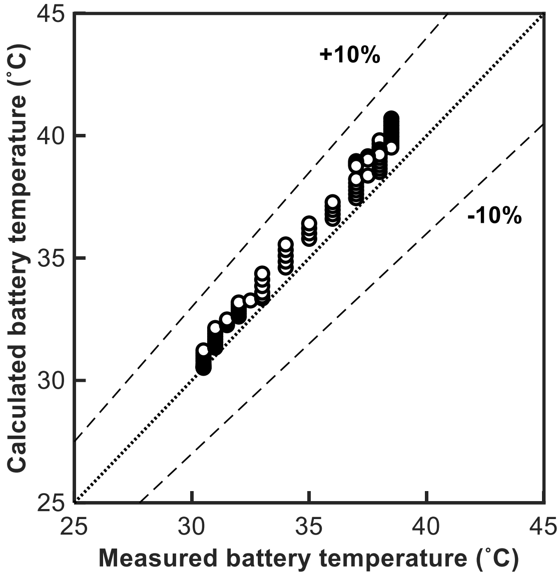

(a)

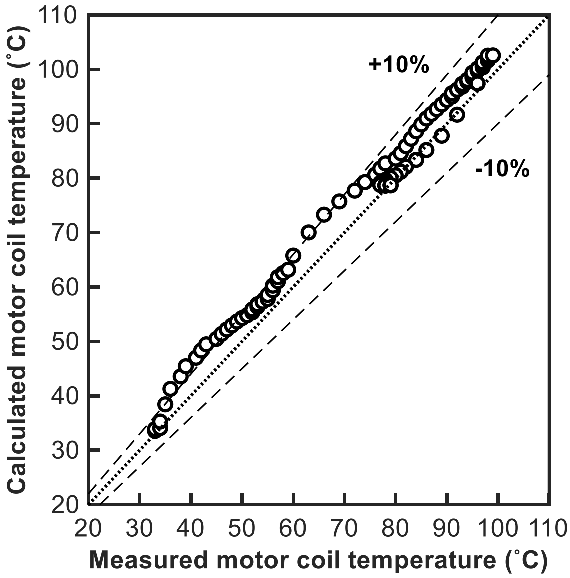

(b)

Figure 2.18 Validation results of (a) averaged battery temperature and (b) motor coil temperature with 10% error line

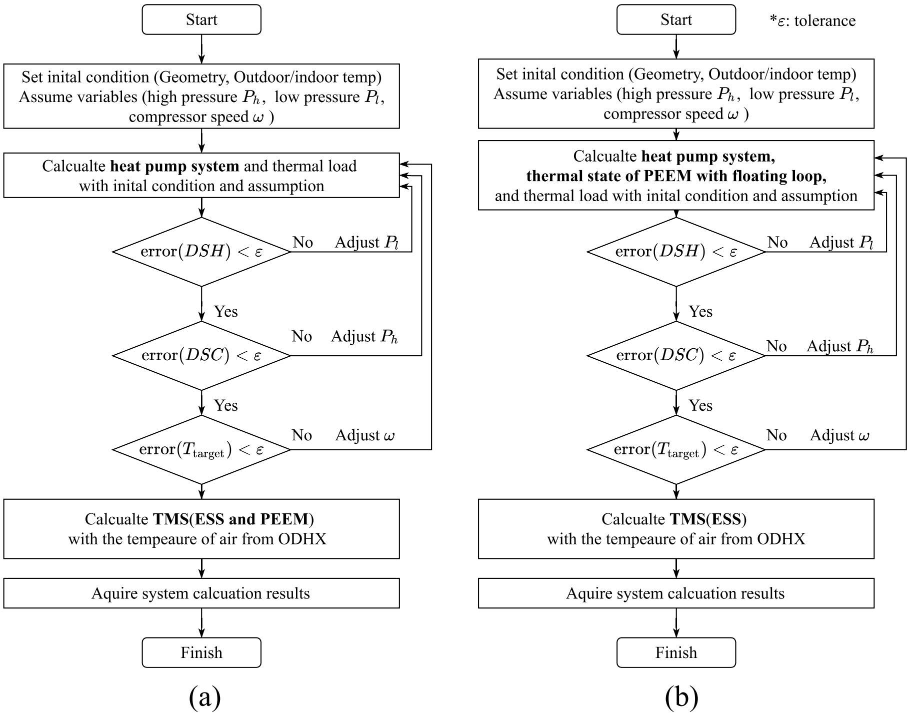

Figure 2.19 Flowchart of the simulation in (a) CHPTMS and (b) FLTMS

Table 2.3 Thermal properties of materials in TMS

Material	ρ (kg/m^3)	c_p (J/kgK)	k (W/mK)
Aluminum	2700	903	170
Copper (coil)	8960	388	400
Iron (stator and rotor)	7860	449	80
Battery cell	1780	1000	30
Insulation case	2300	1430	1.5
Thermal pad	3100	930	5.0

Table 2.4 System modeling conditions

Condition	Value
Ambient air temperature (°C)	-20 ~ 15 (winter) 35 ~ 45 (summer)
DSH and DSC (K)	5
Rotational speed of compressor (rpm)	0 ~ 9450
Battery temperature (°C)	20 (winter) 30 (summer)
Mass flowrate in floating loop (g/s)	10
Solar intensity (W/m^2)	0 (winter) 800 (summer)
Volumetric flowrate of coolant (LPM)	10
Number of passengers (person)	2
Body height of passenger (m)	1.7
Body weight of passenger (kg)	60

2.3.3. Results and discussion

Figure 2.20 (a) presents the total power consumption including compressor power and PTC heater, which only operates when the heating demand is not satisfied by the heat pump system. Compared with CHPTMS, FLTMS and

CRLTMS save the net power consumption in various climate conditions due to the waste heat recovery in floating loop. Power savings increase up to 23.2% with the smallest volumetric ratio of LTR (α) of 0.2 and 27.7% in CRLTMS, which absorbs heat from the ambient air with larger heat transfer area of ODHX. FLTMS and CRTMS require less mass flowrate of compressor than CHPTMS as shown in Figure 2.20 (b) due to the supplementary refrigerant injection in floating loop. Compressor speed is controlled to match the target heating demand of cabin until the compressor reaches its mechanical speed limit of 9,450 rpm. The convex trend of mass flowrate occurs with two principles; lower ambient temperature entails higher ambient load and heating demand of cabin, which requires more mass flowrate of refrigerant, and when the compressor reaches speed limit, mass flowrate decreases with the low suction density of refrigerant which absorbs heat from ambient air with low temperature at low presszure. Mass flowrate is in similar range with moderate outdoor condition where the size of ODHX does not affect the total heat transfer rate. However, as the ambient temperature becomes lower, the difference of heat absorbed from low ambient air in FLTMS becomes larger and FLTMS with smaller α provides heat to cabin at higher temperature and pressure as presented in Figure 2.21 (a). Higher temperature and pressure of air provided in cabin entail less power consumption of PTC heat and total power consumption.

Figure 2.21 (b) shows the motor coil temperature of each TMS presenting that the motor coil is managed under the temperature limit of 120°C. CHPTMS utilizes cold outdoor air with LTR to cool down motor in winter so that the temperature of motor coil lowers with cold ambient condition. The motor coil temperature also represents the thermal level of recovered waste heat in FLTMS and CRLTMS. Therefore, higher thermal level of waste heat recovery saves more power consumption of the compressor, which operates to obtain certain thermal condition of refrigerant through compression process to provide heat.

Figure 2.22 (a) presents the exergy transfer rate from PEEM, which is defined with the product of heat transfer from PEEM and Carnot fraction, as shown in the equation: $\phi = Q \cdot (1 - \frac{T_{outdoor}}{T_{PEEM}})$. Carnot fraction is determined by the heat source temperature T_{PEEM} and the outdoor temperature $T_{outdoor}$ and represents the ratio of maximum useful work from the heat source to the environment. In FLTMS and CRLTMS, PEEM maintains a higher thermal level than CHPTMS so that the thermal values of heat generated from the PEEM increase, which shows the superiority of floating loop thermal management of FLTMS and CRLTMS in winter. The temperature of PEEM follows the trend of refrigerant pressure in the floating loop presented in Figure 2.22 (a). As the ambient temperature decreases, the exergy transfer rate of FLTMS increases due to the lower heat sink temperature, which also presents that the higher thermal level of PEEM is more valuable in severely cold conditions.

Considering the downsized volume of LTR, FLTMS would fail to maintain ESS within a proper thermal state. However, Figure 2.22 (b) shows that FLTMS with smaller LTR can manage heat generation from ESS maintaining the battery temperature under the upper limit of 35°C because the inlet air temperature of LTR becomes lower with larger ODHX absorbing heat from ambient air. Considering that the resultant temperatures of the battery in Figure 2.22 (b) are calculated assuming constant volumetric flowrate of coolant, thermal management of ESS can be achieved by balancing the self-heating effect of ESS and mass flowrate with proper control of coolant flowrate.

The floating loop is advantageous in the perspective of waste heat recovery in cold conditions. However, the heat generation from PEEM in summer burdens an extra cooling load to the ODHX so that additional heat transfer area is required through reallocation of LTR and ODHX. In summer, an auxiliary cooling device does not exist which can operate when the cooling demand is not satisfied such as a PTC heater in winter. Therefore, the target temperature of air provided in the cabin cannot be reached in harsh conditions.

Figure 2.23 (b) shows the outlet temperature of air provided in the cabin, which should decrease considering the ambient load increase in higher outdoor temperature conditions. However, the provided air temperature shows an increasing trend at high ambient air temperature after the compressor speed reaches its upper limit. Only when a sufficient heat exchange area of OHDX is obtained (α is smaller than 0.2), the cooling performance of FLTMS and CRLTMS is comparable with that of CHPTMS. Otherwise, the provided air temperature trends in Figure 2.23 (b) show total failure in cooling especially when α is 0.6 and 0.8, which present completely different trend with other cases. Figure 2.23 (a) presents the power consumption of the compressor that decreases with smaller α because larger OHDX can dissipate more heat to the ambient air. FLTMS does not operate LTR in summer when the battery chiller and floating loop manage the temperature of ESS and PEEM, which means larger ODHX is advantageous in any perspective. However, additional heat rejection requirement deteriorates the cooling performance of FLTMS compared with CHPTMS as presented in Figure 2.23 (a) showing that the compressor consumes more power with insufficient ODHX size. Power consumption of compressor is saved up to 3.8% in CRLTMS and 2.4% in FLTMS with α of 0.2 compared with CHPTMS, in which resultant power savings are much less than that in winter. Figure 2.24 (c) presents the heat exchanger

efficiency of the evaporator, which is calculated as $\eta_{HX} = \frac{T_{air_{in}} - T_{air_{out}}}{T_{air_{in}} - T_{ref_{sat}}}$; the ratio of actual heat transfer to maximum heat transfer. The result shows that the heat exchanger efficiency sharply decreases in FLTMS with large α due to a small heat exchange area with large temperature difference and cooling demand. FLTMS with α of 0.2 and CRLTMS show slightly better heat exchanger efficiency than CHPTMS with a large enough heat exchanger area.

Even though the floating loop utilizes liquid refrigerant at high temperatures to cool down the PEEM, the temperatures of the motor coil are managed under the temperature limit of 120°C as shown in Figure 2.24 (d) when α is small enough to radiate the heat generation from PEEM through the ODHX. CRLTMS and FLTMS with α of 0.4 and 0.2 show better cooling performance than CHPTMS even with a less mass flowrate of working fluid and pump work, which originates from the higher heat transfer coefficient of two-phase refrigerant.

Refrigerant flow from the compressor is separated into two passes: evaporator and battery chiller as shown in Figure 2.25 (a). As the battery chiller requires more mass flowrate of refrigerant to manage the battery temperature in high ambient air temperature conditions, cooling capacity decreases because less refrigerant passes through the evaporator. Therefore, the total mass flowrate of the compressor should increase to match the ambient load at high

temperatures until the speed of the compressor reaches its limit. While compressor speed is set as its maximum, the mass flowrate of the refrigerant is affected by the pressure ratio of the compressor. As shown in Figure 2.25 (b), the pressure of the evaporator stays within a narrow range due to relatively constant heat source temperature; whereas, the pressure of the condenser increase with a higher ambient temperature, which is a heat sink of the heat pump system. However, the dependency of condensing pressure on the ambient temperatures shows different trends in CHPTMS and floating loop systems. Because the floating loop supplies more refrigerant in the condenser, the condensing pressure increases rather insensitively, while the condensing pressure of CHPTMS is directly and solely affected by the ambient temperature. Those pressure trends produce the convex shape of total mass flowrate in CHPTMS and a mildly increasing shape in FLTMS and CRLTMS.

To summarize the result above, the floating loop compactly recovers heat from the PEEM, which is advantageous in the perspective of waste heat recovery in winter and disadvantageous in the perspective of additional cooling load of the heat pump in summer. Therefore, the performance improvement is more prominent in winter where the waste heat can be directly provided in the cabin. The floating loop system is also superior to the conventional system even in summer by allocating more heat exchange areas on ODHX. However, the improvement is relatively small because waste heat itself is a thermal burden in summer.

The system with the largest refrigerant heat exchanger is the best FLTMS mainly considering the power reduction especially in severe condition as shown in Figure 2.20 (a) and Figure 2.23 (a). FLTMS in the selected system also satisfies each thermal requirement of ESS and PEEM. Figure 2.6 (b) and Figure 2.24 (d) show that the system properly operates maintaining the electric devices within a proper temperate range. However, consideration of manufacturing cost is required to evaluate the floating loop idea. Even though the total heat exchanger size is confined and the LTR and OHDX have equal fin-type and material, an additional refrigerant pump with similar operating condition and specification weighs about 7.7kg, which is much heavier and has a larger volume than the coolant pump (about 1kg).

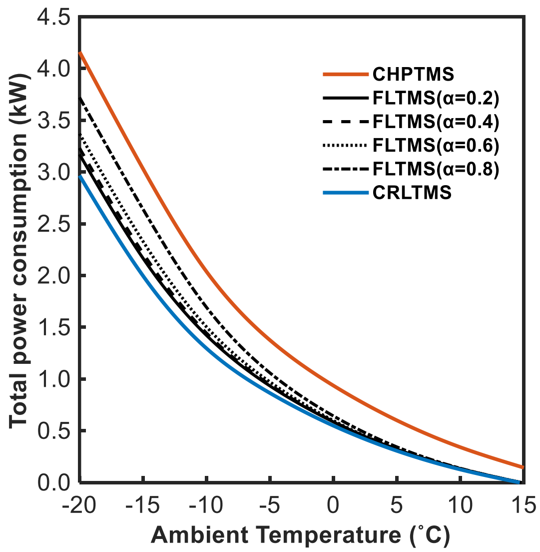

(a)

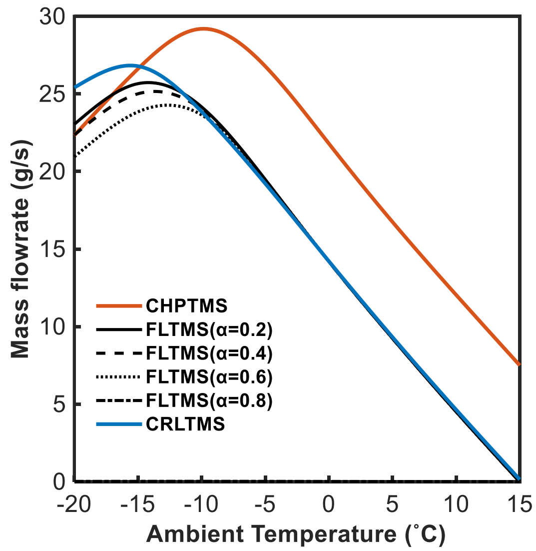

(b)

Figure 2.20 System performance and thermodynamic state of CHPTMS, FLTMS and CRLTMS with different ambient temperature condition in winter: (a) Total power consumption, (b) mass flowrate of compressor

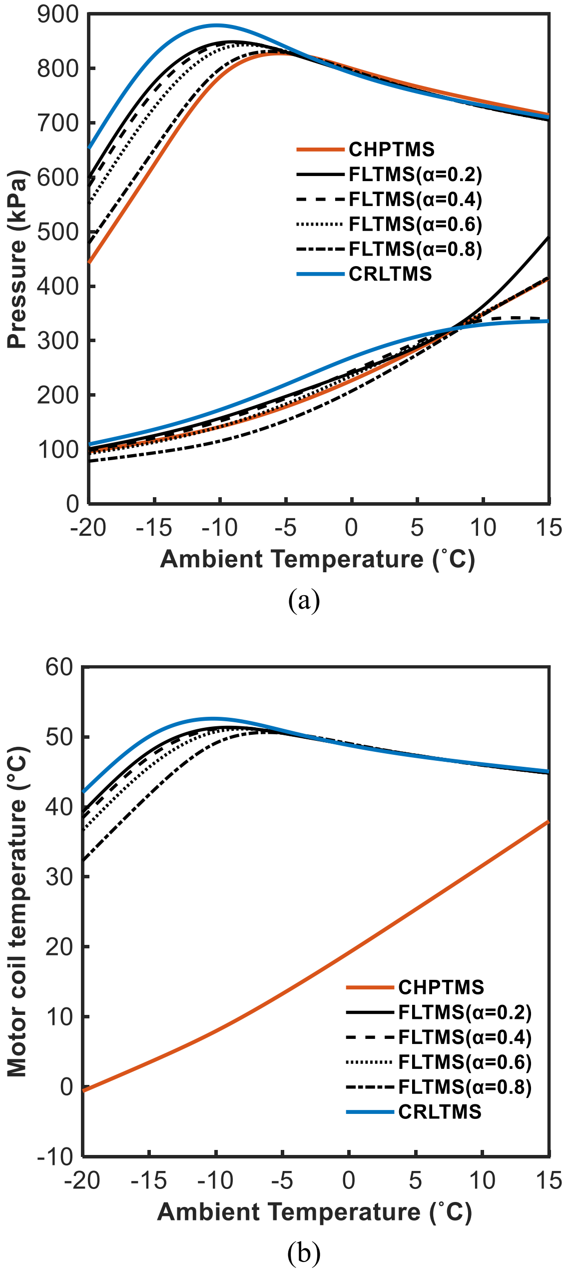

Figure 2.21 System performance and thermodynamic state of CHPTMS, FLTMS and CRLTMS with different ambient temperature condition in winter: (a) pressure and (b) motor coil temperature

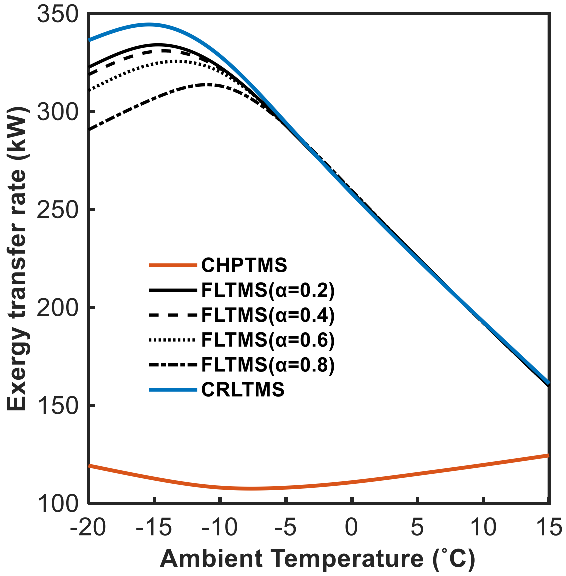

(a)

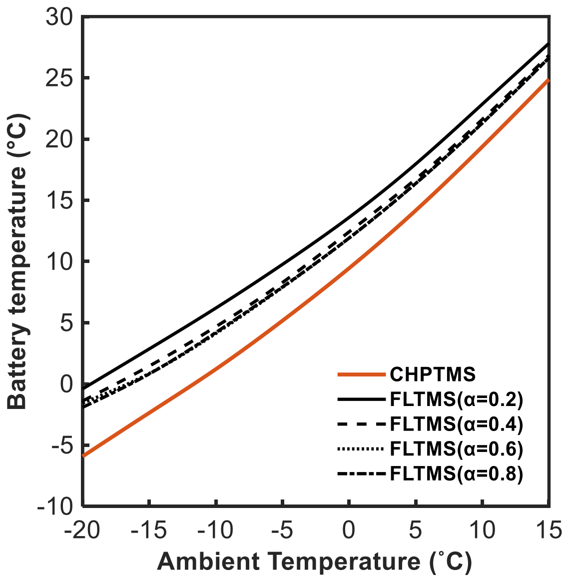

(b)

Figure 2.22 PEEM evaluation as a heat source with (a) exergy transfer rate of CHPTMS, FLTMS and CRLTMS and (b) battery temperature of CHPTMS and FLTMS in winter

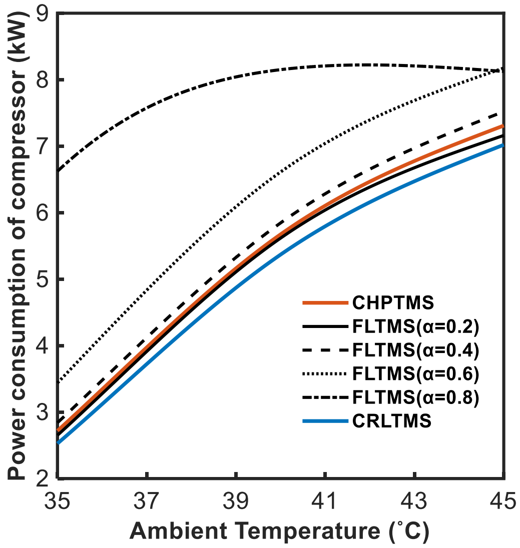

(a)

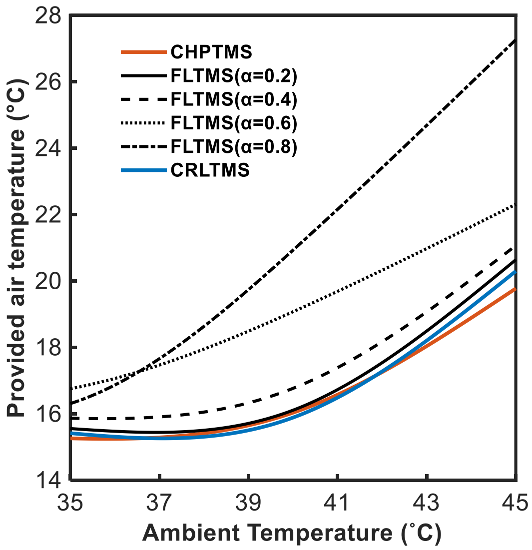

(b)

Figure 2.23 System performance and thermodynamic state of CHPTMS, FLTMS and CRLTMS with different ambient temperature condition in summer: (a) compressor power consumption, (b) temperature of air provided in cabin

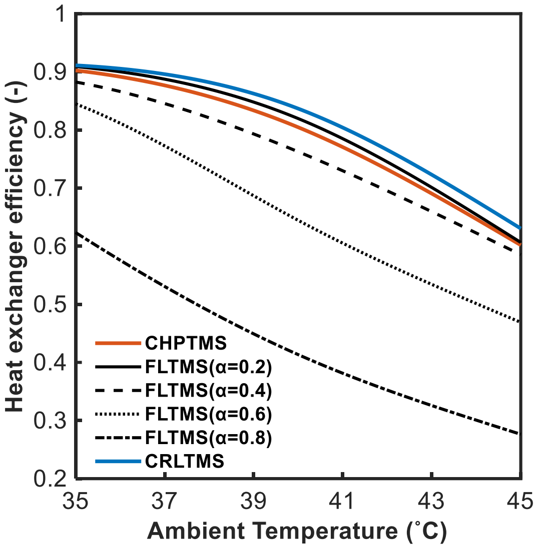

(a)

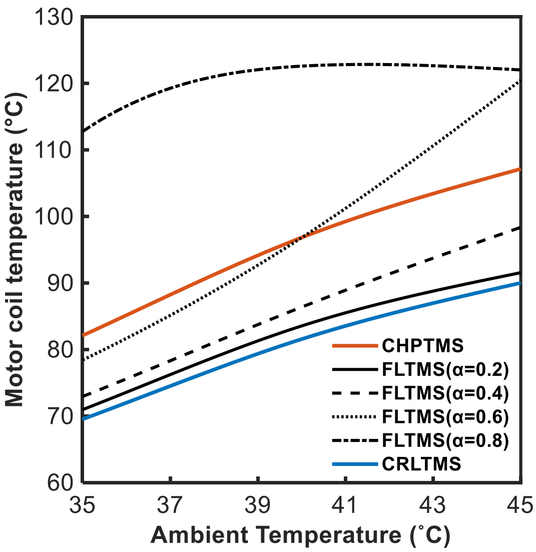

(b)

Figure 2.24 System performance and thermodynamic state of CHPTMS, FLTMS and CRLTMS with different ambient temperature condition in summer: (a) heat exchanger efficiency and (b) motor coil temperature

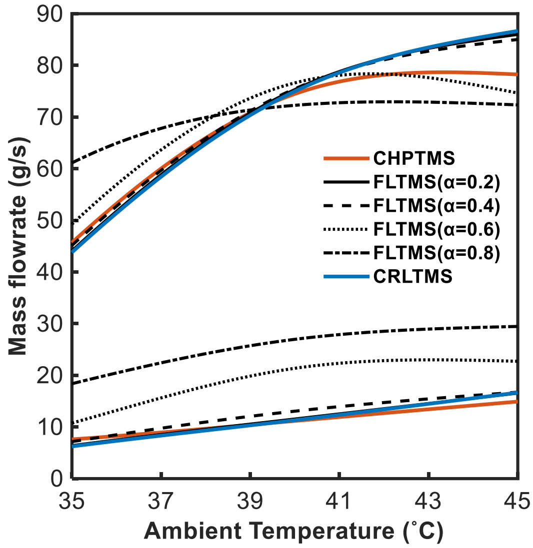

(a)

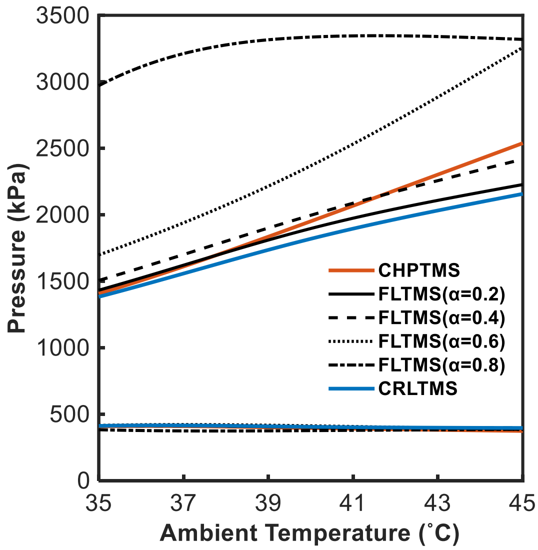

(b)

Figure 2.25 Thermodynamic state of CHPTMS, FLTMS and CRLTMS in summer: (a) mass flowrate of compressor (upper) and chiller (lower) and (b) pressure of condenser (upper) and evaporator (lower)

2.4. Summary

In this chapter, the performance of a MWHR system utilizing the vapor injection technique was investigated under various operating conditions, including outdoor air temperature, amount of waste heat, and the compressor speed. The experimental results show that the heating capacity of the MWHR system outperforms that of the CWHR system with various system operating conditions. The MWHR system transfers the waste heat from the electric device to the heat pump system at an intermediate temperature, which is a higher energy level than CWHR system. Therefore, the heating capacity increased up to 72.5% when the heat pump operated in the coldest condition of -20 °C. Even though the coefficient of performance of two waste heat recovery systems was within a similar range, MWHR system outperformed conventional waste heat recovery system at the ambient temperature of -10 °C. This performance enhancement became more prominent especially when the CHWR system was incapable of utilizing an air source because of insufficient mass flow rate through the evaporator. This incapability occurs when the total mass flow rate decreases with a lower compressor speed or when the waste heat recovery system requires a large portion of total mass flow rate to dissipate large amount of waste heat; this problem does not arise in a MWHR system owing to the vapor injection technique. In addition, MWHR system managed the temperature level of ESS within a proper range from 15 °C to 35 °C except for unusual cases with heat generation exceeding 2 kW.

Heat pump and thermal management system employing floating loop concept is suggested; a system including floating loop and coolant loop (FLTMS) and refrigerant-only loop (CRLTMS). Conventional heat pump and thermal management system (CHPTMS) is compared with the proposed systems with experimentally validated model integrating the component characteristics in heat pump system and thermal management system. Considering changes in thermal load distribution with floating loop, the volumetric ratio α of the refrigerant heat exchanger (outdoor heat exchanger) and coolant heat exchanger (low temperature radiator) is reallocated with finite heat exchanger volume. The following conclusions were obtained.

(1) In winter, the refrigerant passing through the floating loop absorbs heat generated from PEEM, which saves the power consumed in compressor and PTC heater in various climate conditions. Results verified power savings up to 23.2% in FLTMS when α is 0.2 and 27.7% in CRLTMS. The size of refrigerant heat exchanger affects the heat exchanger efficiency and heating capacity of heat pump system especially in severely cold condition.

(2) In summer, the floating loop provides extra cooling demand of the heat pump system. However, by reallocating heat exchangers with finite heat

exchanger volume, the power consumptions of compressor are saved up to 3.8% in FLTMS when α is 0.2 and 2.4% in CRLTMS. Although the performance enhancement is not prominent as that in winter, the FLTMS and CRLTMS shows positive effect compared with CHPTMS.

(3) The larger volumetric ratio of outdoor heat exchanger monotonically increases the performance of heat pump system, presenting CRLTMS as the best system configuration. However, the results can provide guidelines for weighing the relative advantages of FLTMS considering the cost of entire revision of conventional heating, ventilation and air conditioning (HVAC) system in vehicle necessary to employ CRLTMS.

Chapter 3. Multi-level thermal management system[3]

3.1. Introduction

Considering the absence of an abundant waste heat from the case of internal combustion engine, EV requires delicate utilization of waste heat from electric devices. Many researchers suggested novel TMS structures [11–14], integrating thermal management system (TMS) with heat pump system. Leighton et al. [23] suggested combined fluid loop system, using secondary fluid system to modularize the heat pump and strengthen the thermal connectivity. Other studies [16–19] were conducted on the effect of waste heat recovery on the heat pump system, but the waste heat was recovered at only two temperature levels: condensing temperature and evaporating temperature. The difference between the two temperature levels widens in cold condition so that the waste heat recovery at either high [59] or low temperature [21–23] became less efficient. Lee at al. [61] subdivided the temperature into three levels with vapor injection technique and experimentally demonstrated that the heating capacity increases up to 72% when the waste heat is recovered at the

[3] The contents of chapter 3 were published as in *Applied Energy* [144] on 2023

intermediate temperature level. However, those studies focused on the performance of WHRS at one representative temperature level, even though the optimal temperature level changes depending on the ambient temperature and driving profile.

This study investigated the performance of different WHRSs, utilizing three temperature levels, one of which is achieved by a vapor injection technique. To estimate the performance of WHRSs, heat pump experiments were conducted, including waste heat recovery with an electric heater to simulate the waste heat from an electric motor. A transient heat pump model and electric motor model were established based on the experimental data to analyze the performance of each WHRS with actual driving conditions. The established ITMS model investigated the performance of each WHRS and suggested the optimal WHRS under a given driving condition. We expect that the optimal WHRS, suggested by the ITMS model, contributes to the driving range extension when implemented on EV computational system.

3.2. Model description

3.2.1. Scroll compressor modeling

Conventionally, the injection process was assumed as that the injection occurs between two pressures, injection pressure and one main pressure in compression chamber [49], like two-stage compression. The two-stage approximation assumed that the averaged flow rate of injected refrigerant can be derived by finding main pressure, which corresponds to the averaged pressure in the compression chamber. However, the injection process is a consecutive process where the pressure of injected chamber continuously increases, as shown in Figure 3.1. The pressure of compression chamber rises by both compression and injection, which consequently affects the injected mass flow rate. Therefore, the main pressure should be determined by various parameters, which are not constrained by flash tank or internal heat exchanger in MWHR. In addition, the dynamic behavior of MWHR system cannot be estimated with one main pressure as the injection occurs even when the injection pressure is lower the averaged main pressure. Thus, we established a novel injection model.

Figure 3.2 shows experimental setup for two-mirror Schlieren system for visualizing vapor injection process. An LED light was used as a light source and a condensing lens focused the light into a point source. The point light source at the focus of a parabolic mirror generated a collimated beam, passing through the test section. The beam was then reflected another parabolic mirror and concentrated into a point source, where the knife edge located. When the collimated beam passed though the test section, the beam refracted by the density difference of refrigerant in the test section. The refraction caused a change of light path blocked by the knife edge, and resultant light intensity changed as the density difference in the test section. A high-speed camera captured the density gradient of the test section in the injection process.

The test section consisted with two ports; the injection port injected refrigerant into test section and the compression port generated the pressure wave to increase the total pressure of the test section. The opening and closing timing of two ports were controlled by timing relay, which can designate the timing of electric signal with 0.01 s accuracy. A solenoid valve opened or closed the compression port according to the signal from the timing relay, determining the pressure of the test section when injection initiated and ended. A pneumatic ball valve was used, having similar opening mechanism with actual injection, which opens an injection port by sliding of an orbiting scroll. A refrigerant from a refrigerant tank filled the refrigerant in front of two valves, and the pressures were controlled by pressure regulator.

Figure 3.3 shows the experimental results with injection flow at initial stage and flow decaying in the continuously compressed chamber. As the injection was motivated by the pressure difference between the chamber and upstream of injection port, the mass flow rate of injected refrigerant decreased with increasing pressure of the chamber. The pressure of chamber was affected by both the compression and injection simultaneously. Therefore, those effect should be considered. On the other hand, the injected flow shows the jet impingement behavior, reaching the bottom plate of scroll wrap. Martin et al. [122] presented that the jet impingement enhances the heat transfer between the injected vapor and the plate. The heat transfer characteristic was reflected on the injection model below.

A scroll compressor model was established to estimate the thermodynamic state of refrigerant after compression and injection process. The compression process was divided in into three processes: suction, compression with injection, and discharge. The thermodynamic states of refrigerant were determined by three main phenomena: external work (compression), mass inflow and outflow (injection, suction, and leakage), heat transfer (to the adjacent chambers, plates, and ambient). The volume change, leakage length, and heat transfer area were derived based on the analytical equation of involute curve [123]. The enlarged dual-port in the left side of Figure 3.6 shows the area of injection port, which has port radius of r_{inj} and distance from the center of port to the orbiting scroll d. The opened port area was calculated by assuming the non-entirely opened port as a segment, as $\pi r_{inj}^2[1 \pm \sin(2acos(r_{inj}/d)]$, considering the large radius of involute curve compared with the radius of the injection hole.

$$\rho_{n+1} = \{\rho_n \cdot V_n + (\dot{m}_{in} - \dot{m}_{out})\Delta t\}/V_{n+1} \quad \text{Eq. (3.1)}$$

$$u_{n+1} = \{u_n \cdot m_n + (\dot{m}_{in}h_{in} - \dot{m}_{out}h_{out} + Q)\Delta t + P_n(V_n - V_{n+1})\}/m_{n+1} \quad \text{Eq. (3.2)}$$

$$X_{n+1} = f(\rho_{n+1}, u_{n+1}) \quad \text{Eq. (3.3)}$$

$$\mathrm{Nu}_{spr} = 0.23 \cdot \mathrm{Re}^{0.8}\mathrm{Pr}^{0.4}(1.0 + 1.77\frac{D_h}{r_{avg}}) \quad \text{Eq. (3.4)}$$

$$\overline{\mathrm{Nu}}_{inj} = \left[1 + \left(\frac{\frac{H}{D_h}}{\frac{0.6}{\sqrt{f}}}\right)^6\right]^{-0.05} \sqrt{f}\frac{1 - 2.2\sqrt{f}}{1 + 0.2\left(\frac{H}{D_h} - 6\right)\sqrt{f}} \mathrm{Re}^{2/3}\ \mathrm{Pr}^{0.42} \quad \text{Eq. (3.5)}$$

$$\dot{m} = C_d A \left\{P_{up} \cdot \rho_{up} \cdot \frac{2k}{k-1}\left[\left(\frac{P_{dw}}{P_{up}}\right)^{\frac{2}{k}} - \left(\frac{P_{dw}}{P_{up}}\right)^{\frac{k}{k+1}}\right]\right\}^{0.5} \quad \text{Eq. (3.6)}$$

$$\text{if } \left(\frac{P_{dw}}{P_{up}}\right) \geq \left(\frac{2}{k+1}\right)^{\frac{k+1}{k-1}}$$

$$\dot{m} = C_d A \left\{P_{up} \cdot \rho_{up} \cdot k \cdot \left(\frac{2}{k+1}\right)^{\frac{k+1}{k-1}}\right\}^{0.5} \quad \text{Eq. (3.7)}$$

$$\text{if } \left(\frac{P_{dw}}{P_{up}}\right) \leq \left(\frac{2}{k+1}\right)^{\frac{k+1}{k-1}}$$

$$\dot{W} = \sum P_n(V_n - V_{n+1})/\eta_{mech} \qquad \text{Eq. (3.8)}$$

Eq. (3.1) and Eq. (3.2) presents mass and energy equation, deriving the density ρ and specific internal energy u at the next angle $n+1$ (subscript) with the properties at the present angle n (subscript). The change of specific internal energy is summation of energy inflow and outflow; heat transfer; and external work, which can be expressed as a product of mass flow rate $\dot{m}$, enthalpy h, and time step Δt; heat transfer rate Q for Δt; and pressure P and volume change $V_n - V_{n+1}$, respectively. The derived density and specific internal energy determine other thermodynamic properties X. The heat transfer coefficient without injection was derived by the Nusselt number Nu correlation on the spiral heat exchanger [124], presented in Eq. (3.4) as a function of Reynolds number Re, Prandtl number Pr, and hydraulic diameter D_h, and averaged radius r_{avg} of chamber. On the other hand, as jet impingement has distinctive heat transfer characteristics, another Nusselt number correlations should be used to derive heat transfer coefficient during injection. The injection flow within confined chamber shows similar behavior with array of nozzles [122]. As show in Fig.--, the array of nozzles forms a fountain, which is also similar observed in the jet with confining wall because of symmetry in the nozzle array. Eq. (3.6) presents the space-averaged Nusselt number $\overline{\mathrm{Nu}}$ correlation with height H and hydraulic diameter of chamber, and relative nozzle area f, which is a ratio of nozzle area to total area.

The mass flow rate through the scroll clearance and injection port was assumed as an orifice flow. Mass flow rate of refrigerant $\dot{m}$ was mainly determined by pressure of upstream and downstream, denoted as P_{up} and P_{dw}, respectively, and specific heat ratio k. A drag coefficient C_d and orifice area A were derived with experimental data or design parameter. The pressure ratio of downstream to upstream decided whether the flow was choked or not. Eq. (3.6) is used when the flow was not chocked, and Eq. (3.7) is used when choked, determined by comparing actual pressure ratio with critical pressures ratio. The power consumption of compressor $\dot{W}$ were summation of each compression work at angle divided by mechanical efficiency η_{mech}, as presented in Eq. (3.8).

Figure 3.4 and Figure 3.5 presents the validation results of the scroll compressor with injection model, comparing the estimated data with the measured data from previous experimental study [99]. Estimated results show good agreement with the experimental data within 10% error.

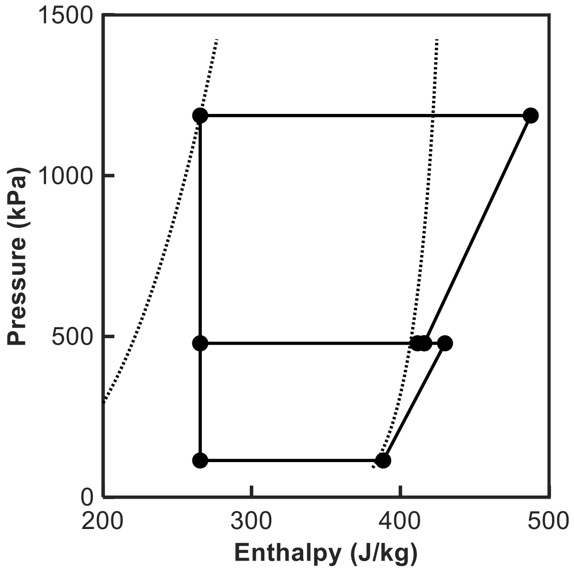

(a)

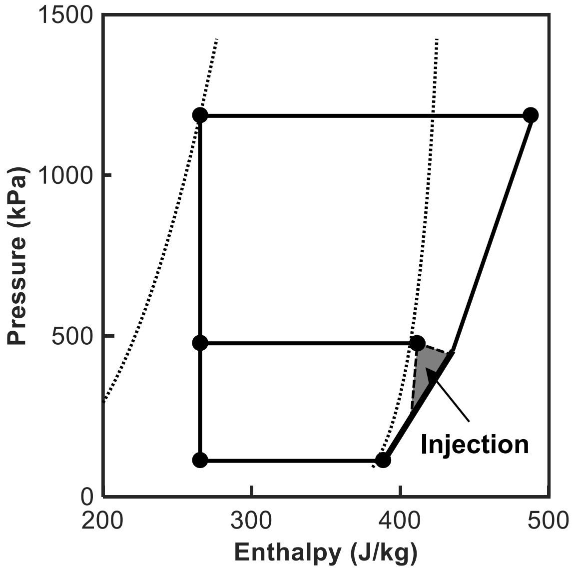

(b)

Figure 3.1 Two multi-level heat pump system on pressure-enthalpy diagram: (a) two-stage, (b) vapor-injection

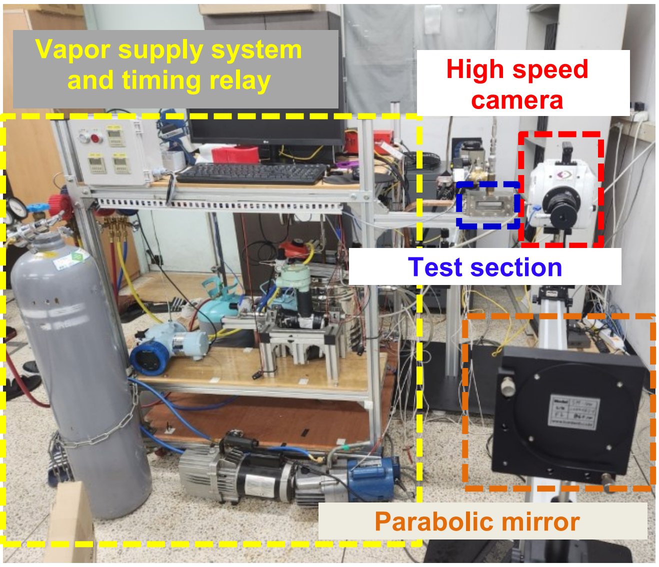

(a)

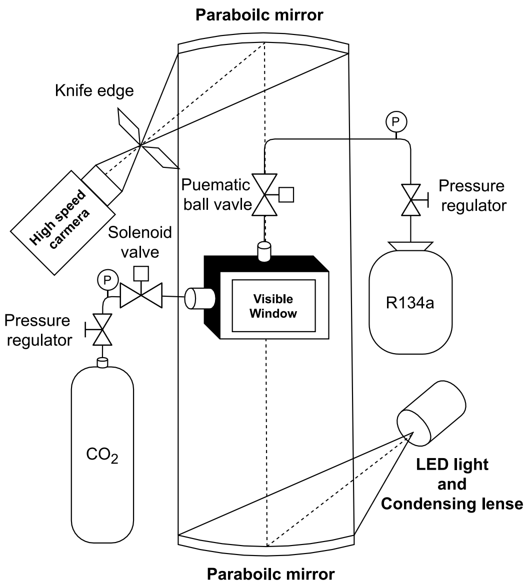

(b)

Figure 3.2 Schlieren experiment (a) apparatus and (b) schematic diagram.

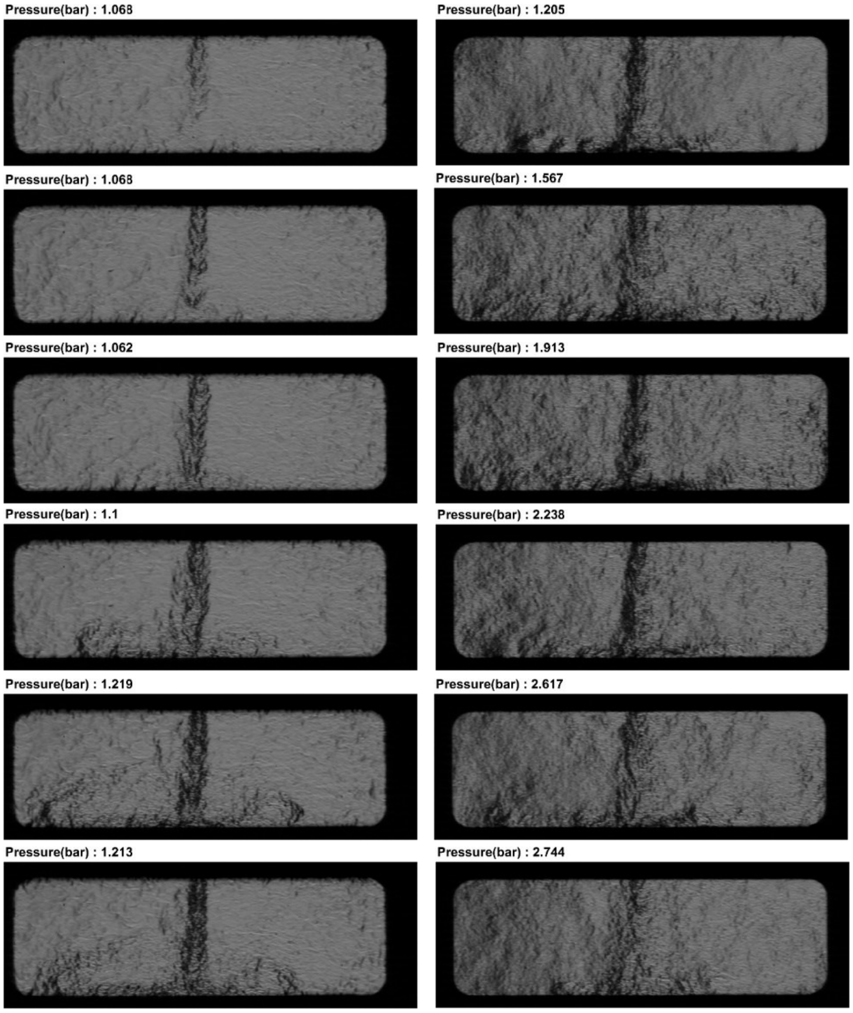

(a) (b)

Figure 3.3 Schlieren image of (a) initial injection process and (b) continuously decaying injection flow due to continuously increasing pressure in the chamber

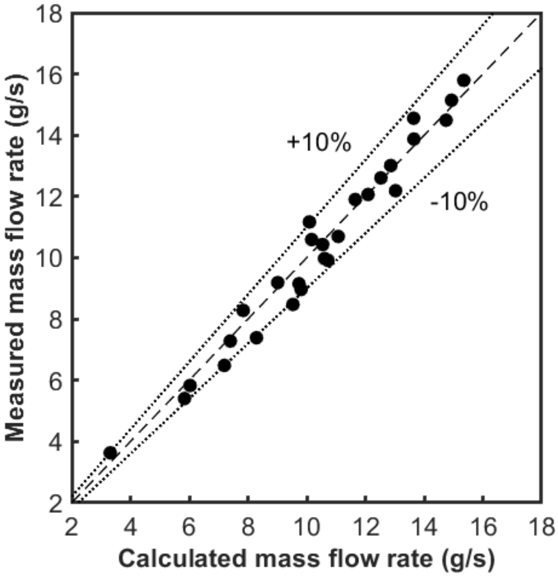

(a)

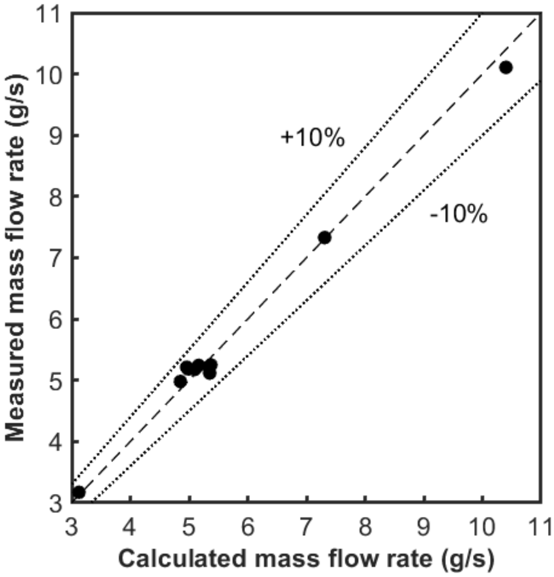

(b)

Figure 3.4 Validation results of scroll compressor with injection: (a) total mass flow rate and (b) injected mass flow rate

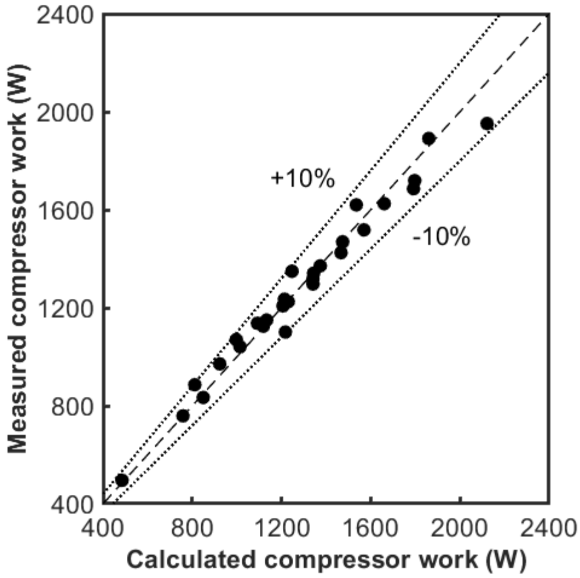

(a)

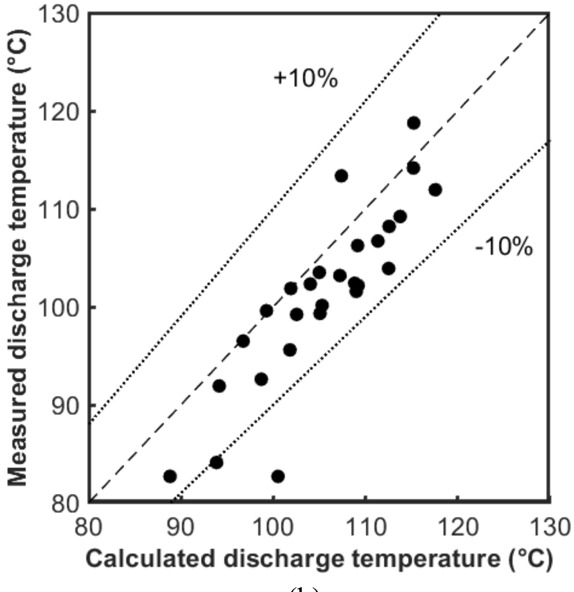

(b)

Figure 3.5 Validation results of scroll compressor with injection: (a) compressor work, and (b) discharge temperature

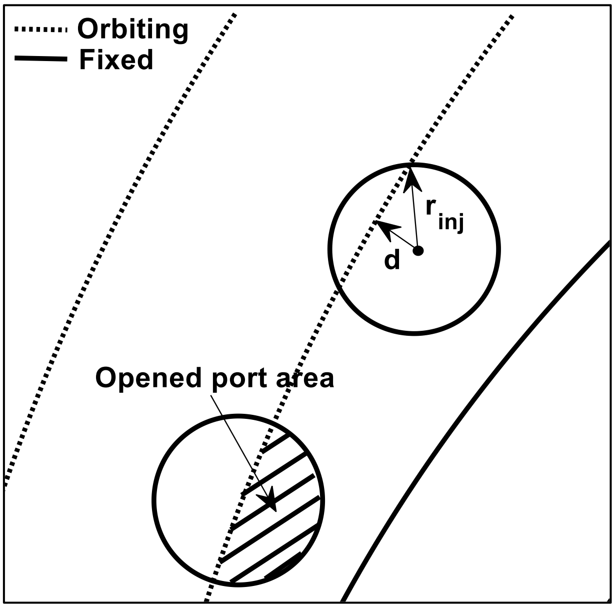

(a)

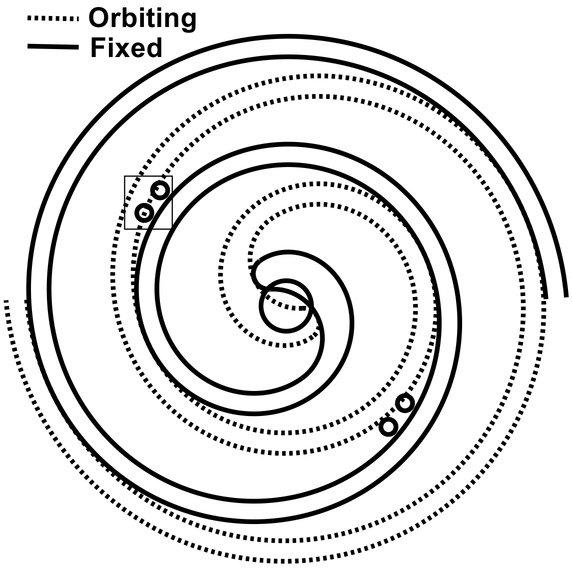

(b)

Figure 3.6 Scroll compressor with two injection holes in (a) enlarged size and (b) normal size

3.2.2. System modeling

Dynamic behavior of the heat pump system mainly originates from the dynamics of heat exchangers because temperature response is slower than the pressure response. Therefore, we focused on the thermal behavior of heat exchangers whereas compressor and expansion valves were assumed as to reach the steady-state in a short period. Quasi-steady compressor and expansion valves model determined the boundary conditions of heat exchangers; enthalpy and mass flow rate at the inlet and outlet. With given boundary conditions, the thermodynamic state of refrigerant in the heat exchanger at the next time step was derived through the secant method [125], which converges faster than the commonly used bisectional method.

$$\frac{\delta \rho}{\delta t} + \nabla \cdot (\rho \boldsymbol{u}) = 0 \qquad \text{Eq. (3.9)}$$

$$\frac{\delta (\rho \boldsymbol{u})}{\delta t} + \boldsymbol{u} \cdot \nabla(\rho \boldsymbol{u}) = \nabla \cdot \boldsymbol{\sigma} + \rho \boldsymbol{f} \qquad \text{Eq. (3.10)}$$

$$\frac{\delta (E)}{\delta t} + \nabla \cdot (E \boldsymbol{u}) = \rho \boldsymbol{f} \cdot \boldsymbol{u} + \nabla \cdot (\boldsymbol{\sigma} \cdot \boldsymbol{u}) - \nabla \cdot \boldsymbol{q} + \dot{Q} \qquad \text{Eq. (3.11)}$$

The transient heat exchanger model was based on the unsteady compressible two-phase flow model from MacArthur et al. [126]. Fundamental transport equations are shown in Eq. (3.9) - Eq. (3.11); mass, momentum, and energy equations.

In equation Eq. (3.9), continuity equation, the time derivative of density ρ equals to the divergence of density flux, which is product of density and velocity vector $\boldsymbol{u}$. Momentum equation is presented in equation Eq. (3.10), which includes stress vector $\boldsymbol{\sigma}$ and external force vector $\boldsymbol{f}$. The energy balance equation in equation Eq. (3.11) expresses the energy E of control volume with energy transfer by external force, viscous dissipation, conduction $\nabla \cdot \boldsymbol{q}$, and heat transfer rate $\dot{Q}$. Momentum equation was not considered in this model as the pressure wave propagates at the speed of sound, which is much faster than propagation speed of the others. Therefore, pressure was assumed as equal in any location as the pressure propagates at an instant without pressure drop. Then, the momentum and energy equations were derived into simpler form with proper assumptions. Considering the pipe or plate structure of heat exchanger, the governing equation was simplified into one-dimensional form. Viscous heat dissipation, spatial effect of pressure due to shear stress, and conduction effects were neglected, which correspond to the first three terms on the right-hand side of Eq. (3.11). Then, the mass flow was induced by the density change of control volume and the density of control volume is determined by heat transfer rate through wall and energy inflow and outflow. Heat exchangers were discretized into finite nodes, where the proper scheme is required to improve computational stability and accuracy. In this modeling, the upwind scheme and implicit Euler method [127] were applied to discretize the time and spatial change or gradient. The upwind scheme estimates surficial property as volumetric property at the node along with the direction of flow. This scheme compensates for the spatial bias caused by upstream during a unit time step. The implicit Euler method is unconditionally stable with large time step so that takes less computational time.

In Figure 3.7, spatial notation of the refrigerant properties in each node is presented, where the volumetric properties, enthalpy h, and density ρ, are at the middle of the node and surficial value, mass flow rate $\dot{m}$, is on the boundary of adjacent nodes. Heat transfer rate $\dot{Q}$ was calculated based on the h in the volume and locates at the bottom surface. The mass flow rate calculated from the last node was compared with the boundary condition derived from compressor or expansion valve to confirm the connections between components.

$$\frac{(\rho_i^{n+1} - \rho_i^n)V_i}{\Delta t} + \dot{m}_{j+1}^{n+1} - \dot{m}_j^{n+1} = 0 \qquad \text{Eq. (3.12)}$$

$$\dot{m}_{j+1}^{n+1} = \dot{m}_j^{n+1} - \frac{(\rho_i^{n+1} - \rho_i^n)V_i}{\Delta t} = 0 \qquad \text{Eq. (3.13)}$$

$$\frac{\{(\rho h)_i^{n+1} - (\rho h)_i^n\}V_i}{\Delta t} = (\dot{m}h)_j^n - (\dot{m}h)_{j+1}^{n+1} + UA_i(T_{i,cool}^{n+1} - T_i^{n+1}) \qquad \text{Eq. (3.14)}$$

$$h_i^{n+1}\left\{c_i + \frac{\rho_i^n V_i}{\Delta t}\right\} + UA_i T_i^{n+1}$$
$$= a_i h_{i-1}^{n+1} + b_i h_i^{n+1} + UA_i T_{i,cool}^{n+1} + h_i^n \frac{\rho_i^n V_i}{\Delta t} \qquad \text{Eq. (3.15)}$$

$$a_{i+1} = \max\left(\dot{m}_j^{n+1}, 0\right), b_i = \max\left(\dot{m}_j^{n+1}, 0\right), c_i = a_i + b_i + \frac{\rho_i^n V_i}{\Delta t}, \qquad \text{Eq. (3.16)}$$

Resultant continuity and energy balance equations were shown as Eq. (3.13) and Eq. (3.15). Subscripts i and j denote the properties at the volume and surface. Surficial property at j was substituted either i or $i+1$ depending on the flow direction with upwind scheme. Superscript n represents time step and properties or state at the next time step $n+1$ were used with implicit Euler method. Eq. (3.12) represents that the change of density with certain time step Δt in the node equals the difference between incoming and outgoing mass flow rates. This equation was rewritten as Eq. (3.13) to derive the mass flow rate from the previous node to next mode with incoming mass flow rate and density change. Eq. (3.14) means that the energy change in the node in a time step is expressed by incoming and outgoing energy rates and heat transfer rate, determined by the temperature difference of fluids. Convective heat transfer coefficient UA in Eq. (3.14) between two fluids, refrigerant and coolant (denoted as subscript $cool$), were calculated with appropriate correlations. Correlations [29–33] are tabularized in Table 3.1, which reflected the state of fluids (single phase, evaporating, and condensing), geometric specification (fin pitch, tube hydraulic diameter, etc.) and type of the heat exchanger (plate, fin-tube, louvered-fin tube). Eq. (3.14) was also rewritten into Eq. (3.14) by combining equation Eq. (3.14) and Eq. (3.12). Eq. (3.15) checked whether the energy balance with assumed pressure at the next time step is corrected or not. The assumed pressure at the next time step is updated with new value, calculated from secant method, until the difference between the right-hand side and left-hand side of the Eq. (3.15) converges within designated tolerance. Notably, the terms in energy balance equation should be ordered as Eq. (3.15) to ensure the convergence of iterative secant method. Coefficients a, b, and c were defined as Eq. (3.16) and introduced to conveniently express the substituted surficial values with upwind scheme.

Figure 3.8 shows the flowchart of ITMS model, including transient heat pump model and power electronics and electric motor (PEEM) model, in MWHR and CWHR modes. Secant method was used to iteratively find the pressure of condenser, evaporator, and WHX satisfying continuity and energy balance equation with given mass flow rate boundary conditions. Due to explicit nature of system connection, time step was confined as 1 s and boundary condition of mass flow rate was calculated at the present time step. Then, pressure of heat exchanger was assumed and the properties at nodes were calculated with inlet mass flow rate boundary condition. The outlet mass flow rate is compared with outlet boundary condition and assumed pressure value changes based on the results. However, this method accumulated refrigerant charge error, resulting in erroneous charge distribution in the system. Therefore, refrigerant charge was set as target variable instead of outlet mass flow rate and errors at the present time step were compensated at the next time step. Opening areas of expansion valves were controlled to maintain the DSH of evaporator and WHX both in experiment and system model. As PID gains used in experiment were not corresponded to the gains used in model so that detailed control logic was quantitatively different. However, validation results in Figure 3.9 shows a good agreement with experiment

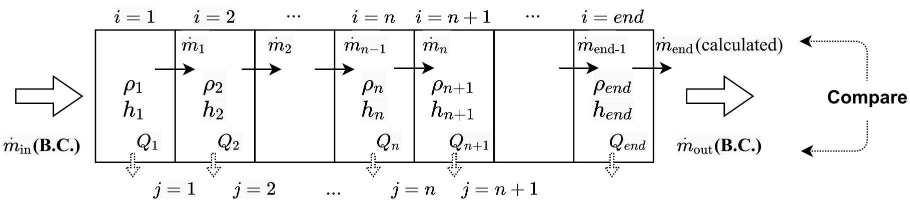

Figure 3.7 Refrigerant properties and its notation at each node in heat exchanger

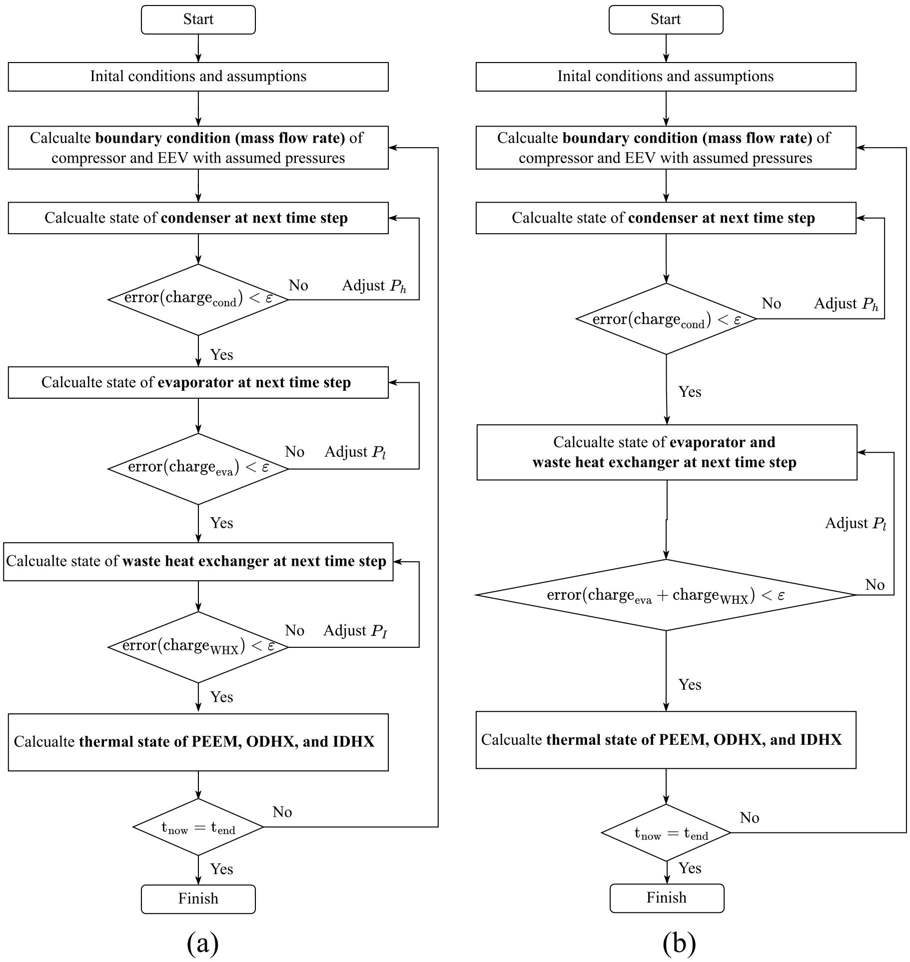

Figure 3.8 Flowchart of the simulation in (a) CHPTMS and (b) FLTMS

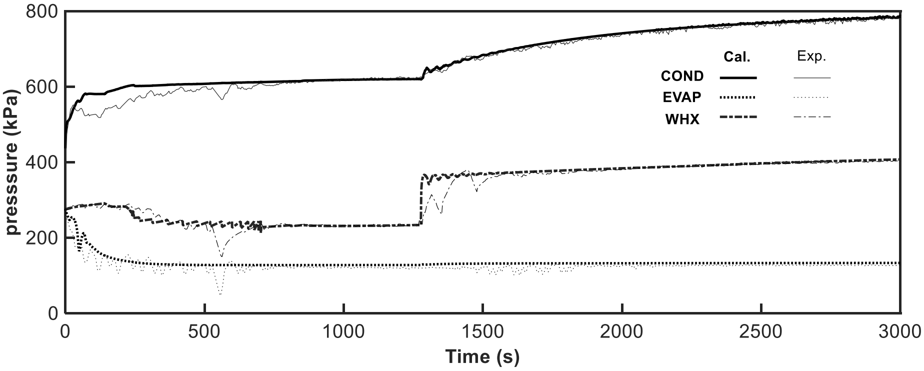

(a)

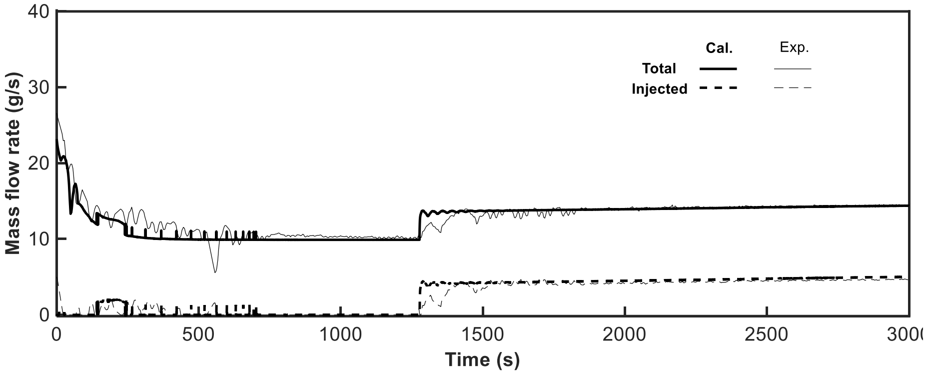

(b)

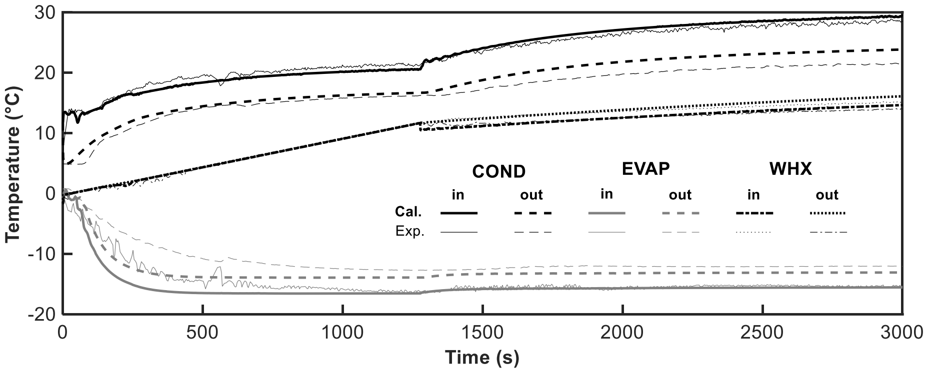

(c)

Figure 3.9 Dynamic behavior of heat pump experiment and model estimation of MWHR; (a) pressure, (b) mass flow rate, and (c) temperature

Table 3.1 Correlations and conditions used in heat transfer coefficient calculation

Reference	Correlation	Conditions
Yan and Lin [29]	$\mathrm{Nu} = 0.2121\mathrm{Re}^{0.78}\mathrm{Pr}^{1/3}$	Plate heat exchanger, single-phase
	$\mathrm{Nu} = 1.926\mathrm{Pr}_l^{\frac{1}{3}}\mathrm{Bo}^{0.3}\mathrm{Re}_{eqv}^{0.5}[(1-x)+x\left(\frac{\rho_l}{\rho_g}\right)]$	Plate heat exchanger, evaporating
Shah [30]	$h_t = h_l[(1-x)^{0.8} + \frac{3.8x^{0.76}(1-x)^{0.04}}{(P/P_{crit})^{0.38}}$	Plate heat exchanger, condensing
Chang and Wang [31]	$j = \mathrm{Re}^{-0.49}\left(\frac{\theta}{90}\right)^{0.27}\left(\frac{F_p}{L_p}\right)^{-0.14}\left(\frac{F_l}{L_p}\right)^{-0.29}\left(\frac{T_d}{L_p}\right)^{-0.23}\left(\frac{L_l}{L_p}\right)^{0.68}\left(\frac{T_p}{L_p}\right)^{-0.28}\left(\frac{\delta_f}{L_p}\right)^{-0.05}$	Louvred fin heat exchanger, air
Kays [32]	$j = \exp[-0.3488 \cdot ln(\mathrm{Re}/1000 - 4.283)]$	Fin tube heat exchanger, air
Gnielinski [33]	$\mathrm{Nu} = 0.0499 \cdot \mathrm{Re} \cdot \mathrm{Pr} \cdot \frac{d_h}{L} + 7.547$	Fin tube heat exchanger, coolant
	$\mathrm{Nu} = 0.012 \cdot (\mathrm{Re}^{0.87} - 280)\mathrm{Pr}^{0.4}[1 + \left(\frac{d_h}{L}\right)^{\frac{2}{3}}]$	Fin tube heat exchanger, coolant

3.2.3. Electric device modeling

Interior permanent magnet synchronous motor (IPMSM) is commonly used as a traction motor in EVs due to its high power density and efficiency. The thermal model of IMPSM was established to calculate the amount of heat generation and heat transferred to the waste heat recovery system, which are essential values determining the amount of recovered heat. The thermal model was mainly composed of heat generation model and thermal resistance model. Total heat generation of motor was estimated with sum of iron loss and copper loss, which were presented in Eq. (3.17) and Eq. (3.19).

$$Q_{coppper} = I_w^2 R_w \qquad \text{Eq. (3.17)}$$

$$R_w = R_0(1 + a_w T_w) \qquad \text{Eq. (3.18)}$$

$$Q_{iron} = k_h B_{max}^{\beta} \omega + k_e B_{max}^2 \omega^2 \qquad \text{Eq. (3.19)}$$

In Eq. (3.17), subscript w denotes the copper winding of IPMSM and heat generated by Joule loss of copper Q_{copper}, was calculated by the product of square of current I_w and resistance R_w, which is presented in Eq. (3.18) as reference resistance R_0, temperature T_w, and thermal coefficient of resistance a_w. As presented in Eq. (3.19), heat generated in iron Q_{iron} was mainly caused by hysteresis of magnetization in iron and eddy current. Hysteresis loss is presented with hysteresis coefficient k_h, maximum magnetic flux density

B_{max}^{β}, and rotational speed of motor ω. Eddy current loss is expressed with eddy current coefficient k_e, maximum magnetic flux, and speed of motor. This model was based on the electric motor thermal model of Kim et al. [131] and coefficients and magnetic flux were also presented in the literature. Heat generated in the electric motor transferred through thermal resistance of rotor, airgap between rotor and stator, coil, stator, and cooling jacket. Thermal resistance was calculated on cylindrical coordinate and discretized into 8 nodes, shown as a schematic of thermal resistance circuit in Figure 3.10 (b).

Power electronics (PE) were simply assumed to generate heat proportional to the total power consumption of the electric motor and heat was assumed to be totally transferred instantenously to the coolant, considering the small size of PE. The model was validated with vehicle experiments and estimated the coil temperature with reasonable accuracy, as presented in the previous study [59]

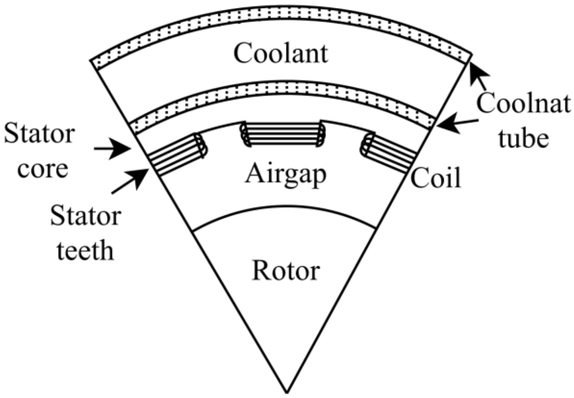

(a)

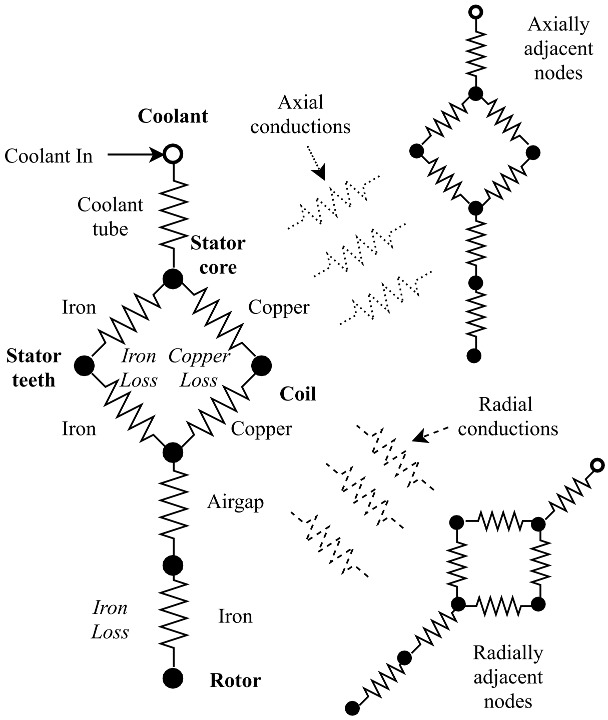

(b)

Figure 3.10 Schematic of motor model; (a) thermal components and structure of electric motor and (b) thermal resistance circuit of motor.

3.3. Results and discussion

Results were thoroughly investigated with various driving profile and ambient air temperature. In addition to MWHR and CWHR modes, direct waste heat recovery (DWHR) mode was considered as a WHRS, which directly provided hot coolant, absorbing waste heat from PEEM, to the cabin through indoor heat exchanger (IDHX). An auxiliary PTCH was used to provide additional heat to the cabin to equalize the heating capacity of CWHR, MWHR, and DWHR mode as 5 kW. Cabin air, calculated by lumped cabin thermal model [108], was recirculated and passed through the IDHX. As a reference, driving profile with constant velocity were tested first to clearly verify the effect of driving duration, vehicle velocity, and ambient air temperature.

Figures 8 and 9 show transient behavior of system performance in CWHR, MWHR, and DWHR mode when the velocity of the vehicle was 100 km/h and the ambient temperature of the air was 0 °C. While CWHR simultaneously recovered waste heat with heat pump operation, MWHR and DWHR needed a time delay to WHR until the temperature of coolant reached a certain level. DWHR initiated WHR when the coolant temperate from PEEM exceeded the coolant temperature of IDHX by 5 °C. Then, two coolant streams from PEEM and IDHX were merged and entered the IDHX; the merged stream was separated into two streams at the exit of IDHX, flowing to the WHX and condenser, respectively. This flow merge increased the total flow rate in IDHX, augmenting the heating capacity of the system. MWHR initiated as heat pump operates, but the EEV at the inlet of WHX was not opened until the residual liquid refrigerant in WHX evaporated. After refrigerant in WHX became superheated state, refrigerant flowed to WHX to prevent liquid injection into compressor. Figure 3.11 (a) presents transient pressure from start-up conditions in CWHR, MWHR and DWHR modes. The condensing pressures in each mode increased with time as the temperature of heat sink, air in the cabin, increased with cabin air recirculation. The evaporating pressures were relatively constant with constant temperature of heat source, ambient air. At the early stage, the condensing pressure of CWHR was higher than the other two modes because larger amount of heat was absorbed from the PEEM. However, as the MWHR recovered waste heat (from 259 s), condensing pressure rose more rapidly than that of CWHR. The condensing pressure of MWHR firstly increased and then decreased before PEEM heat recovery. The pressure drops after early stage occurred because of forced injection derived by the heat absorption in WHX. The evaporated refrigerant in WHX was injected to the compressor when the pressure in WHX exceeded the pressure of compression chamber. The pressure of compression was determined by evaporating pressure, which decreased until the mass inflow from condenser and mass outflow to compressor were equalized. After forced injection, EEV at the inlet of WHX opened to absorb heat from PEEM, increasing the pressure of WHX.

Figure 3.11 (b) demonstrates that even though the amount of absorbed heat from PEEM in MWHR was smaller than in CWHR, MWHR utilized the ambient air source more effectively than CWHR. The heating capacity of MWHR was larger than that of CWHR after 601 s, where the superiority of MWHR exists. The main disadvantage of CWHR originates from the biased flow distribution to the dual heat sources: ambient air and PEEM. As the certain amount of mass flow from compressor separated into two streams, more refrigerant flowed to the heat source dissipating larger amount of heat. Therefore, CWHR was unable to utilize the ambient air source as much as single-source with flow distribution problem, which did not occur in the MWHR as the refrigerant injection was induced by external pressure difference. This phenomenon is shown in Figure 3.12 (a), presenting total and injected mass flow rate in each mode. As the absorbed heat from PEEM increased, the total mass flow rate increase of CWHR was relatively small even with increasing refrigerant flow from WHX, while the total mass flow rate of MWHR continuously increased by the injected mass flow rate of WHX.

The behavior of DWHR was relatively simple as the waste heat recovery and heat pump system operated in separated loop except for the IDHX. As the temperature of coolant from PEEM exceeds the temperature of coolant from IDHX, coolant from condenser and PEEM merged and passed the IDHX, providing more heat to the cabin as shown in Figure 3.11 (b). The condensing pressure of DWHR in Figure 3.11 (a) increased as warmer coolant inflowed into condenser; the temperature difference of inlet and outlet coolant of IDHX decreased with more coolant flow rate through IDHX. However, heat pump operated consistently because of separated PEEM heat recovery.

The temperatures of coolant in the PEEM heat recovery system were presented in Figure 3.12 (b), showing the temperature level of WHR of each mode. The temperature level of PEEM in MWHR resided at the intermediate level between CWHR and DWHR, which recovered heat at the evaporating and condensing temperature, respectively. The overall temperature of the coolant increases as the heat radiated to the coolant were less than the heat generated in PEEM with limited performance of the cooling jacket.

Figure 3.13 presents the resultant power consumption of CWHR, MWHR, and DWHR. CWHR required less PTCH power consumption owing to the higher heating capacity at the early stage; when the waste heat was not available in MWHR and DWHR until the temperature of PEEM reached the appropriate level. After the MWHR initiated the injection, the instantaneous power consumption of compressor increased with an additional mass flow through compressor, while less power of PTCH was required with larger heating capacity. Total power consumption of CWHR exceeded that of MWHR (611 s), as the PTCH power consumption of MWHR decreased. The higher heating capacity of MWHR required less PTCH usage than that of CWHR, which originated from the superior waste heat recovery of MWHR, as mentioned above. Even though the compressor in MWHR consumed more power with a larger mass flow than CWHR, the total power consumption of MWHR was saved with less power demand from PTCH, having a COP of 1.

The superior heating performance of MWHR eventually brought a cross of total power consumption in the entire driving. The accumulated power of CWHR surpassed that of MWHR at 1275 s, when 664 s had elapsed after the instantaneous power consumption trend of MWHR and CWHR was reversed. This represents a time to compensate initial unavailability of waste heat in MWHR by superiority in waste heat recovery. Power consumption of the compressor in each mode increased with the higher condensing pressure and mass flow rate indicated in Figure 3.11 (a) and Figure 3.12 (a), respectively. DWHR initiated heat recovery at 946 s, which needed more time delay to warm up the coolant through PEEM. After heat recovery in DWHR, instantaneous power consumption of DWHR became smaller than that of CWHR with augmented heating capacity, and then the accumulated power consumption was reversed at 2501 s. In addition, the instantaneous power consumption of DWHR crossed that of MWHR because less power was consumed at the compressor, which implied that the accumulated power consumption of MWHR would exceed that of DWHR and the optimal WHRS change.

To further investigate the performance of WHRSs, we analyzed WHRSs with different ambient air temperature and velocity of vehicle. Figure 3.14 shows transient behavior of WHRSs when the vehicle velocity were 50 km/h and 100 km/h. As the vehicle drove at slower pace, the amount of absorbed waste heat decreased. This affects the time to initiate the DWHR, which was determined by the temperature rise of PEEM by the heat generation; and the time to initiate heat recovery in DWHR was postponed from 947 s to 2190 s with a smaller amount of waste heat, as shown in Figure 3.14 (b).

In MWHR, the target DSH at the outlet of WHX was set as 5 K so that the mass flow rates through WHX were determined by the amount of waste heat. As shown in Figure 3.14 (a), the total mass flow rate increased with faster vehicle velocity, which directly augmented the heating capacity of heat pump system. Resultant power consumptions are presented in Figure 3.14 (c), demonstrating that the cross points, where MWHR became more advantageous than CWHR, were withheld with less vehicle speed owing to the smaller amount of waste heat. This was because the biased flow problem in CWHR deteriorated with a large amount of waste heat, as the imbalance between the waste heat and absorbed heat from ambient was worse. Those effects were more prominent on DWHR as the waste heat affected the time to initiate heat recovery in DWHR as well as the amount of waste heat itself. Figure 3.14 (c) indicates that the accumulated power consumption of DWHR with a vehicle speed of 50 km/h was larger than that of CWHR within 3000 s, whereas the power consumption of CWHR with 100 km/s speed condition exceeded that of DWHR at 2501 s.

Ambient air temperature mainly affects the evaporating pressure, where heat from ambient air is absorbed. As the lower evaporating pressure accompanies lower suction density and mass flow rate of a compressor, heat pump performance deteriorates at low ambient temperature. Figure 3.15 shows the transient power consumptions of CWHR, MWHR, and DWHR at different ambient air temperatures. Power consumption was increased at lower ambient temperatures because of poor heat pump performance. However, a notable result was that the performance enhancements between different WHRSs at lower ambient temperatures were more apparent, especially in DWHR. The cross points between MWHR or DWHR and CWHR were advanced (from 1364 s to 1255 s and 2522 s to 2028 s) with lower ambient temperature, which originated from relatively low quality of ambient air-source. CWHR utilized the waste heat from PEEM at ambient temperature whereas MWHR and DWHR recovered the waste heat at higher temperature levels. As the heat pump operated at a lower performance region, enhancement with efficient utilization of the waste heat was more necessitated. DWHR outperformed MWHR at 2781 s when the outdoor air temperature was -10 °C, which did not even appear at 0 °C ambient air temperature.

The results above demonstrate that the advantage of utilizing waste heat with optimal WHRS is more prominent, especially at cold ambient temperatures and with fast driving speed, which is the main region where the EV range extension is necessitated.

The ITMS model can suggest an optimal WHRS with given driving conditions, including driving profile and ambient air temperature. Under the given driving profile and ambient air temperature, the ITMS model predicts the performances of each WHRSs and derives optimal WHRS. Standardized driving profiles are classified as highway profiles, including HWFET, WLTP3, and ArtMw150, and urban driving profiles, including FTP75, NEDC, and ArtRR and each profile was cycled twice to clearly show the transition trend of optimal WHRS. Driving profiles mainly affected the optimal WHRS with driving time and averaged velocity, which is summarized in Table 3.2.

Table 3.3 shows the optimal WHRSs and power savings with different ambient temperature condition and driving profiles. Driving profiles with longer duration, such as WLTP3 and FTP75, had sufficient time to compensate the energy consumption of MWHR and DWHR without WHR in the delayed time. Driving profiles with higher averaged driving speed, such as ArtMw150, provided larger amount of waste heat to the cabin, obtaining DWHR as an optimal WHRS. Results demonstrate that the energy consumption can be saved up to 13% with the predictive WHRS optimization method compared with CWHR.

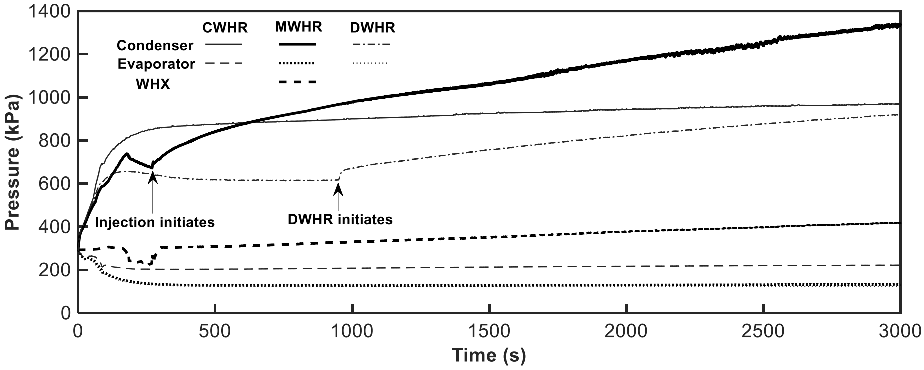

(a)

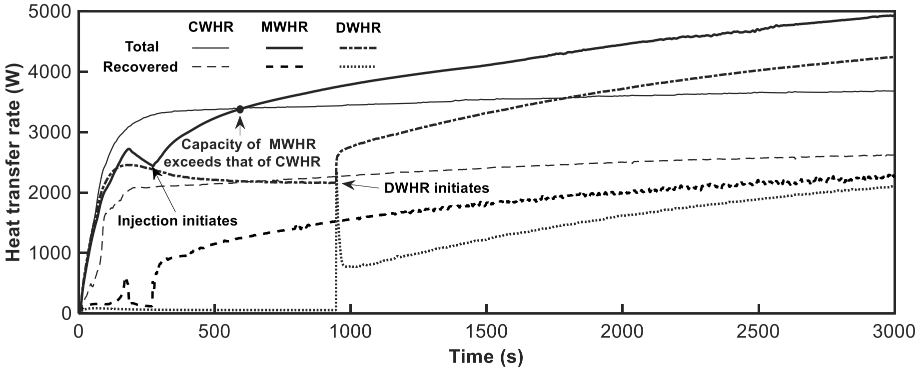

(b)

Figure 3.11 Transient behavior of heat pump system in CWHR, MWHR, and DWHR mode; (a) pressure, (b) heat transfer rate. Heat pump operated with constant vehicle speed of 100 km/h, ambient temperature of 0 °C, and 100% recirculation of cabin air. (evaporating pressure of DWHR and MWHR are overlapped.)

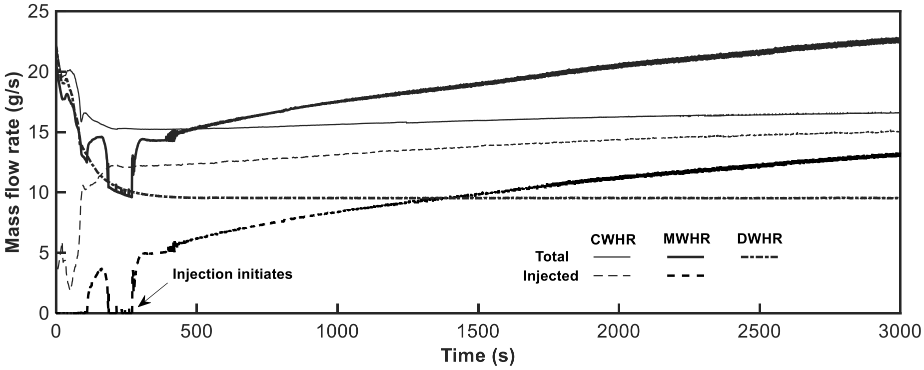

(a)

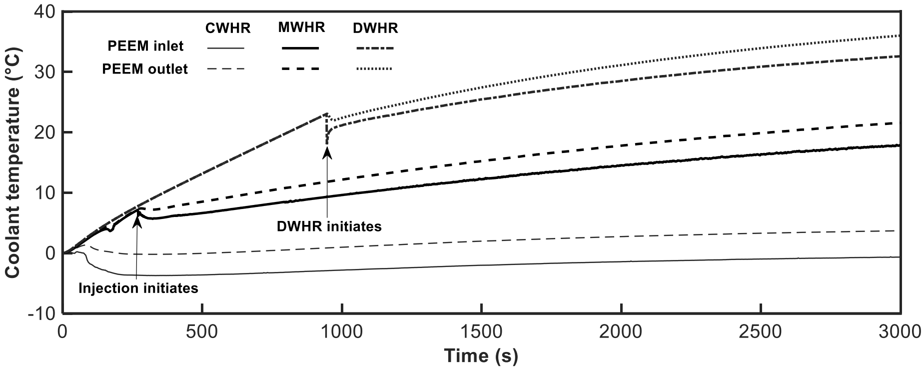

(b)

Figure 3.12 Transient behavior of heat pump system in CWHR, MWHR, and DWHR mode; (a) mass flow rate, and (b) PEEM coolant temperature. Heat pump operated with constant vehicle speed of 100 km/h, ambient temperature of 0 °C, and 100% recirculation of cabin air

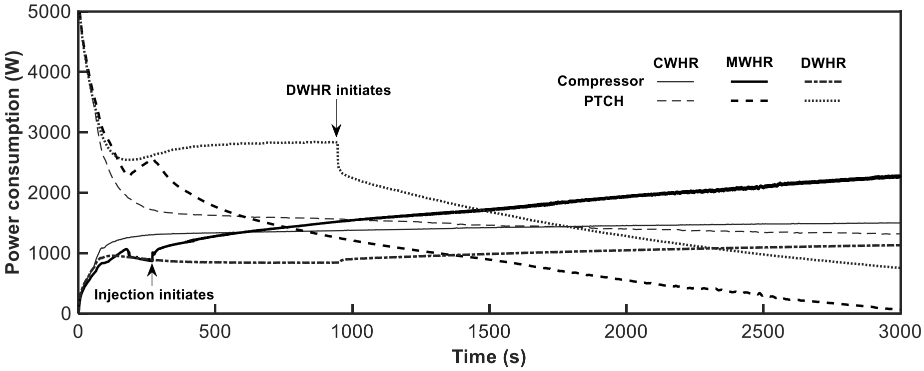

(a)

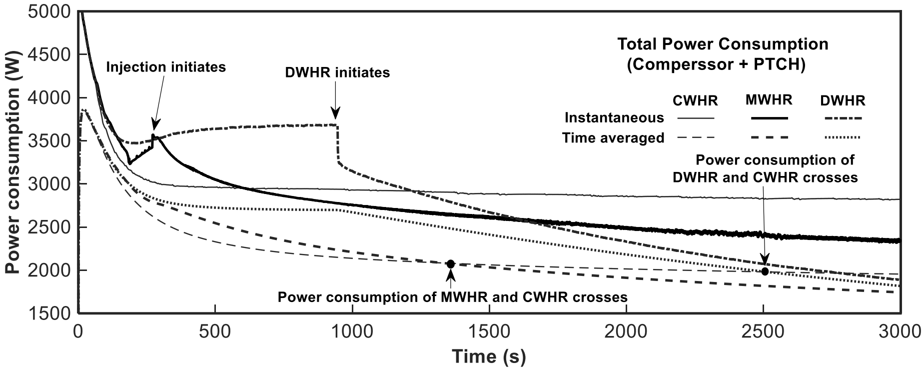

(b)

Figure 3.13 Power consumption by (a) components and (b) total power consumption of heat pump system at instantaneous and time averaged domain in CWHR, MWHR, and DWHR mode.

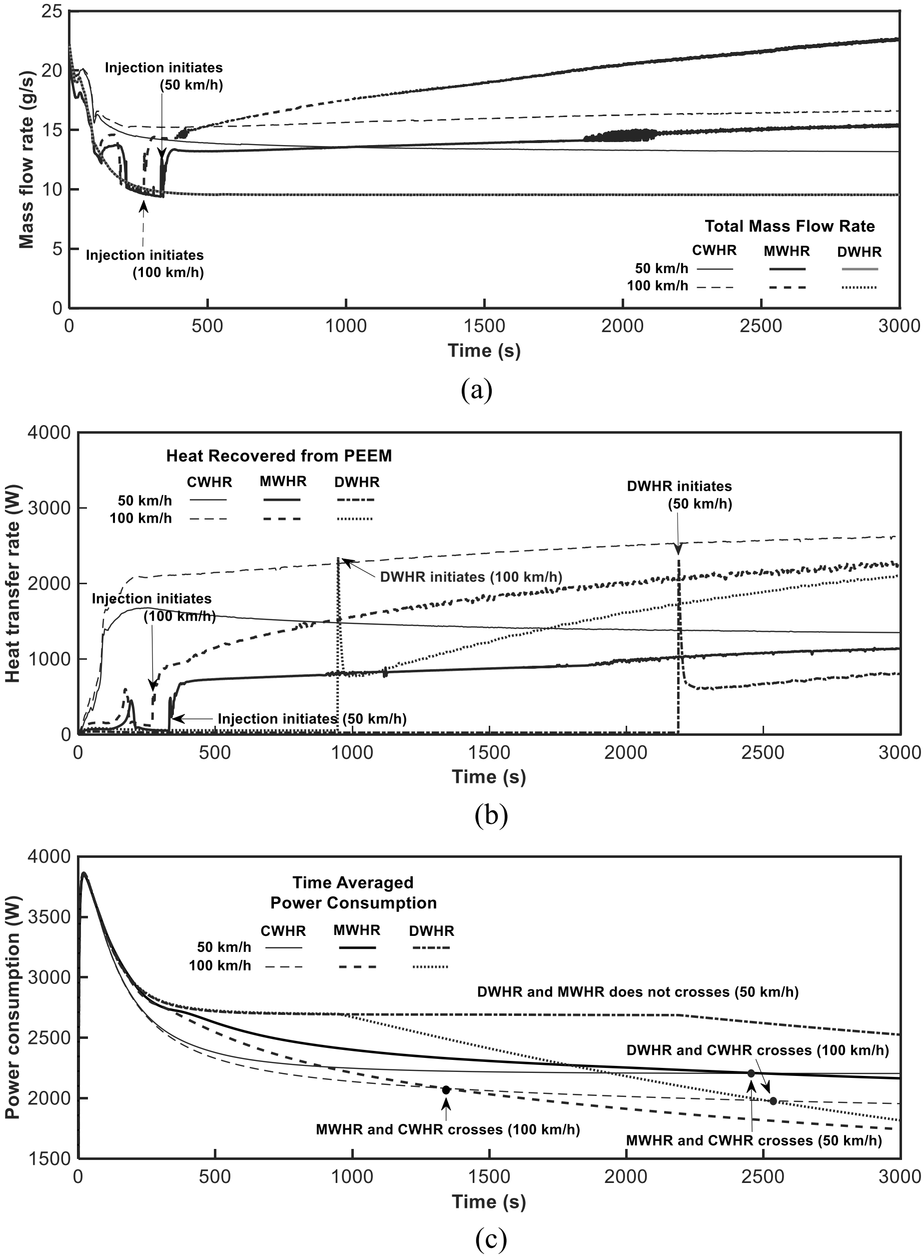

Figure 3.14 Transient behavior of heat pump system with different vehicle speed; (a) total mass flow rate (b) recovered heat from PEEM (c) time averaged power consumption.

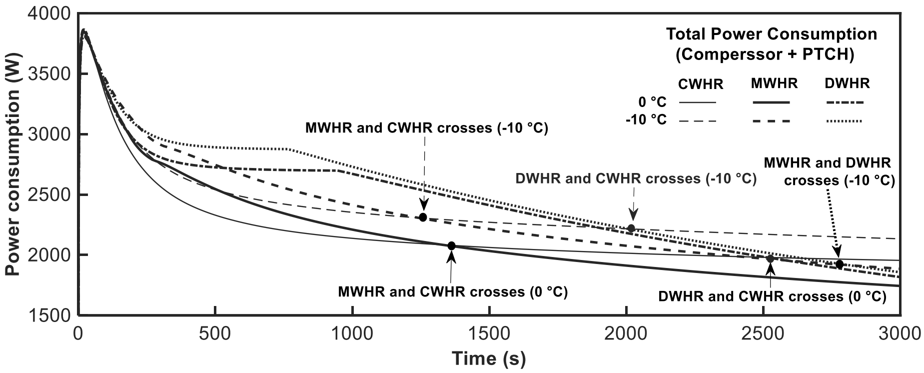

Figure 3.15 Transient behavior of total power consumptions at different ambient air temperatures in each mode.

Table 3.2 Averaged speed and duration of standardized driving profiles

Profile	Averaged Speed (m/s)	Duration (s)	Remarks
ArtMw150	27.63	1068	Driving cycle from Artemis project. Highway driving with 150 km/h speed limit.
HWFET	21.55	765	The Highway Fuel Economy Driving Schedule. Highway driving under 100 km/h.
WLTP3	12.92	1800	The Worldwide Harmonized Light Vehicle Test Procedure (WLTP) Class 3.
ArtRR	15.96	1082	Driving cycle from Artemis project. Driving on rural road.
FTP75	7.18	2474	The Federal Test Procedure (FTP)
NEDC	9.33	1180	New European Driving Cycle

Table 3.3 Optimal WHRSs and power savings of different driving profiles and ambient temperatures

CWHR	MWHR	DWHR

Temp / Profile	-0 °C	-5 °C	-10 °C	-15 °C	-20 °C
ArtMw150	6.5%	7.7%	7.0%	7.9%	13.0%
HWFET					0.4%
WLTP3	2.5%	2.8%	3.0%	3.4%	3.6%
ArtRR		0.3%	0.8%	1.3%	1.2%
FTP75	2.7%	2.5%	2.5%	2.4%	2.3%
NEDC					

3.4. Summary

In this chapter, we investigated the performance of WHRSs and suggested the optimal WHRS under various start-up conditions with the ITMS model. Conventional WHRS recovers waste heat from electric devices at one temperature level. We subdivide the temperature level into three using the vapor injection technique, which enables delicate utilization of the waste heat. A transient heat pump and PEEM thermal model were established based on experimental data, and the ITMS model estimated the heating performance of each WHRS. Compared with CWHR, MWHR and DWHR had larger heating capacity augmented through WHR at higher temperature levels and resultant power consumptions were saved with less PTCH usage. However, MWHR and DWHR required time delay to compensate for the unavailability of waste heat at the early stage. The time delays were 1275 s in MWHR and 2501 s in DWHR when the ambient temperature was 0 °C and vehicle speed was 100 km/h. Those time delays were reduced with lower ambient temperature and increased with slower vehicle speed. Results with standardized driving profiles demonstrated that MWHR and DWHR were advantageous under driving profiles with a large amount of waste heat and long driving duration, such as WLTP3 or ArtMw150 profile. Power consumptions were saved up to 3.6% and 13.0 % with MWHR and DWHR, respectively. However, CWHR consumed the least power in urban driving conditions, NEDC, with slow vehicle speed and short duration. The optimal WHRS, suggested by the ITMS model in advance of driving, utilizes the waste heat most efficiently, contributing to the driving range extension of EVs under various driving conditions.

Chapter 4. Port design optimization of multi-level waste heat recovery system[4]

4.1. Introduction

Previous studies on MWHR focused on the overall system performance and power savings with existing injection port design. As the MWHR uses vapor injection technique, the port hole design affects both heat pump system and thermal management system (TMS). Therefore, investigation on the effect of port geometry is necessary to design vapor injection compressor with MWHR.

In this chapter, I investigated the effect of port design in the perspective of integrated thermal management system (ITMS), including heat pump system and TMS. A flow visualization experiments were conducted to inspect the complicated phenomena, including macroscopic jet impingement behavior. Existing injection models simply assumed the injection process as steady isentropic nozzle [123, 132, 133] or used empirical fitting coefficients [134, 135]. To the best of our knowledge, none of injection models have considered

[4] The contents of chapter 4 were published as in *Applied Thermal Engineering* [145] on 2023

the jet impingement effect to determine the thermodynamic state of mixed refrigerants. Therefore, we established a novel injection model based on the heat transfer characteristic of jet impingement and dynamically increasing pressure of the chamber during compression process. This model was combined with a transient heat pump model and power electronics and electric motor (PEEM) model, incorporating an ITMS model. We investigated the effect of port hole size and location on the MWHR system with the ITMS model. Furthermore, the optimal port design was suggested to save total power consumption.

4.2. Results and discussion

I investigated the effect of port design on the MWHR performance under cold-start condition. The simulation conditions are summarized in the Table 4.1, including ambient temperature, vehicle speed, port angle and size. The port hole radius was varied from 1 mm to 2 mm, which is maximum radius to be entirely closed by the orbiting scroll. The effect of larger port size was analyzed by adding a secondary port, denoted as dual-port. As shown in Figure 4.1, the port location was set from 360 ° to 780 °, including the angle where the port opens before suction chamber closed, and the angle which is closed after discharge port opens. The initial temperature of each component was assumed to be soaked at the ambient air temperature. As a preliminary investigation, three different waste heat recovery systems in Figure 4.2 were compared. CWHR recovers the waste heat from PEEM through WHX, which has equal pressure with the evaporator due to pipe connection before entering into the compressor. On the other hand, DWHR directly recovers the waste heat by flowing hot coolant from PEEM to the indoor heat exchanger (IDHX). It requires a time delay for coolant from PEEM to reach the temperature of coolant from the condenser. Lastly, MWHR recovers heat from PEEM with WHX having an intermediate pressure to inject the refrigerant into the compressor.

The main difference between WHRs lies in the temperature level where the waste heat is recovered. As the heat is recovered at higher temperature, refrigerant or coolant with higher energy transfers heat to the cabin, and less power is required to raise the temperature of fluid to reach appropriately high temperature to be provided to the cabin. However, an additional heat is needed to elevate the temperature level of the heat source having certain heat capacity. Therefore, a trade-off between the heating capacity augmentation and heat required to raise the temperature level should be analyzed on the time domain.

Figure 4.3 shows the performance of each waste heat recovery system with the perspective of power consumption and heat. The accumulated power consumption in Figure 4.3 (a) demonstrates that CWHR system consumed the least power compared with other two systems until one hour; but the discrepancy of time-averaged power consumption between CWHR with DWHR and MWHR decreased with time. The instantaneous power consumption of DWHR and MWHR became lower than that of CHWR. This originated from the decreasing trends of consumed power of PTCH after injection and DWHR, as indicated in the Figure 4.3 (b). Even though the compressor required more power with increasing pressure ratio in DWHR and mass flow rate in MWHR, total power consumption decreased with both DWHR and MWHR.

In addition, MWHR and DWHR outperformed CWHR in terms of the heat transfer to the cabin even with less heat absorption from the PEEM, as shown in Figure 4.3 (c). This is because CWHR shared a finite mass flow rate of compressor suction line by evaporator and WHX. As to a larger amount of waste heat to be absorbed with WHX, more mass flow rate of refrigerant through WHX should flow through the WHX, resulting in the decreased heat absorption from the ambient air with the evaporator. Nevertheless, the advantageous aspects of MWHR and DWHR with existing port design could not compensate the initial heat requirement to elevate the temperature level in an hour. The existing port was originally designed to be used in a vapor injection system with a flash tank or internal heat exchanger; and MWHR has entirely different thermal behavior with conventional vapor injection system. Therefore, the injection port should be redesigned to optimize the system performance with MWHR.

To optimize the MWHR heat pump system, the system performance was investigated with various port geometries, as presented in Table 4.1. Figure 4.4 presents the time-averaged power consumption of CWHR, DWHR, and MWHR with different ports, showing that the larger injection port and angle requiring less power consumption. Figure 4.4 (b) only shows a region where the power consumption decreased with the port angle to graphically show the tendency in a clear way. The time when the time-averaged power of MWHR becomes less than that of CWHR is called the ‘cross point’, which is a key indicator. It represents the time required to compensate for the initial stage of MWHR, when the waste heat is used to elevate the temperature level of PEEM instead of absorbed in the heat pump system. When a EV drives for a duration longer than the time at the cross point, operating the heat pump system with MWHR is advantageous and vice versa. Therefore, early time at the cross point means that the heat pump operation with MWHR is beneficial in broader region.

The port size mainly affected the injected mass flow rate and resulting heat absorption from PEEM, as presented in Figure 4.5 (a) and (b). As the port enlarged or became dual, more refrigerant flowed through the injection hole with equal pressure difference between WHX and compression chamber. The electronic expansion valve (EEV) controlled the degree of superheat (DSH) of refrigerant at the outlet of WHX to prevent wet-compression. Therefore, the specific enthalpy difference between inlet and outlet refrigerant of WHX was constant, so that the increasing mass flow rate through WHX accompanied more heat absorption from the PEEM.

On the other hand, the port angle mainly determined the pressure of compression chamber during injection. The injection initiated with the opening of injection port and completed with the closing of injection port. As shown in the Figure 4.5 (c), the pressure level of WHX increases when the injection port was located at small angle because the port opened after relatively longer compression. The higher pressure of WHX caused larger pressure difference and injected mass flow rate. However, Figure 4.5 (d) demonstrates that the temperature level of PEEM increased with higher pressure level of WHX as the heat absorption temperature equaled to the saturation temperature at the pressure of WHX. This temperature level elevation delayed the cross point in two aspects: increased amount of heat required to rise the temperature level of PEEM and postponed time at the initiation of injection, which awaited PEEM to reach the temperature level. The injection timing is not clearly shown Figure 4.5 because of overlapped data except for Figure 4.5 (d).

The results were reorganized in Figure 4.6, presenting power consumptions and corresponding cross point changes with dominant system indicators, after driving for an hour. As mentioned above, a large area of injection port decreases power consumption and time at the cross point with larger amount of injected refrigerant, as shown in Figure 4.6 (a) and (b). On the other hand, the optimal port angle existed as 600 ° and 660 ° with the perspective of power consumption and cross point, respectively. The existence of the optimal angle originated from that the injection port hole at large angle opened during the suction process. The injection increased the pressure of suction chamber, refrigerant suction from the evaporator was interrupted by injection flow. The sudden decrease in suction mass flow rate is shown in Figure 4.6 (d), implying insufficient heat absorption from the ambient air. This negative impact of large port angle was combined with the positive impact of decrease in the injection pressure or temperature level of waste heat absorption, forming a convex shape and the optimal port angle.

Lastly, the amount of waste heat was varied by adjusting the vehicle velocity. In the previous discussion, DWHR was not mentioned as the parameters above did not affect the performance of DWHR. However, the amount of waste heat determined the time of DWHR initiation when the temperature of coolant form PEEM exceeded that from the condenser. Figure 4.7 (a) shows the delay in the initiation of DWHR with slower vehicle speed of 50 km/h. Considering that the power consumption of MWHR and DWHR nearly crossed at 3600 s with the vehicle speed of 100 km/h, the driving conditions where DWHR requires the least power exists. However, DWHR required excessive time to compensate unavailability of the waste heat in early stage in the analysis in this study.

The cross points of MWHR were delayed not as much as the initiation time of DWHR with slow vehicle speed. This was because CWHR recovered less amount of waste heat as well as the MWHR did. Figure 4.7 (b) shows that the time at the cross point decreased with faster vehicle speed, representing that the MWHR is desirable when faster and longer driving, which is one of the common circumstances where the passengers experiences the range anxiety. Therefore, I expect that the heat pump operation with optimized MWHR can contribute to alleviating the range anxiety

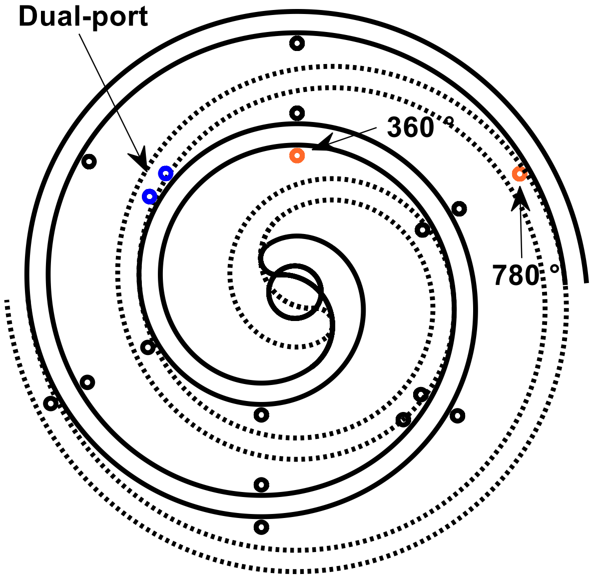

Figure 4.1 Scroll wrap with injection ports with (port angle from 360° to 780°)

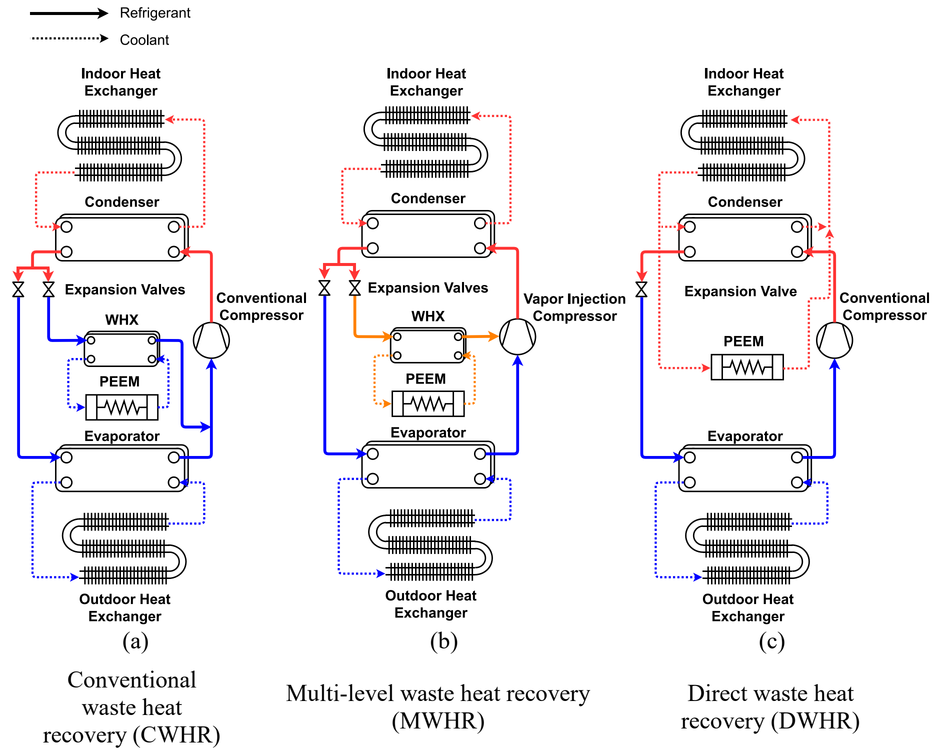

Figure 4.2 Schematic of different waste heat recovery systems

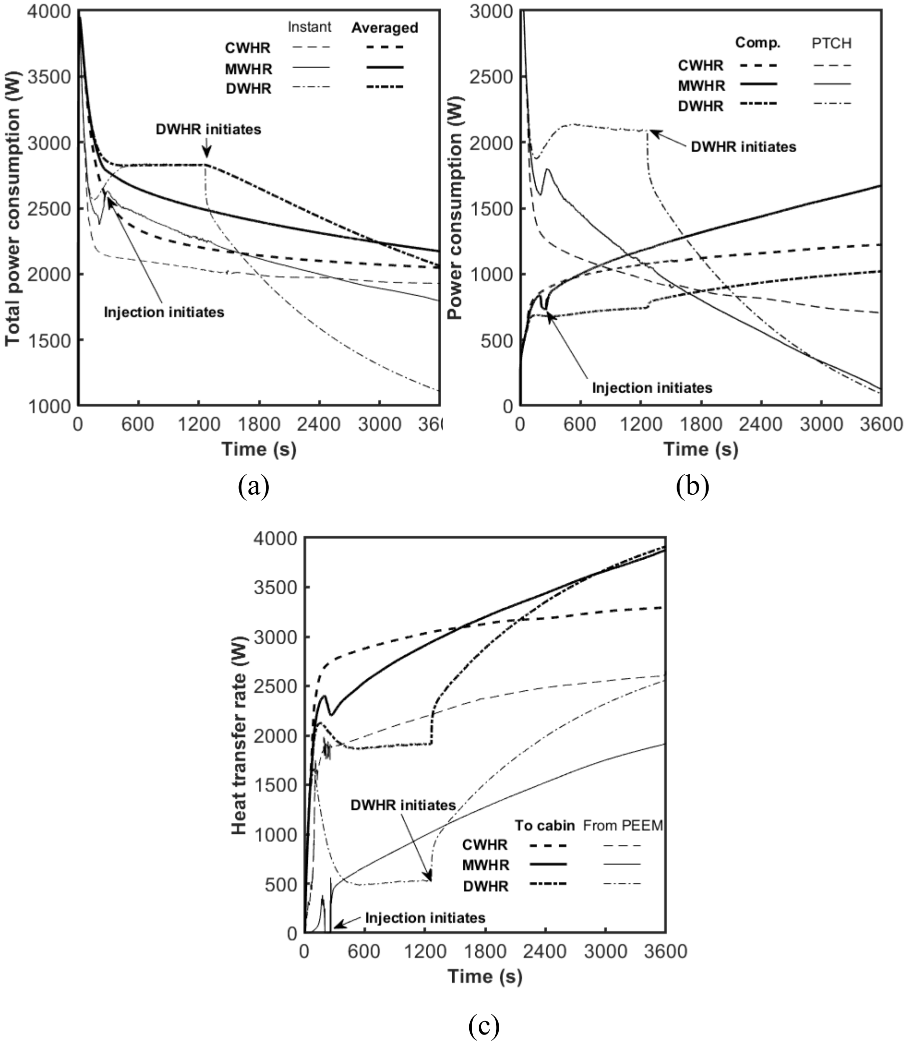

Figure 4.3 Scroll wrap with injection ports with (port angle from 360° to 780°)

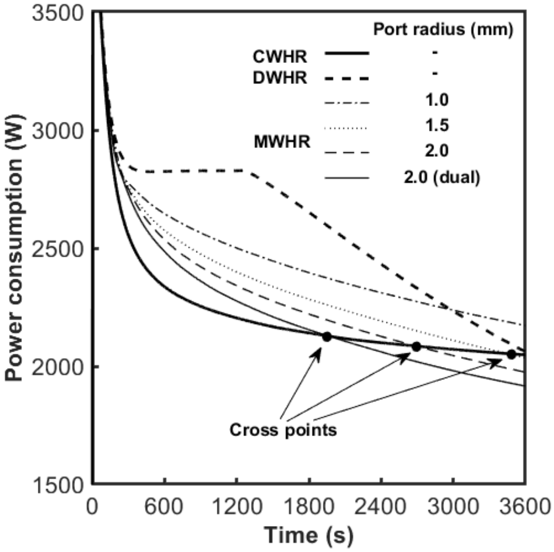

(a)

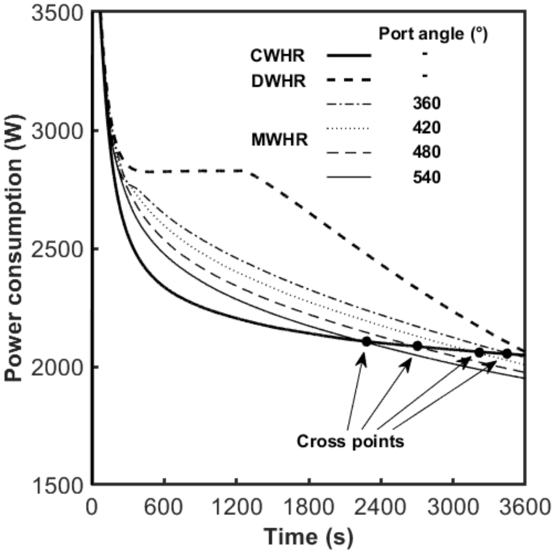

(b)

Figure 4.4 Time-averaged power consumption of MWHR with different (a) port size and (b) port angle. (The port was located at 480 ° and had radius of 2 mm in (a) and (b), respectively.)

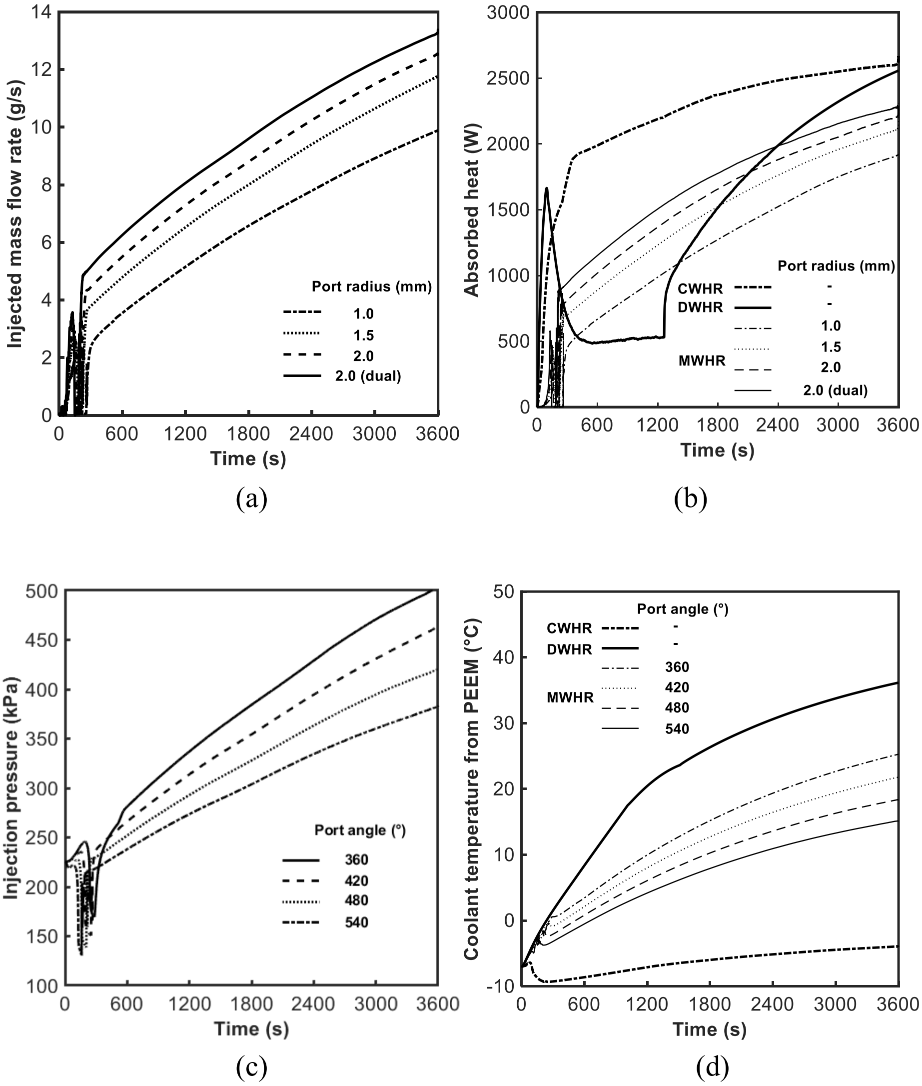

Figure 4.5 System performances with different port geometries: (a) injected mass flow rate and (b) absorbed heat from PEEM with various port sizes; (c) injection pressure and (d) temperature of coolant from PEEM with various port angles.

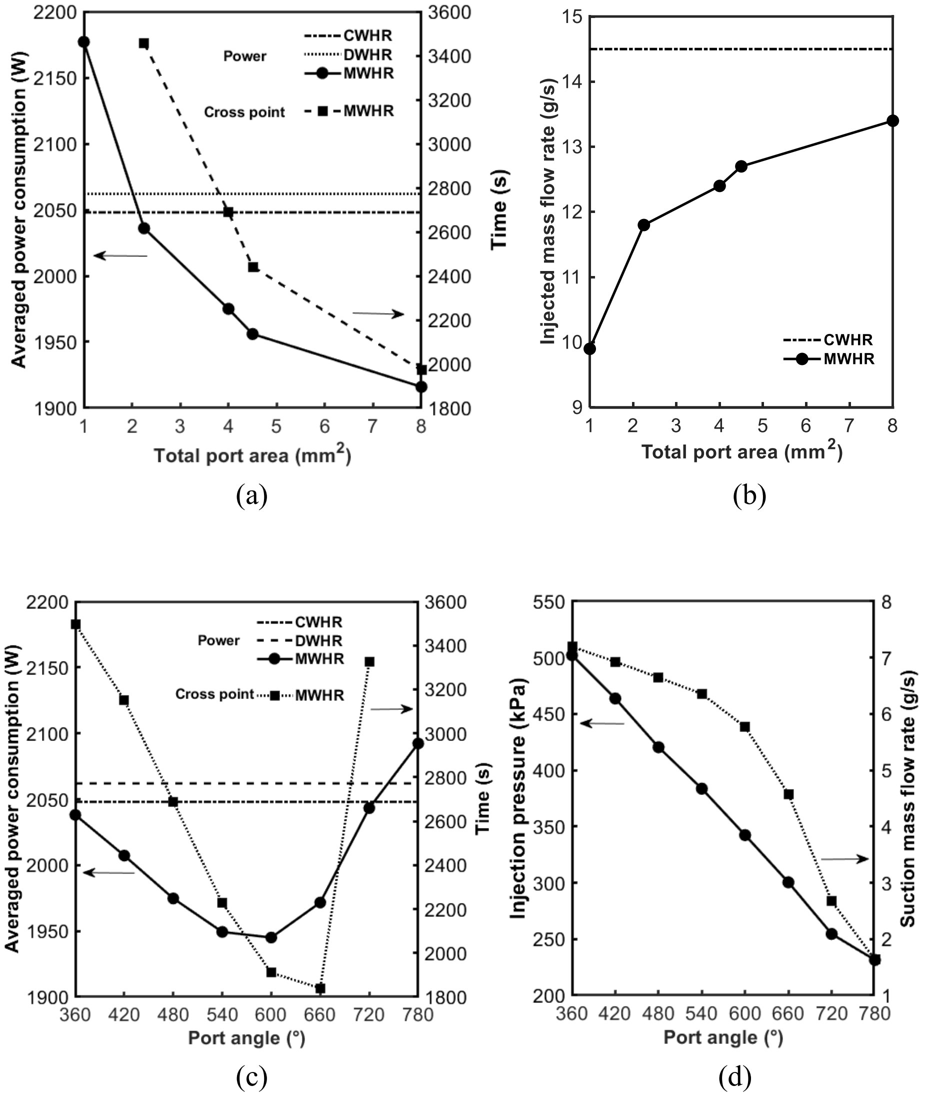

Figure 4.6 System performance variation with different port geometries: (a) time-averaged power consumption and cross point and (b) injected mass flow rate with different port areas; and (c) time-averaged power consumption and cross points and (d) injection pressure and suction mass flow rate with different port angles.

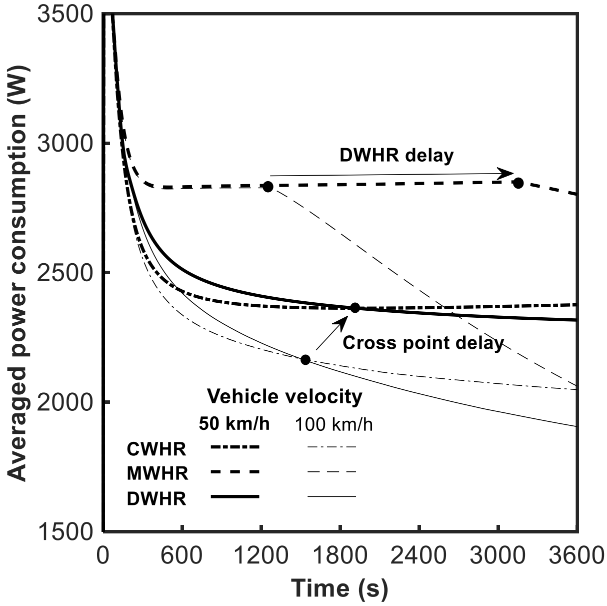

(a)

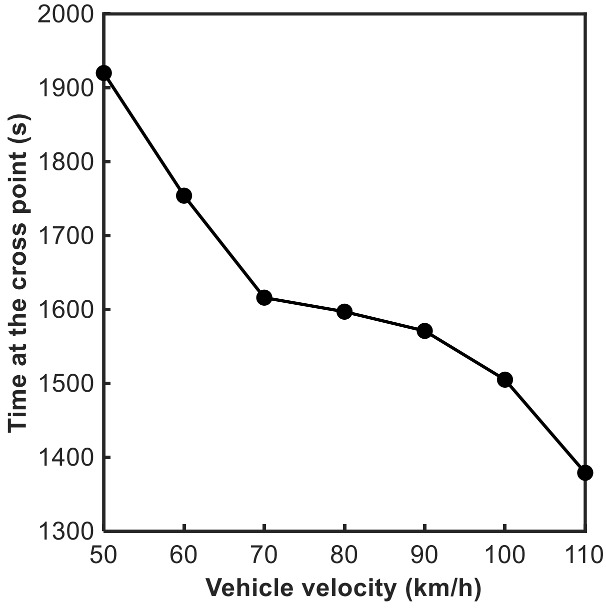

(b)

Figure 4.7 The effect of vehicle velocity on the (a) power consumption and (b) cross points.

Table 4.1 Simulation conditions

Parameter	Values
Ambient air temperature (°C)	−7
Injection port radius (mm)	1 to 2 (increment: 0.5)
Injection port angle (°)	360 to 780 (increment: 60)
Vehicle speed (km/h)	50 to 120 (increment: 10)
Recirculation ratio (%)	50

4.3. Summary

In this chapter, the effect of port design on the performance of heat pump system with MWHR was investigated. From the flow visualization experiment with schlieren apparatus, distinctive flow characteristics of injection process was observed. Based on the experimental result, a novel injection model considering dynamic change in the compression chamber and jet impingement was established and validated. The injection model was integrated with transient heat pump model and PEEM model, incorporated into an ITMS model. The ITMS model evaluated the performance of three waste heat recovery system: CWHR, MWHR, and DWHR, having different temperature level of recovering the waste heat from PEEM. As the existing injection port was designed to properly operate with flash tank or internal heat exchanger, port hole needs redesign to optimize the performance of MWHR. The port hole size and angle were varied in the broad region and the performances of MWHR with different port designs were estimated. Result demonstrates that the larger port hole entails an increase in the injected mass flow rate and the amount of heat absorbed from PEEM. On the other hand, the angle at which the port is located mainly determines the pressure of chamber and corresponding temperature level recovering waste heat. As the temperature level decreases, the injection initiates early and the heat required to raise the temperature of PEEM decreases, saving the total power consumption. However, larger port angle interrupts the suction flow from evaporator when the port opens before suction chamber is closed. The optimal port angle is 660 ° and 600 ° in terms of the power consumption and the time at the cross point where the accumulated power consumption of MWHR becomes less than that of CWHR. Furthermore, the cross points are advanced with faster vehicle speed because larger amount of waste heat is efficiently utilized with MWHR. I expect that the results provide an insight on the port design in MWHR and promote broad adoption of MWHR as a solution to EV range reduction.

Chapter 5. Active battery thermal management strategy[5]

5.1. Introduction

Many EVs adopted liquid-based cooling methods to manage the thermal state of ESS [16, 17]. However, conventional liquid-based BTMS did not heat the battery under cold-start conditions as a significant amount of energy is required to raise the temperature of the ESS. Instead, conventional BTMS used the self-heating of the battery, depending on the reversible heat generation from electrochemical reaction and Joule heating with internal resistance [59]. Few studies focused on the preheating method [38, 74, 75] including internal heating with alternating or pulse current, and external heating with air, liquid, or heat pipe. However, none of the studies have utilized a heat pump system as a heating device except for Leighton et al. [23], which simply flowed the hot coolant with a constant flow rate to ESS without considering the overall system performance. This study suggests active BTMS using a secondary loop in an EV heat pump system. Experiments on the cell-level performance were conducted at low temperatures, and the pack-level ESS thermal model [59]

[5] The contents of chapter 5 were published as in *Energy* [146] on 2023

reflected the low-temperature performance based on the experimental results. A transient heat pump model in the previous study [136] was integrated with the ESS thermal model to establish the ITMS model. The ITMS model estimated the system performance, which included both cabin heating and battery thermal management. The overall system performances under cold-startup conditions were analyzed with three BTMSs: active heating of ESS with the hot coolant, heat recovery from ESS with the cold coolant, and self-heating without any thermal management. The optimal BTMS was obtained with the ITMS model under various ambient air temperatures, driving profiles, and initial SOC conditions. Furthermore, the preheating with the heat pump system was compared with preheating by conventional positive temperature coefficient heater (PTCH) in terms of power consumption and preheating performance. This active BTMS is expected to suggest the optimal BTMS, contributing to the driving range extension of EVs.

5.2. Battery model description

5.2.1. Battery performance experiment at low temperatures

The low-temperature performance of the battery was investigated with internal resistance and capacity measurement tests. A lithium-ion battery, having a capacity of 1000 mAh, was selected and experiments were conducted under various power, temperature, and SOC conditions. The battery was submerged in a dielectric coolant to maintain the battery temperature. As liquid has much higher convective heat transfer coefficient than the air [112], the battery maintained a stable isothermal state, compared with the conventional climatic chamber. The temperature of the dielectric coolant was controlled with a bath-circulator, which can preserve the temperature of the bath from -30 °C to 60 °C. WPG100HP was used as a potentiostat and galvanostat, which can load a constant current on the battery up to 5 A.

As the previous studies on battery performance at low temperatures focused on the dependence of internal resistances on the temperature, SOC, and C-rate. In this experiment, the battery performance was reorganized based on power instead of the current, considering that an EV requires certain power through a battery management system (BMS). Furthermore, existing studies provided the internal resistances with discrete SOC. However, this study aims to identify the available EV range around battery depletion (full discharged state), the voltage was measured with continuous SOC change. We used a constant power protocol from 0.2 W to 2 W, which covers a narrow and low power range. Those values were selected to represent actual vehicle power consumption; 0.2W and 2W correspond to the power consumption of EV with the speed of 30 km/h and 140 km/h, respectively. Those operating temperatures varied from -20 °C to 25 °C, and the SOC was continuously decreased from a fully charged to fully discharged state.

Figure 5.1 shows that the capacity at -20 °C decreases up to 74% and 51% compared with the nominal capacity of 1 Ah. The capacity fade at low temperature was more prominent when the battery consumed higher power as other researches presented [65, 137]. On the other hand, notable results presented that capacity increased with higher power consumption in low-temperature cases, which was also shown by other studies [26, 27]. The results were significant as the purpose of this study is to evaluate the trade-off between the battery performance enhancement and additional power consumption on the battery heating. Those phenomena were reflected in the following battery thermal model.

The thermal behavior of the ESS originates from heat generation, internal conduction, and external convection to the coolant. Two types of heat generations were considered; reversible heat generation and irreversible heat generation.

$$Q_{rev} = IT\left(\frac{\partial U}{\partial T}\right) = T\Delta s \qquad \text{Eq. (5.1)}$$

$$Q_{irr} = I(U - V) = I^2 R_{int} \qquad \text{Eq. (5.2)}$$

Reversible heat generation Q_{rev} is expressed as the Eq. (5.1), which is a product of temperature T and entropy change Δs measured in experiments [120]. Irreversible heat generation Q_{irr} is caused by internal resistance with current and expressed as the product of internal resistance R_{int} and square of internal current I as presented in Eq. (5.2). Both equations are presented in terms of OCV, denoted as U, and rearranged in the aforementioned form. Actual power consumption of the electric motor was calculated from the vehicle dynamics and motor efficiency map.

Figure 5.2 (b) shows a schematic diagram of the thermal resistance circuit in ESS. The thermal resistance of each component in ESS was calculated with the thermal properties and geometry of each component (detailed parameters are presented in the previous study [59]). A finite element method [112] was used to consider the spatial gradient of temperature distribution. Each grid of cells was assumed to have homogenous heat generation and the heat was conducted to the adjacent grid. The metal fin and thermal interface material conveyed heat to the coolant, which flows bottom side of the ESS. Test data from actual EV tests with different vehicle velocities were used to validate the ESS thermal model, which estimated the temperature of the battery with boundary conditions of coolant inlet temperature and flow rate through the cooling channel. Figure 5.3 shows the model estimation results with a reasonable error of around 2 °C

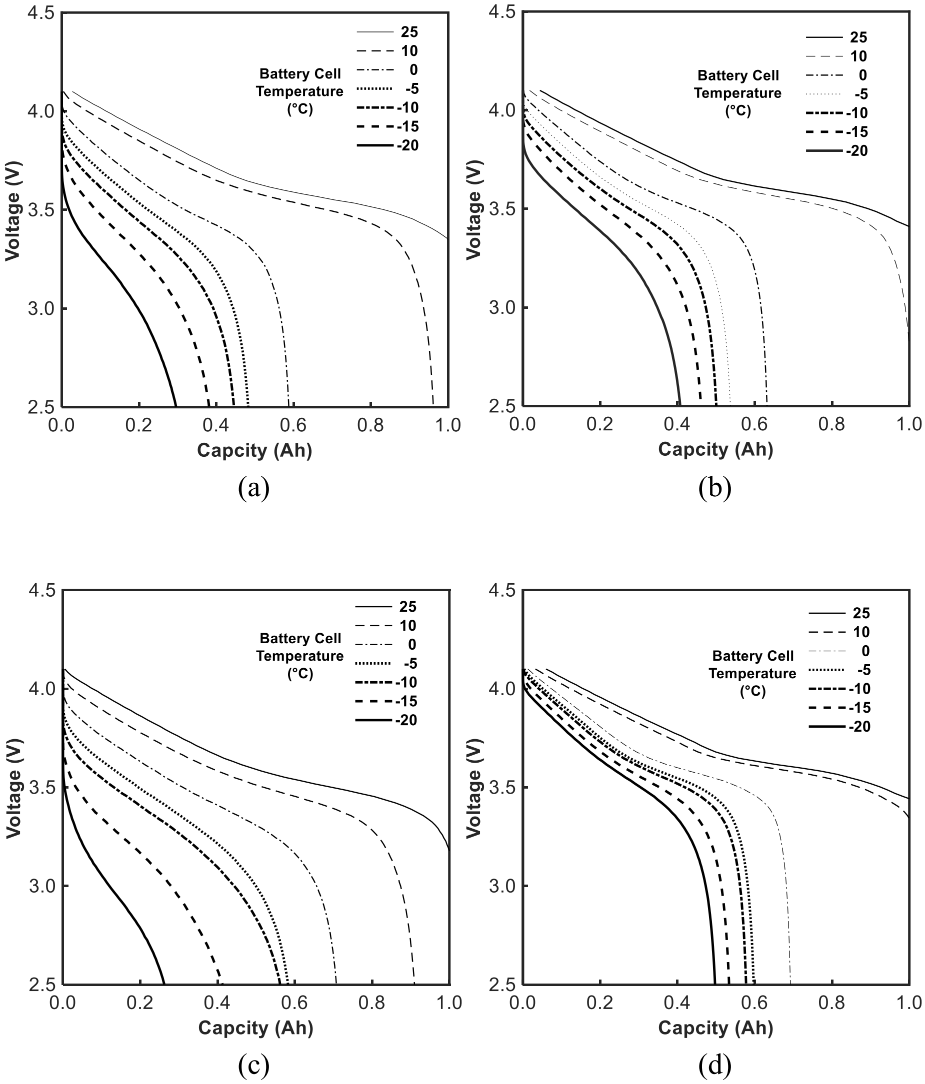

Figure 5.1 Battery capacities with different temperature and power consumptions: (a) 0.2W, (b) 0.5 W, (c) 1 W, and (d) 2 W

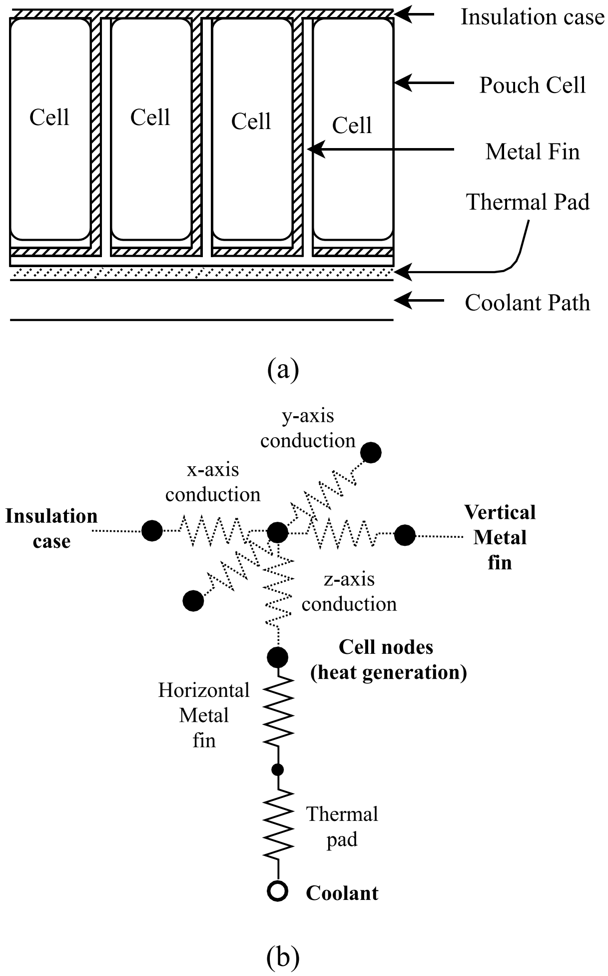

Figure 5.2 Schematic diagram of (a) thermal components and (b) thermal resistance circuit of ESS

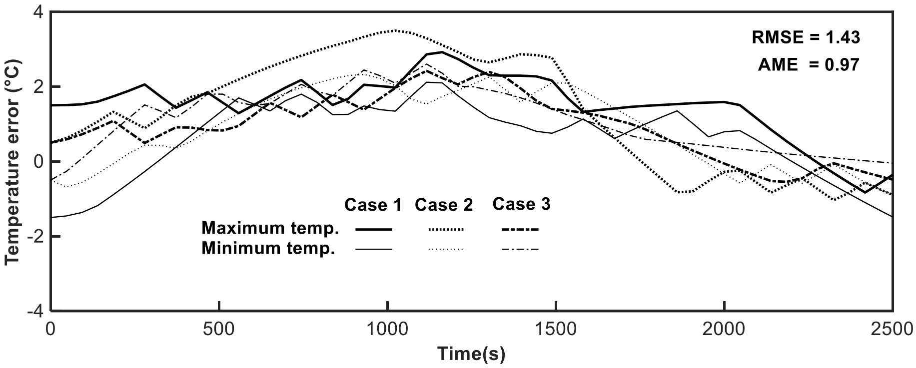

Figure 5.3 Validation results of the ESS thermal model. Minimum and maximum temperatures of the ESS were compared, and bumpy profiles were obatined due to the discrete time steps in the measurement. (RMSE: root mean square error, AME: absolute mean error)

5.2.2. Battery heating strategies

The models explained above were integrated into the ITMS model by thermally combining transient heat pump model and ESS thermal model. As shown in Figure 5.4, three thermal management systems were modeled to analyze the BTMSs. The self-heating BTMS in Figure 5.4 (a) was dependant on the self-heating effect of the ESS to heat the battery; whereas the active heating and heat recovery BTMSs in Figure 5.4 (b) and (c) actively managed the thermal state of the ESS. The active heating BTMS transferred the heat from the heat pump system to the ESS through the hot coolant. The hot coolant from the condenser separated and flowed into the indoor heat exchanger (IDHX) and ESS, respectively. In the ITMS model, the inlet temperatures of IDHX and ESS were equally set as the outlet coolant temperature of the condenser. The two streams were merged before entering the condenser, and the temperature was set as the weighted average temperature by the flow rate through ESS and IDHX. On the other hand, the heat recovery BTMS utilized cold coolant from the evaporator to recover the heat generation from ESS. The cold coolant split into two streams, flowing through ODHX and ESS to absorb heat from the ambient air and ESS, respectively. The hot coolant from condenser flowed to ESS in the active heating BTMS.

In active heating BTMS, the heating capacity from the heat pump system was shared by two thermal objects; cabin and ESS. Therefore, insufficient heat was provided to the cabin, requiring additional power consumption of the PTCH. Nevertheless, the active heating BTMS was preferable when the performance enhancement of the battery by temperature increase was more significant. On the other hand, heat recovery BTMS augmented the heating capacity provided to the cabin by utilizing an additional heat source, ESS. The increased heating capacity saved power consumption of the PTCH, which was advantageous when the temperature of ESS had a relatively minor effect on the battery performance.

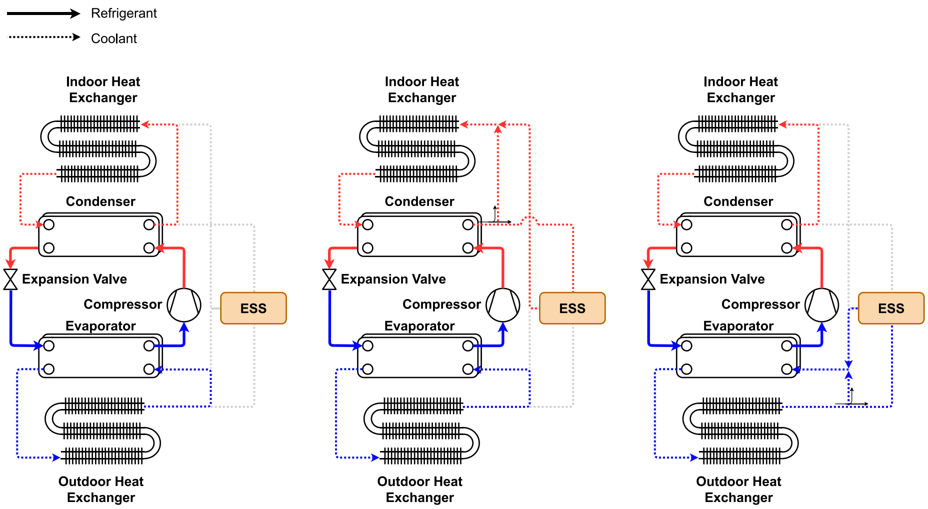

Figure 5.4 Schematic diagram of three BTMSs; (a) self-heating, (b) active heating, and (c) heat recovery

5.3. Results and discussion

Results were thoroughly investigated from the perspectives of overall system performance and preheating performance under cold start conditions.

Three BTMSs including self-heating, active heating, and heat recovery were denoted as SHTMS, AHTMS, and HRTMS, respectively. The vehicle was considered to be soaked at -15 °C and drove at the speed of 100 km/h. The initial SOC was 0.65, which is slightly higher than the minimum SOC, capable of providing enough power to obtain the vehicle speed of 100 km/h, to analyze the behavior until complete SOC depletion. SOC was considered depleted when the cell voltage reached the cut-off voltage of 2.5 V. The heating demand of the cabin was equally set as 4 kW in three BTMSs, where the insufficient capacity from the heat pump was supplemented by PTCH.

The main differences between the BTMSs are the temperature of ESS as shown in Figure 5.5 (a). As the coolant flowing through the ESS came from the condenser, the hot coolant provided heat to the ESS with AHTMS, whereas the cold coolant from the evaporator absorbed heat from the ESS with HRTMS. Therefore, the average temperature of ESS was relatively high with AHTMS and low with HRTMS; and that of SHTMS resided in the intermediate region. Figure 5.5 (b) shows the heat transfer rate from the coolant to ESS, where the negative sign of heat transfer with HRTMS indicates heat absorption from the

ESS and vice versa. The heat generations in the battery cell are also presented in Figure 5.5 (b). As mentioned above, heat generation is mainly affected by battery temperature, which affects both the irreversible and reversible heat generation. The convex shape of heat generation was related with the combined effect of power consumption, SOC, and temperature on the internal resistance of the battery, which will be discussed later.

Figure 5.5 (d) shows the power consumption trend of each BTMS. Total power consumption was a summation of the power consumption of the compressor and PTCH. As the AHTMS allocated a certain amount of heating capacity to the ESS, the heat provided in the cabin is not sufficient as that of SHTMS and HRTMS. Therefore, additional power was consumed at PTCH with AHTMS, as the thin lines in Figure 5.5 (d) shows. The total power consumption was the highest with AHTMS as the PTCH was dominant due to the smaller COP than the heat pump system. However, AHTMS had advantages in terms of heat pump performance. From the perspective of a heat pump, ESS is an additional low-temperature heat sink (than cabin air), whereas HRTMS had an additional higher temperature (than the ambient air) heat source. The dual-source heat pump operation such as HRTMS cannot efficiently utilize both heat sources due to heat imbalance problem, as reported in other research [31, 32]. Besides, an additional heat sink with a low temperature is desirable because the heat sink lowers the condensing pressure of the heat pump system, resulting in the enhancement of COP [140]. The pressure change in Figure 5.5 (c) shows the effect of ESS utilization as a heat source or sink. The evaporating pressure with HRTMS is higher than that of SHTMS and AHTMS, while the condensing pressure was also higher due to a larger mass flow rate with a higher suction density of refrigerant. On the other hand, the condensing pressure with AHTMS was much lower, so the pressure ratio was smaller. Therefore, the total power consumption of the compressor was the smallest with AHTMS as shown in the grey lines in Figure 5.5 (d).

The main purpose of this investigation is to find out the BTMS with the longest driving range. The driving range is determined by the timing when the battery is fully discharged. As mentioned above, the battery was considered to be depleted when the cell voltage reaches the cut-off voltage of 2.5 V, as shown in Figure 5.6 (a). The voltage change shows a convex shape, and this trend was determined by the combined effect of power consumption, SOC, and temperature. The cell voltage is determined by open circuit voltage and overpotential, which is expressed as the product of internal resistance and current. The power consumption of the overall system affects both the open circuit voltage and overpotential. The trend of total power consumption in Figure 5.5 (d) decreased after the early stage when only a small amount of heating capacity is provided in the heat pump system, requiring aggressive usage of PTCH. However, the total power consumption increased again because the heat sink temperature, including the cabin and ESS, increased. This variation of total power consumption determined the current of the battery cell, affecting the overpotential. On the other hand, the open circuit voltage is known as a function of SOC [34, 35]. The total power consumption with AHTMS was the highest so that the SOC might be considered to be the lowest. However, Figure 5.6 (b) shows less current consumption with AHTMS because the power consumption is a product of cell voltage and current. The voltage level was higher with AHTMS so that the resultant current was less than that of SHTMS and WHTMS; where AHTMS was more advantageous. The reason for the higher voltage level exists in the dominant dependence of the internal resistance on the temperature. The decreased internal resistance with higher temperature decreased overpotentials, resulting in delayed battery depletion and longer driving range. The driving range with AHTMS increased by 75.8% and 18.8%, compared with that of WHTMS and SHTMS, and that result corresponds to the range extension of 10.5 km and 3.9 km.

On the other hand, BTMSs should consider the cases when the battery is not fully discharged. In this case, we should consider the capacity recovery characteristic of the battery [143]. This study demonstrated that even after the battery is fully discharged, the capacity is recovered when the temperature of the battery rises. This phenomenon can be interpreted as the capacity of the battery is not lost but unavailable at a low temperature. On the contrary, the additional power consumption on the battery heating accompanies the actual migration of a lithium-ion, which cannot be recovered. To the best of our literature survey, there was no research on the negative impact of low-temperature discharge on the battery state-of-health. Therefore, the main objective in a case when the vehicle completes driving before battery is fully discharged is to save the total SOC decrease.

We investigated the non-depleted cases with more mild conditions: soaking temperature of -5 °C, vehicle speed of 50 km/h, and initial SOC of 0.6. Figure 5.7 (a) shows the accumulated current and corresponding SOC. AHTMS shows the most SOC decrease, while the trend with SHTMS and WHTMS was crossed around 1,300 s. This is because of the larger power consumption of AHTMS, as presented in Figure 5.7 (c). However, even though the power consumption trend was similar to the previous case, the resultant current usage was reversed, where the SOC of AHTMS decreased more than that of the others. This is because the voltage abruptly drops when SOC is near zero as shown in the experimental results in Figure 5.1. Therefore, the absolute value and relative change of the cell voltage between three BTMSs in Figure 5.7 (b) were smaller when the battery was operated in the region far from the zero-SOC. Figure 5.7 (d) presents larger temperature differences between BTMSs, but the effect was not influential enough to compensate the larger power consumption with AHWHR. The accumulated current consumption was saved with WHTMS up to 5.3 % and 2.2 %, compared with AHTMS and SHTMS, respectively.

At low SOC and temperature conditions, the ESS cannot provide enough power to the vehicle; a battery preheating can be a solution to this problem. The battery preheating mode operated equally as AHTMS except that the hot coolant did not pass through the IDHX without a need to heat the cabin. The initial SOC and temperature of ESS were 0.45 and -5 °C, respectively; in which conditions, a vehicle cannot even reach the speed of 50 km/h. As shown in Figure 5.8 (a), the maximum power consumption was approximately 1.1 kW, which is quite a small amount compared with the power consumption in driving. As a battery cell shows a similar performance at low temperature when the power consumption is small enough [141], the preheating is possible with any low temperature and SOC conditions. The power consumption of the compressor gradually increased with the temperature rise of ESS. Therefore, the COP of the heat pump system decreased; but the overall power consumed in the preheating can be saved by 38.4%. The heating performance is presented in Figure 5.8 (b), showing that the preheating of an hour increased the temperature of the ESS to 15 °C within the optimal temperature range between 15 °C and 35 °C.

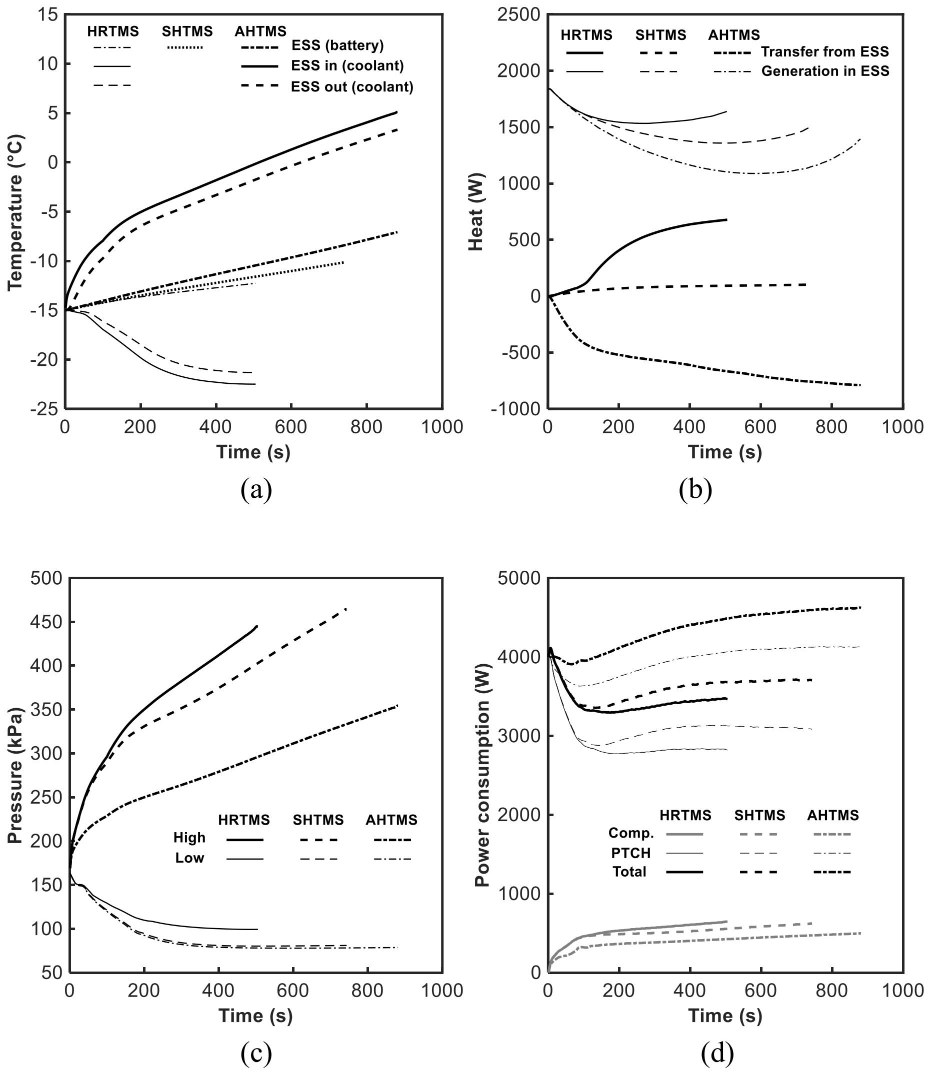

Figure 5.5 System performances of three BTMSs: (a) ESS temperaure, (b) heat transfer and generaion, (c) operating pressure, and (d) power consumption. (Soaking temperautre: -15 °C, initial SOC: 0.65, vehicle speed: 100 km/h)

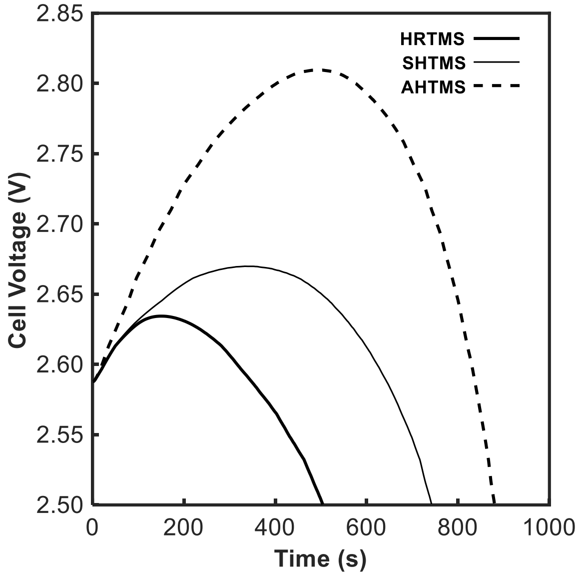

(a)

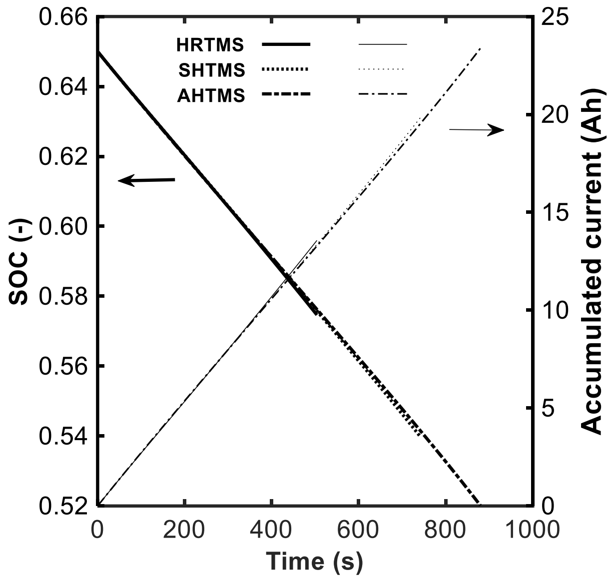

(b)

Figure 5.6 Battery status of three BTMSs: (a) cell voltage and (b) SOC and accumulated current

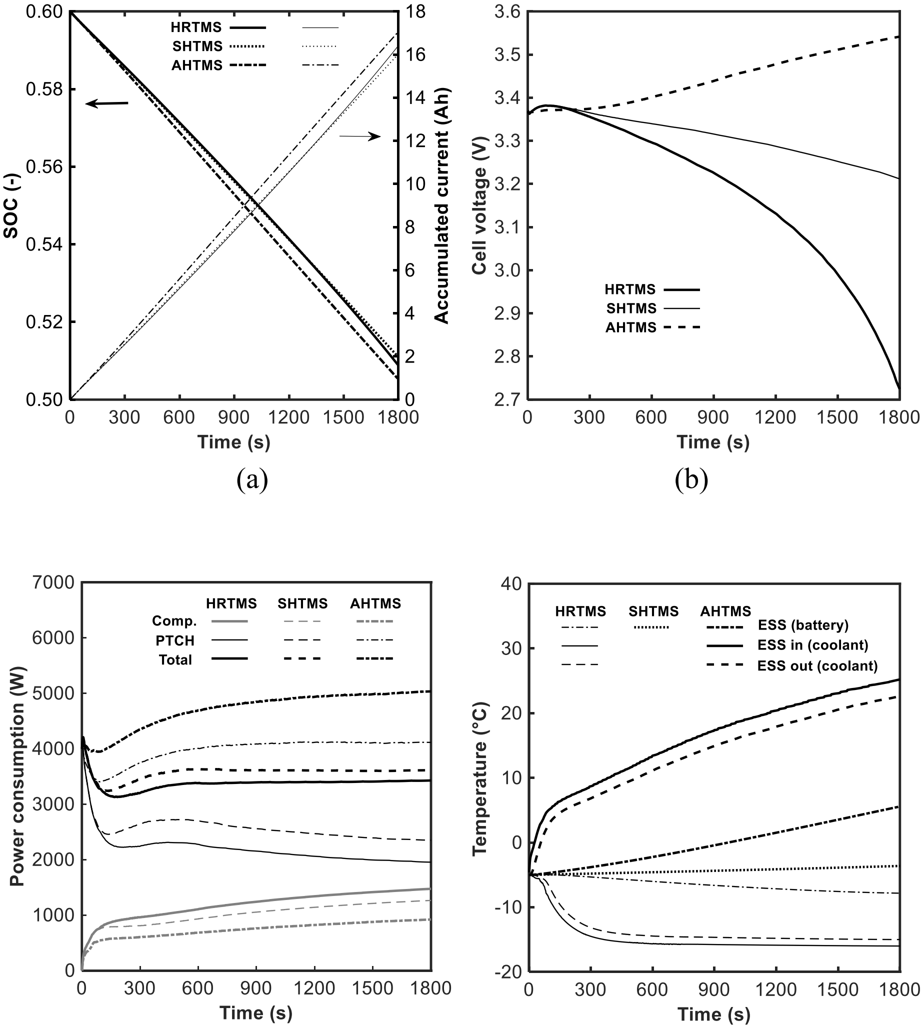

Figure 5.7 System performances of three BTMSs: (a) SOC and accmulated current, (b) cell voltage, (c) power consumption, and (d) ESS temperature. (Soaking temperautre: -5 °C, initial SOC: 0.6, vehicle speed: 50 km/h)

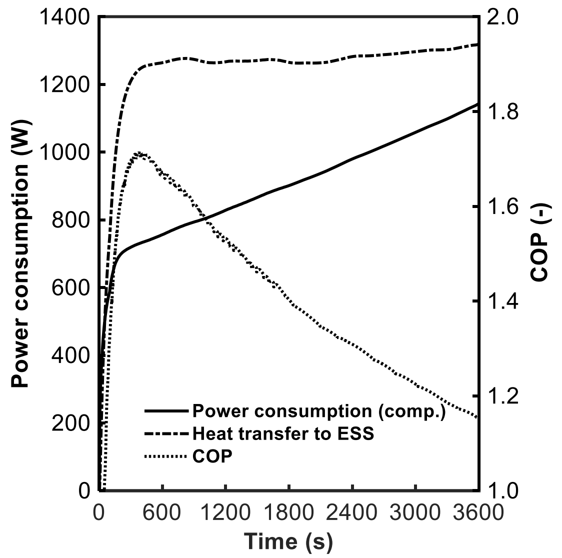

(a)

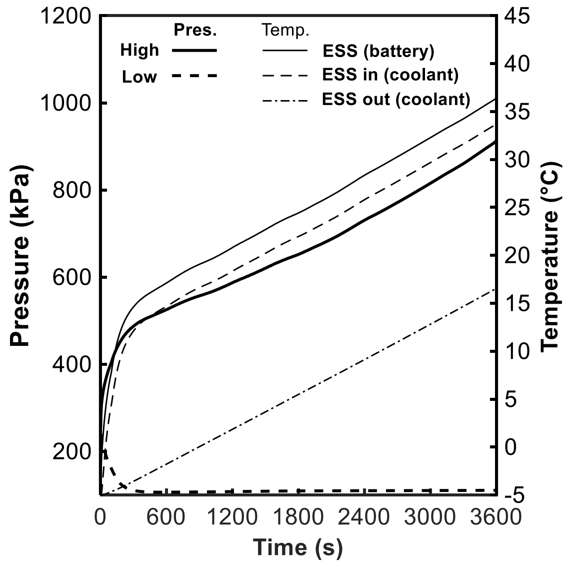

(b)

Figure 5.8 Preheating performance of heat pump system: (a) power consumption, heat transfer, and COP and (b) operating pressure and ESS temperaure

5.4. Summary

In this chapter, I suggested and investigated the performance of BTMSs utilizing the secondary heat pump system in EV. The optimal BTMS should be derived considering the trade-off between additional power consumption on the battery thermal management and enhanced performance of the battery through the thermal management. To evaluate the trade-off, I established the ITMS model, which included the battery thermal model reflecting the low-temperature performance and the transient heat pump model. Based on the ITMS model, I compared the performances of three strategies: AHTMS, HRTMS, and SHTMS. The results demonstrated that the AHTMS with ESS heating improves the driving range of EV up to 18.8% compared with SHTMS. This originated from the dominant dependency of the internal resistance on the temperature rather than power consumption or SOC. The current with AHTMS was less than the WHTMS and SHTMS even with larger power consumption due to increased voltage level. Furthermore, the heat pump performance was also improved with AHTMS by distributing heat capacity to the additional low-temperature heat sink, ESS. On the other hand, the objective of the BTMS was set to save the total current consumption when the ESS was not depleted. The accumulated current with WHTMS was the least because of the absorbed heat from the ESS augmented the heating capacity and saved PTCH usage. In addition, the performance of ESS preheating was analyzed, showing a temperature rise of 20 °C within an hour with 38.4% less power consumption than the PTCH preheating. The ITMS model I suggested is expected to derive the optimal BTMS under cold-start conditions, contributing to the range extension of the EV.

Chapter 6. Concluding remarks

As a solution to EV range reduction problem, heat pumps are widely adopted to replace PTC heater as a cabin heating device. However, heating capacity of heat pumps decreases at low ambient temperature, whereas the heating demand of cabin increases. The insufficient heating capacity is supplemented by PTC heater, resulting in parasitic effect on the EV range. Therefore, I suggest the multi-level thermal management system to efficiently absorb the waste heat from PEEM and properly manage the thermal state of ESS. The MWHR benefits from active utilization of different temperature levels in heat pump system.

In chapter 2, I investigated the effect of temperature level, at which the waste heat is recovered. The performances of heat pump system with waste heat recovery were evaluated with experimental and numerical methods. Conventional waste heat recovery at evaporating temperature was compared with two different temperature levels: condensing temperature and intermediate temperature. By elevating the temperature level, the refrigerant after recovering the waste heat had higher enthalpy and pressure, which results in the augmentation in the heating capacity and savings in power consumption of compressor. Experimental results showed that the heating capacity with

MWHR increased up to 72.5% when the heat pump operated in the coldest condition of -20 °C; and numerical analysis verified that power savings up to 23.2% when recovering heat at the condensing temperature.

In chapter 3, I proposed the operating strategy of MWHR depending on the driving conditions. I developed an ITMS model which integrated the transient heat pump model with vapor injection and thermal model of electric devices. The ITMS model evaluated the performance of heat pump system with different heat recovery temperature and derived the optimal temperature level. To absorb the waste heat at the higher temperature level, the waste heat should be utilized the heat up the temperature of heat source (PEEM). Therefore, initial unavailability of waste heat at the early stage should be compensated with the enhanced heating performance of the system. I suggested the cross point when the initial loss is completely compensated and the trend of the cross points in various operating conditions. Results showed that the cross points were advanced with higher vehicle speed and low ambient temperature, when the passengers mainly suffer from the range anxiety.

In chapter 4, I optimized the port design, which critically affects the performance of heat pump with vapor injection. As existing injection ports were designed to properly operate with flash tank or internal heat exchanger, the ports require a redesign to perform well with MWHR. Various port design was examined with different port size and location. A novel injection model was devised to accurately reflect the phenomena in the injection process. Result demonstrated that the larger port hole entails an increase in the injected mass flow rate and the amount of heat absorbed from PEEM. On the other hand, the angle at which the port is located mainly determines the pressure of chamber and corresponding temperature level recovering waste heat. The optimal port angle is 660 ° and 600 ° in terms of the power consumption and the time at the cross point.

In chapter 5, I inspected the effect of thermal management of ESS from the systematic perspective. The internal resistance of lithium-ion battery significantly increases at low temperatures, accompanying the power decrease and capacity fade. Therefore, low-temperature operation of ESS should be avoided, but the heating of ESS requires large amount of energy due to massive volume and heat capacity of ESS. The trade-off between performance enhancement from temperature rise of ESS and the energy consumed in heating the ESS should be estimated. The results verified that the active heating of ESS with heat pump improves the driving range of EV up to 18.8% compared with non-heating case. Furthermore, I propose the absorption of heat generated by ESS to supplement the heating capacity when the battery has enough SOC. In addition, preheating of ESS before driving was achieved by heat pump system with 38.4% less power consumption.

In conclusion, the multi-level thermal management system efficiently absorbs heat from the PEEM by actively utilizing different temperature levels. The vapor injection technique supplemented the intermediate temperature level to subdivide the temperature levels into three. The ITMS model derived the optimal temperature level, where the waste heat is utilized most efficiently. In addition, the ITMS model also verified that the active heating of ESS is advantageous on the range extension of EV by alleviating the rise of internal resistance of lithium-ion battery at low temperature.

Reference

[1] V. Masson-Delmotte, P. Zhai, H.-O. Pörtner, D. Roberts, J. Skea, P. R. Shukla, A. Pirani, W. Moufouma-Okia, C. Péan, and R. Pidcock, "Global Warming of 1.5 C," *An IPCC Spec. Rep. impacts Glob. Warm.*, vol. 1, no. 5, 2018.

[2] X. Zhang, J. Xie, R. Rao, and Y. Liang, "Policy Incentives for the Adoption of Electric Vehicles across Countries," *Sustainability*, vol. 6, no. 11, pp. 8056–8078, 2014, doi: 10.3390/su6118056.

[3] B. M. Al-Alawi and T. H. Bradley, "Total Cost of Ownership, Payback, and Consumer Preference Modeling of Plug-in Hybrid Electric Vehicles," *Appl. Energy*, vol. 103, no. 2013, pp. 488–506, 2013, doi: 10.1016/j.apenergy.2012.10.009.

[4] A. S. Brouwer, T. Kuramochi, M. van den Broek, and A. Faaij, "Fulfilling the Electricity Demand of Electric Vehicles in the Long Term Future: An Evaluation of Centralized and Decentralized Power Supply Systems," *Appl. Energy*, vol. 107, pp. 33–51, 2013, doi: 10.1016/j.apenergy.2013.02.005.

[5] A. Foley, B. Tyther, P. Calnan, and B. Ó Gallachóir, "Impacts of Electric Vehicle Charging under Electricity Market Operations," *Appl.*

Energy, vol. 101, no. 2013, pp. 93–102, 2013, doi: 10.1016/j.apenergy.2012.06.052.

[6] U. S. EIA, "Electricity Explained. Electricity in the United States," *US Energ y Inf. Adm.*, 2021.

[7] D. Rutherford, "Lessons Learned from 10 Years in International Environmental Policymaking," 2019.

[8] C. Thiel, A. Perujo, and A. Mercier, "Cost and CO2 Aspects of Future Vehicle Options in Europe under New Energy Policy Scenarios," *Energy Policy*, vol. 38, no. 11, pp. 7142–7151, 2010, doi: 10.1016/j.enpol.2010.07.034.

[9] D. Santini and A. Burnham, "Reducing Light Duty Vehicle Fuel Consumption and Greenhouse Gas Emissions: The Combined Potential of Hybrid Technology and Behavioral Adaptation," *SAE Int. J. Altern. Powertrains*, vol. 2, no. 2, pp. 314–324, 2013, doi: 10.4271/2013-01-1282.

[10] R. Schmidt and M. Iyengar, "Information Technology Energy Usage and Our Planet," in *2008 11th Intersociety Conference on Thermal and Thermomechanical Phenomena in Electronic Systems*, 2008, pp. 1255–1275.

[11] J. H. M. Langbroek, J. P. Franklin, and Y. O. Susilo, "The Effect of

Policy Incentives on Electric Vehicle Adoption," *Energy Policy*, vol. 94, pp. 94–103, 2016.

[12] R. T. Doucette and M. D. McCulloch, "Modeling the Prospects of Plug-in Hybrid Electric Vehicles to Reduce CO2 Emissions," *Appl. Energy*, vol. 88, no. 7, pp. 2315–2323, 2011, doi: 10.1016/j.apenergy.2011.01.045.

[13] E. M. Bibra, E. Connelly, M. Gorner, C. Lowans, L. Paoli, J. Tattini, and J. Teter, "Global EV Outlook 2021—Accelerating Ambitions Despite the Pandemic." International Energy Agency Paris, France, 2021.

[14] A. Bui and Z. Yang, "US Light-Duty Vehicle Greenhouse Gas Standards for Model Years 2023–2026 and Corporate Average Fuel Economy Standards for Model Years 2024–2026," *POLICY*, 2022.

[15] A. K. Breed, D. Speth, and P. Plötz, "CO2 Fleet Regulation and the Future Market Diffusion of Zero-Emission Trucks in Europe," *Energy Policy*, vol. 159, 2021, doi: 10.1016/j.enpol.2021.112640.

[16] J. A. Sanguesa, V. Torres-Sanz, P. Garrido, F. J. Martinez, and J. M. Marquez-Barja, "A Review on Electric Vehicles: Technologies and Challenges," *Smart Cities*, vol. 4, no. 1, pp. 372–404, 2021, doi: 10.3390/smartcities4010022.

[17] M. M. Thackeray, C. Wolverton, and E. D. Isaacs, “Electrical Energy Storage for Transportation—Approaching the Limits of, and Going beyond, Lithium-Ion Batteries,” *Energy Environ. Sci.*, vol. 5, no. 7, pp. 7854–7863, 2012.

[18] D. Hafemeister, B. Levi, M. Levine, and P. Schwartz, “American Physical Society Physics of Sustainable Energy,” *UC, Berkeley*, 2008.

[19] N. Lutsey and M. Nicholas, “Update on Electric Vehicle Costs in the United States through 2030,” *Int. Counc. Clean Transp*, vol. 12, 2019.

[20] T. Franke, I. Neumann, F. Bühler, P. Cocron, and J. F. Krems, “Experiencing Range in an Electric Vehicle: Understanding Psychological Barriers,” *Appl. Psychol.*, vol. 61, no. 3, pp. 368–391, 2012, doi: 10.1111/j.1464-0597.2011.00474.x.

[21] H. Lohse-Busch, M. Duoba, E. Rask, K. Stutenberg, V. Gowri, L. Slezak, and D. Anderson, “Ambient Temperature (20°F, 72°F and 95°F) Impact on Fuel and Energy Consumption for Several Conventional Vehicles, Hybrid and Plug-in Hybrid Electric Vehicles and Battery Electric Vehicle,” *SAE Tech. Pap.*, 2013, doi: 10.4271/2013-01-1462.

[22] M. A. Jeffers, L. Chaney, and J. P. Rugh, “Climate Control Load Reduction Strategies for Electric Drive Vehicles in Cold Weather,”

SAE Int. J. Passeng. Cars - Mech. Syst., 2016, doi: 10.4271/2016-01-0262.

[23] D. Leighton, "Combined Fluid Loop Thermal Management for Electric Drive Vehicle Range Improvement," *SAE Int. J. Passeng. Cars - Mech. Syst.*, 2015, doi: 10.4271/2015-01-1709.

[24] B. Yu, J. Yang, D. Wang, J. Shi, and J. Chen, "Energy Consumption and Increased EV Range Evaluation through Heat Pump Scenarios and Low GWP Refrigerants in the New Test Procedure WLTP," *Int. J. Refrig.*, vol. 100, pp. 284–294, 2019, doi: 10.1016/j.ijrefrig.2019.01.033.

[25] D.-Y. Lee, C.-W. Cho, J.-P. Won, Y. C. Park, and M.-Y. Lee, "Performance Characteristics of Mobile Heat Pump for a Large Passenger Electric Vehicle," *Appl. Therm. Eng.*, vol. 50, no. 1, pp. 660–669, 2013, doi: 10.1016/j.applthermaleng.2012.07.001.

[26] F. Qin, S. Shao, C. Tian, and H. Yang, "Experimental Investigation on Heating Performance of Heat Pump for Electric Vehicles in Low Ambient Temperature," *Energy Procedia*, vol. 61, pp. 726–729, 2014, doi: 10.1016/j.egypro.2014.11.952.

[27] J. P. Zammit, P. J. Shayler, and I. Pegg, "Thermal Coupling and Energy Flows between Coolant, Engine Structure and Lubricating Oil

during Engine Warm Up," in *Vehicle Thermal Management Systems Conference and Exhibition (VTMS10)*, 2011, pp. 177–188.

[28] J. D. Trapy and P. Damiral, "An Investigation of Lubricating System Warm-up for the Improvement of Cold Start Efficiency and Emissions of SI Automotive Engines," *SAE Trans.*, pp. 1635–1645, 1990.

[29] K. Liu, J. Wang, T. Yamamoto, and T. Morikawa, "Exploring the Interactive Effects of Ambient Temperature and Vehicle Auxiliary Loads on Electric Vehicle Energy Consumption," *Appl. Energy*, vol. 227, pp. 324–331, 2018.

[30] M. Allen, "Electric Range for the Nissan Leaf & Chevrolet Volt in Cold Weather," *Fleet Carma*, vol. 12, 2013.

[31] K. Bennion, "Electric Motor Thermal Management R & D," *Nrel/Mp-5400-64944*, no. April, 2016.

[32] G. Moreno, "Power Electronics Thermal Management R & D," no. April, pp. 1–16, 2015.

[33] J. P. Rugh, A. Pesaran, and K. Smith, "Electric Vehicle Battery Thermal Issues and Thermal Management Techniques (Presentation)," *Natl. Renew. Energy Lab.(NREL), Golden, CO (United States)*, no. NREL/PR-5400-52818, 2013, [Online]. Available: https://www.nrel.gov/docs/fy13osti/52818.pdf

[34] F. Nielsen, Å. Uddheim, and J. O. Dalenbäck, "Potential Energy Consumption Reduction of Automotive Climate Control Systems," *Appl. Therm. Eng.*, vol. 106, pp. 381–389, 2016, doi: 10.1016/j.applthermaleng.2016.05.137.

[35] M. Giansoldati, R. Danielis, L. Rotaris, and M. Scorrano, "The Role of Driving Range in Consumers' Purchasing Decision for Electric Cars in Italy," *Energy*, vol. 165, pp. 267–274, 2018, doi: 10.1016/j.energy.2018.09.095.

[36] K. Y. Kim, S. C. Kim, and M. S. Kim, "Experimental Studies on the Heating Performance of the PTC Heater and Heat Pump Combined System in Fuel Cells and Electric Vehicles," *Int. J. Automot. Technol.*, vol. 13, no. 6, pp. 971–977, 2012, doi: 10.1007/s12239-012-0099-z.

[37] Z. Zhang, C. Liu, X. Chen, C. Zhang, and J. Chen, "Annual Energy Consumption of Electric Vehicle Air Conditioning in China," *Appl. Therm. Eng.*, vol. 125, pp. 567–574, 2017, doi: 10.1016/j.applthermaleng.2017.07.032.

[38] T. Zhu, H. Min, Y. Yu, Z. Zhao, T. Xu, Y. Chen, X. Li, and C. Zhang, "An Optimized Energy Management Strategy for Preheating Vehicle-Mounted Li-Ion Batteries at Subzero Temperatures," *Energies*, vol. 10, no. 2, pp. 1–23, 2017, doi: 10.3390/en10020243.

[39] Q. Peng and Q. Du, "Progress in Heat Pump Air Conditioning Systems for Electric Vehicles—A Review," *Energies*, vol. 9, no. 4, 2016, doi: 10.3390/en9040240.

[40] Z. Zhang, J. Wang, X. Feng, L. Chang, Y. Chen, and X. Wang, "The Solutions to Electric Vehicle Air Conditioning Systems: A Review," *Renew. Sustain. Energy Rev.*, vol. 91, pp. 443–463, 2018, doi: 10.1016/j.rser.2018.04.005.

[41] M. Yang, B. Wang, X. Li, W. Shi, and L. Zhang, "Evaluation of Two-Phase Suction, Liquid Injection and Two-Phase Injection for Decreasing the Discharge Temperature of the R32 Scroll Compressor," *Int. J. Refrig.*, vol. 59, pp. 269–280, 2015, doi: 10.1016/j.ijrefrig.2015.08.004.

[42] L. Feng and P. Hrnjak, "Experimental Study of an Air Conditioning-Heat Pump System for Electric Vehicles," *SAE Technical Paper Series*. 2016. doi: 10.4271/2016-01-0257.

[43] H.-S. Lee and M.-Y. Lee, "Steady State and Start-up Performance Characteristics of Air Source Heat Pump for Cabin Heating in an Electric Passenger Vehicle," *Int. J. Refrig.*, vol. 69, pp. 232–242, 2016, doi: 10.1016/j.ijrefrig.2016.06.021.

[44] W. Li, R. Liu, Y. Liu, D. Wang, J. Shi, and J. Chen, "Performance

Evaluation of R1234yf Heat Pump System for an Electric Vehicle in Cold Climate,” *Int. J. Refrig.*, vol. 115, pp. 117–125, 2020.

[45] S. Hirai, T. Kataoka, T. Kumada, and T. Goto, “The Humidity Control System Applied to Reduce Ventilation Heat Loss of HVAC Systems,” *SAE Technical Paper Series*. 2011. doi: 10.4271/2011-01-0134.

[46] Z. Zhang, W. Li, C. Zhang, and J. Chen, “Climate Control Loads Prediction of Electric Vehicles,” *Appl. Therm. Eng.*, vol. 110, pp. 1183–1188, 2017, doi: 10.1016/j.applthermaleng.2016.08.186.

[47] J. P. Rugh, R. S. Howard, R. B. Farrington, M. R. Cuddy, and D. M. Blake, “Innovative Techniques for Decreasing Advanced Vehicle Auxiliary Loads,” 2000. doi: 10.4271/2000-01-1562.

[48] Z. Zhang, D. Wang, C. Zhang, and J. Chen, “Electric Vehicle Range Extension Strategies Based on Improved AC System in Cold Climate – A Review,” *Int. J. Refrig.*, vol. 88, pp. 141–150, 2018, doi: 10.1016/j.ijrefrig.2017.12.018.

[49] F. Qin, Q. Xue, G. M. Albarracin Velez, G. Zhang, H. Zou, and C. Tian, “Experimental Investigation on Heating Performance of Heat Pump for Electric Vehicles at −20°C Ambient Temperature,” *Energy Convers. Manag.*, vol. 102, pp. 39–49, 2015, doi: 10.1016/j.enconman.2015.01.024.

[50] C. Kwon, M. S. Kim, Y. Choi, and M. S. Kim, “Performance Evaluation of a Vapor Injection Heat Pump System for Electric Vehicles,” *Int. J. Refrig.*, vol. 74, pp. 138–150, 2017, doi: 10.1016/j.ijrefrig.2016.10.004.

[51] J. H. Ahn, H. Kang, H. S. Lee, H. W. Jung, C. Baek, and Y. Kim, “Heating Performance Characteristics of a Dual Source Heat Pump Using Air and Waste Heat in Electric Vehicles,” *Appl. Energy*, vol. 119, pp. 1–9, 2014, doi: 10.1016/j.apenergy.2013.12.065.

[52] Z. Tian, B. Gu, W. Gao, and Y. Zhang, “Performance Evaluation of an Electric Vehicle Thermal Management System with Waste Heat Recovery,” *Appl. Therm. Eng.*, vol. 169, no. January, 2020, doi: 10.1016/j.applthermaleng.2020.114976.

[53] S. Park and D. Jung, “Design of Vehicle Cooling System Architecture for a Heavy Duty Series-Hybrid Electric Vehicle Using Numerical System Simulations,” *J. Eng. Gas Turbines Power*, vol. 132, no. 9, pp. 1–11, 2010, doi: 10.1115/1.4000587.

[54] S. Chowdhury, L. Leitzel, M. Zima, M. Santacesaria, G. Titov, J. Lustbader, J. Rugh, J. Winkler, A. Khawaja, and M. Govindarajalu, “Total Thermal Management of Battery Electric Vehicles (BEVs),” *SAE Tech. Pap.*, vol. 2018-May, no. May, pp. 1–7, 2018, doi:

10.4271/2018-37-0026.

[55] X. Han, H. Zou, J. Wu, C. Tian, M. Tang, and G. Huang, "Investigation on the Heating Performance of the Heat Pump with Waste Heat Recovery for the Electric Bus," *Renew. Energy*, vol. 152, pp. 835–848, 2020, doi: 10.1016/j.renene.2020.01.075.

[56] C.-W. Cho, H.-S. Lee, J.-P. Won, and M.-Y. Lee, "Measurement and Evaluation of Heating Performance of Heat Pump Systems Using Wasted Heat from Electric Devices for an Electric Bus," *Energies*, vol. 5, no. 3, pp. 658–669, 2012, doi: 10.3390/en5030658.

[57] Z. Tian, W. Gan, X. Zhang, B. Gu, and L. Yang, "Investigation on an Integrated Thermal Management System with Battery Cooling and Motor Waste Heat Recovery for Electric Vehicle," *Appl. Therm. Eng.*, vol. 136, no. March, pp. 16–27, 2018, doi: 10.1016/j.applthermaleng.2018.02.093.

[58] X. Chen, J. Wang, A. Griffo, and L. Chen, "Evaluation of Waste Heat Recovery of Electrical Powertrain with Electro-Thermally Coupled Models for Electric Vehicle Applications," *Chinese J. Electr. Eng.*, vol. 7, no. 3, pp. 88–99, 2021, doi: 10.23919/CJEE.2021.000028.

[59] S. Lee, Y. Chung, S. Kim, Y. Jeong, and M. S. Kim, "Investigation on the Performance Enhancement of Electric Vehicle Thermal

Management System Utilizing Floating Loop with Finite Heat Exchanger Size," *Energy Convers. Manag.*, vol. 255, p. 115265, 2022, doi: 10.1016/j.enconman.2022.115265.

[60] N. Javani, I. Dincer, and G. F. Naterer, "Thermodynamic Analysis of Waste Heat Recovery for Cooling Systems in Hybrid and Electric Vehicles," *Energy*, vol. 46, no. 1, pp. 109–116, 2012, doi: 10.1016/j.energy.2012.02.027.

[61] R. Song, M. Cui, and J. Liu, "A Correlation for Heat Transfer and Flow Friction Characteristics of the Offset Strip Fin Heat Exchanger," *Int. J. Heat Mass Transf.*, vol. 115, pp. 695–705, 2017, doi: 10.1016/j.ijheatmasstransfer.2017.08.054.

[62] C. W. Roh and M. S. Kim, "Effects of Intermediate Pressure on the Heating Performance of a Heat Pump System Using R410A Vapor-Injection Technique," *Int. J. Refrig.*, vol. 34, no. 8, pp. 1911–1921, 2011, doi: 10.1016/j.ijrefrig.2011.07.011.

[63] J. Jaguemont, L. Boulon, and Y. Dubé, "A Comprehensive Review of Lithium-Ion Batteries Used in Hybrid and Electric Vehicles at Cold Temperatures," *Appl. Energy*, vol. 164, pp. 99–114, 2016, doi: 10.1016/j.apenergy.2015.11.034.

[64] W. Wu, S. Wang, W. Wu, K. Chen, S. Hong, and Y. Lai, "A Critical

Review of Battery Thermal Performance and Liquid Based Battery Thermal Management," *Energy Convers. Manag.*, vol. 182, pp. 262–281, 2019, doi: 10.1016/j.enconman.2018.12.051.

[65] S. S. Zhang, K. Xu, and T. R. Jow, "Charge and Discharge Characteristics of a Commercial LiCoO2-Based 18650 Li-Ion Battery," *J. Power Sources*, vol. 160, pp. 1403–1409, 2006, doi: 10.1016/j.jpowsour.2006.03.037.

[66] M. Ouyang, Z. Chu, L. Lu, J. Li, X. Han, X. Feng, and G. Liu, "Low Temperature Aging Mechanism Identification and Lithium Deposition in a Large Format Lithium Iron Phosphate Battery for Different Charge Profiles," *J. Power Sources*, vol. 286, pp. 309–320, 2015, doi: 10.1016/j.jpowsour.2015.03.178.

[67] S. Tippmann, D. Walper, L. Balboa, B. Spier, and W. G. Bessler, "Low-Temperature Charging of Lithium-Ion Cells Part I: Electrochemical Modeling and Experimental Investigation of Degradation Behavior," *J. Power Sources*, vol. 252, pp. 305–316, 2014, doi: 10.1016/j.jpowsour.2013.12.022.

[68] W. Wu, W. Wu, X. Qiu, and S. Wang, "Low-Temperature Reversible Capacity Loss and Aging Mechanism in Lithium-Ion Batteries for Different Discharge Profiles," *Int. J. Energy Res.*, vol. 43, no. 1, pp.

243–253, 2019, doi: 10.1002/er.4257.

[69] T. Zhang, C. Gao, Q. Gao, G. Wang, M. Liu, Y. Guo, C. Xiao, and Y. Y. Yan, "Status and Development of Electric Vehicle Integrated Thermal Management from BTM to HVAC," *Appl. Therm. Eng.*, vol. 88, pp. 398–409, 2015, doi: 10.1016/j.applthermaleng.2015.02.001.

[70] A. A. Pesaran, S. Burch, and M. Keyser, "An Approach for Designing Thermal Management Systems for Electric and Hybrid Vehicle Battery Packs Preprint," *Fourth Veh. Therm. Manag. Syst. Conf. Exhib. 24-27*, no. January, pp. 1–18, 1999.

[71] R. Sabbah, R. Kizilel, J. R. Selman, and S. Al-Hallaj, "Active (Air-Cooled) vs. Passive (Phase Change Material) Thermal Management of High Power Lithium-Ion Packs: Limitation of Temperature Rise and Uniformity of Temperature Distribution," *J. Power Sources*, vol. 182, no. 2, pp. 630–638, 2008, doi: 10.1016/j.jpowsour.2008.03.082.

[72] A. Pesaran, "Battery Thermal Management in EVs and HEVs : Issues and Solutions," *Adv. Automot. Batter. Conf.*, p. 10, 2001.

[73] J. Kim, J. Oh, and H. Lee, "Review on Battery Thermal Management System for Electric Vehicles," *Appl. Therm. Eng.*, vol. 149, no. November 2018, pp. 192–212, 2019, doi: 10.1016/j.applthermaleng.2018.12.020.

[74] S. Wu, R. Xiong, H. Li, V. Nian, and S. Ma, “The State of the Art on Preheating Lithium-Ion Batteries in Cold Weather,” *J. Energy Storage*, vol. 27, no. November 2019, p. 101059, 2020, doi: 10.1016/j.est.2019.101059.

[75] Z. LEI, C. ZHANG, J. LI, G. FAN, and Z. LIN, “Preheating Method of Lithium-Ion Batteries in an Electric Vehicle,” *J. Mod. Power Syst. Clean Energy*, vol. 3, no. 2, pp. 289–296, 2015, doi: 10.1007/s40565-015-0115-1.

[76] M. Malik, I. Dincer, and M. A. Rosen, “Review on Use of Phase Change Materials in Battery Thermal Management for Electric and Hybrid Electric Vehicles,” *International Journal of Energy Research*. 2016. doi: 10.1002/er.3496.

[77] M. Al-Zareer, I. Dincer, and M. A. Rosen, “Novel Thermal Management System Using Boiling Cooling for High-Powered Lithium-Ion Battery Packs for Hybrid Electric Vehicles,” *J. Power Sources*, 2017, doi: 10.1016/j.jpowsour.2017.07.067.

[78] J. Smith, M. Hinterberger, C. Schneider, and J. Koehler, “Energy Savings and Increased Electric Vehicle Range through Improved Battery Thermal Management,” *Appl. Therm. Eng.*, vol. 101, pp. 647–656, 2016, doi: 10.1016/j.applthermaleng.2015.12.034.

[79] S. K. Mohammadian and Y. Zhang, “Thermal Management Optimization of an Air-Cooled Li-Ion Battery Module Using Pin-Fin Heat Sinks for Hybrid Electric Vehicles,” *J. Power Sources*, vol. 273, pp. 431–439, 2015, doi: 10.1016/j.jpowsour.2014.09.110.

[80] H. S. Hamut, I. Dincer, and G. F. Naterer, “Analysis and Optimization of Hybrid Electric Vehicle Thermal Management Systems,” *J. Power Sources*, vol. 247, pp. 643–654, 2014, doi: 10.1016/j.jpowsour.2013.08.131.

[81] R. Bayerer, “Advanced Packaging Yields Higher Performance and Reliability in Power Electronics,” *Microelectron. Reliab.*, vol. 50, no. 9–11, pp. 1715–1719, 2010, doi: 10.1016/j.microrel.2010.07.016.

[82] S. Narumanchi, “Thermal Management of Power Electronics and Electric Motors for Electric-Drive Vehicles,” pp. 1–23, 2014.

[83] S. Waye, “Power Electronics Thermal Management R & D,” no. April, pp. 1–16, 2015.

[84] C. W. Ayers, J. C. Conklin, J. S. Hsu, and K. T. Lowe, “A Unique Approach to Power Electronics and Motor Cooling in a Hybrid Electric Vehicle Environment,” *VPPC 2007 - Proc. 2007 IEEE Veh. Power Propuls. Conf.*, pp. 102–106, 2007, doi: 10.1109/VPPC.2007.4544107.

[85] K. T. Lowe, C. W. Ayers, and J. S. Shu, “Floating Refrigerant Loop Based on R-134a Refrigerant Cooling of High-Heat Flux Electronics,” *Energy*, no. September, p. 16, 2005.

[86] C. W. Ayers, J. S. Hsu, and K. T. Lowe, “Fundamentals of a Floating Loop Concept Based on R134a Refrigerant Cooling of High Heat Flux Electronics,” *Annu. IEEE Semicond. Therm. Meas. Manag. Symp.*, vol. 2006, pp. 59–64, 2006, doi: 10.1109/stherm.2006.1625207.

[87] J. B. Campbell, L. M. Tolbert, C. W. Ayers, B. Ozpineci, and K. T. Lowe, “Two-Phase Cooling Method Using the R134a Refrigerant to Cool Power Electronic Devices,” *IEEE Trans. Ind. Appl.*, vol. 43, no. 3, pp. 648–656, 2007, doi: 10.1109/TIA.2007.895719.

[88] H. Fujita, A. Itoh, and T. Urano, “Newly Developed Motor Cooling Method Using Refrigerant,” *World Electr. Veh. J.*, vol. 10, no. 2, 2019, doi: 10.3390/wevj10020038.

[89] Sunjin Kim, “Study on the Thermal Management of Motor in Electric Vehicle Using Flow Boiling Heat Transfer in Curved Channel,” 곡선 유로에서의 비등 열전달을 이용한 전기자동차용 모터 열관리에 대한 연구. 서울 : 서울대학교 대학원, 서울, 2019. [Online]. Available: http://snu-

primo.hosted.exlibrisgroup.com/82SNU:82SNU_INST21684231670002591

[90] R. Kizilel, R. Sabbah, J. R. Selman, and S. Al-Hallaj, "An Alternative Cooling System to Enhance the Safety of Li-Ion Battery Packs," *J. Power Sources*, vol. 194, no. 2, pp. 1105–1112, 2009, doi: 10.1016/j.jpowsour.2009.06.074.

[91] M. Al-Zareer, I. Dincer, and M. A. Rosen, "Review on Use of Phase Change Materials in Battery Thermal Management for Electric and Hybrid Electric Vehicles," *J. Power Sources*, vol. 363, pp. 291–303, 2017, doi: 10.1016/j.jpowsour.2017.07.067.

[92] J. Sarkar and S. Bhattacharyya, "Application of Graphene and Graphene-Based Materials in Clean Energy-Related Devices Minghui," *Int. J. Energy Res.*, vol. 33, no. 4, pp. 23–40, 2012, doi: 10.1002/er.

[93] S. S. Zhang, K. Xu, and T. R. Jow, "Low-Temperature Performance of Li-Ion Cells with a LiBF4-Based Electrolyte," *J. Solid State Electrochem.*, vol. 7, no. 3, pp. 147–151, 2003, doi: 10.1007/s10008-002-0300-9.

[94] S. S. Zhang, K. Xu, and T. R. Jow, "The Low Temperature Performance of Li-Ion Batteries," *J. Power Sources*, vol. 115, no. 1,

pp. 137–140, 2003, doi: 10.1016/S0378-7753(02)00618-3.

[95] Y. Higuchi, H. Kobayashi, Z. Shan, M. Kuwahara, Y. Endo, and Y. Nakajima, "Efficient Heat Pump System for PHEV/BEV," *SAE Technical Paper Series*. 2017. doi: 10.4271/2017-01-0188.

[96] X. Xu, Y. Hwang, and R. Radermacher, "Refrigerant Injection for Heat Pumping/Air Conditioning Systems: Literature Review and Challenges Discussions," *Int. J. Refrig.*, vol. 34, no. 2, pp. 402–415, 2011, doi: 10.1016/j.ijrefrig.2010.09.015.

[97] X. Wang, Y. Hwang, and R. Radermacher, "Two-Stage Heat Pump System with Vapor-Injected Scroll Compressor Using R410A as a Refrigerant," *Int. J. Refrig.*, 2009, doi: 10.1016/j.ijrefrig.2009.03.004.

[98] Y. Chung and M. S. Kim, "Thermal Analysis and Pack Level Design of Battery Thermal Management System with Liquid Cooling for Electric Vehicles," *Energy Convers. Manag.*, vol. 196, no. February, pp. 105–116, 2019, doi: 10.1016/j.enconman.2019.05.083.

[99] S. Lee, Y. Chung, Y. Jeong, and M. S. Kim, "Experimental Study on an Electric Vehicle Heat Pump System with Multi-Level Waste Heat Recovery Using a Vapor Injection Technique at Low Ambient Temperatures," *Energy Convers. Manag.*, vol. 267, p. 115935, 2022, doi: 10.1016/j.enconman.2022.115935.

[100] C. Arpagaus, F. Bless, J. Schiffmann, and S. S. Bertsch, "Multi-Temperature Heat Pumps: A Literature Review," *Int. J. Refrig.*, vol. 69, pp. 437–465, 2016, doi: 10.1016/j.ijrefrig.2016.05.014.

[101] ANSI/AMCA, "Laboratory Methods of Testing Fans for Certified Aerodynamic Performance Rating," *210-16/ASHRAE*. Air Movement and Control Association, pp. 16–51, 2016.

[102] I. ASHRAE, *2009 ASHRAE handbook: fundamentals*. American Society of Heating, Refrigeration and Air-Conditioning Engineers, 2009.

[103] R. J. Moffat, "Contributions to the Theory of Single-Sample Uncertainty Analysis," *J. Fluids Eng. Trans. ASME*, vol. 104, no. 2, pp. 250–258, 1982, doi: 10.1115/1.3241818.

[104] AHRI, "ANSI/ASHRAE Standard 210/240: Performance Rating of Unitary Air-Conditioning and Air-Source Heat Pump Equipment," *ASHRAE Stand.*, vol. 2, no. Addenda 1 and 2, pp. 1–32, 2008.

[105] Z. Tian, B. Gu, W. Gao, and Y. Zhang, "Performance Evaluation of an Electric Vehicle Thermal Management System with Waste Heat Recovery," *Appl. Therm. Eng.*, vol. 169, 2020, doi: 10.1016/j.applthermaleng.2020.114976.

[106] S. J. 2765, "Procedure for Measuring System COP (Coefficient of

Performance) of a Mobile Air Conditioning System on a Test Bench," vol. 4970, 2008.

[107] "Heatpump System US Patent".

[108] S. Lee, Y. Chung, Y. Jeong, and M. S. Kim, "Investigation on the Performance Enhancement of Electric Vehicle Heat Pump System with Air-to-Air Regenerative Heat Exchanger in Cold Condition," *Sustain. Energy Technol. Assessments*, vol. 50, no. November 2021, p. 101791, 2022, doi: 10.1016/j.seta.2021.101791.

[109] E. W. Lemmon, M. L. Huber, and M. O. Mclinden, "REFPROP 9.1," *NIST Stand. Ref. database*, 2013.

[110] R. E. Sonntag, C. Borgnakke, G. J. Van Wylen, and S. Van Wyk, *Fundamentals of thermodynamics*, vol. 6. Wiley New York, 1998.

[111] Y. J. Chang and C. C. Wang, "A Generalized Heat Transfer Correlation for Louver Fin Geometry," *Int. J. Heat Mass Transf.*, vol. 40, no. 3, pp. 533–544, 1997, doi: 10.1016/0017-9310(96)00116-0.

[112] D. P. D. T.L. Bergman, A. S. Lavine, F. P. Incropera, "Fundamentals of Heat and Mass Transfer," *New York Wiley*, 1996.

[113] M. H. Kim and C. W. Bullard, "Air-Side Thermal Hydraulic Performance of Multi-Louvered Fin Aluminum Heat Exchangers," *Int. J. Refrig.*, vol. 25, no. 3, pp. 390–400, 2002, doi: 10.1016/S0140-

7007(01)00025-1.

[114] Y. Y. Yan and T. F. Lin, "Evaporation Heat Transfer and Pressure Drop of Refrigerant R-134a in a Plate Heat Exchanger," *J. Heat Transfer*, 1999, doi: 10.1115/1.2825924.

[115] Y. Y. Yan, H. C. Lio, and T. F. Lin, "Condensation Heat Transfer and Pressure Drop of Refrigerant R-134a in a Plate Heat Exchanger," *Int. J. Heat Mass Transf.*, vol. 42, no. 6, pp. 993–1006, 1999, doi: 10.1016/S0017-9310(98)00217-8.

[116] J. P. Hartnett and M. Kostic, "Heat Transfer to Newtonian and Non-Newtonian Fluids in Rectangular Ducts," in *Advances in heat transfer*, vol. 19, Elsevier, 1989, pp. 247–356.

[117] G. F. C. Rogers and Y. R. Mayhew, "Heat Transfer and Pressure Loss in Helically Coiled Tubes with Turbulent Flow," *Int. J. Heat Mass Transf.*, vol. 7, no. 11, pp. 1207–1216, 1964, doi: 10.1016/0017-9310(64)90062-6.

[118] W. Cui, L. Li, M. Xin, T. C. Jen, Q. Chen, and Q. Liao, "A Heat Transfer Correlation of Flow Boiling in Micro-Finned Helically Coiled Tube," *Int. J. Heat Mass Transf.*, vol. 49, no. 17–18, pp. 2851–2858, 2006, doi: 10.1016/j.ijheatmasstransfer.2006.02.020.

[119] C. N. Chen, J. T. Han, T. C. Jen, and L. Shao, "Thermo-Chemical

Characteristics of R134a Flow Boiling in Helically Coiled Tubes at Low Mass Flux and Low Pressure,” *Thermochim. Acta*, vol. 512, no. 1–2, pp. 163–169, 2011, doi: 10.1016/j.tca.2010.09.020.

[120] V. V. Viswanathan, D. Choi, D. Wang, W. Xu, S. Towne, R. E. Williford, J. G. Zhang, J. Liu, and Z. Yang, “Effect of Entropy Change of Lithium Intercalation in Cathodes and Anodes on Li-Ion Battery Thermal Management,” *J. Power Sources*, vol. 195, no. 11, pp. 3720–3729, 2010, doi: 10.1016/j.jpowsour.2009.11.103.

[121] P. Moin, *Fundamentals of engineering numerical analysis*. Cambridge University Press, 2010.

[122] H. Martin, “Impinging Jet Flow Heat and Mass Transfer,” *Adv. heat Transf.*, vol. 13, p. 13, 1977.

[123] Y. U. Choi, M. S. Kim, G. T. Kim, M. Kim, and M. S. Kim, “Performance Analysis of Vapor Injection Heat Pump System for Electric Vehicle in Cold Startup Condition,” *Int. J. Refrig.*, vol. 80, pp. 24–36, 2017, doi: 10.1016/j.ijrefrig.2017.04.026.

[124] S. Kakaç, R. K. Shah, and W. Aung, “Handbook of Single-Phase Convective Heat Transfer,” *John Wiley Sons, New York,* 1987.

[125] A. Kharab and R. B. Guenther, *An introduction to numerical methods: A MATLAB® approach, second edition*. 2005.

[126] J. W. MacArthur and E. W. Grald, “Unsteady Compressible Two-Phase Flow Model for Predicting Cyclic Heat Pump Performance and a Comparison with Experimental Data,” *Int. J. Refrig.*, vol. 12, no. 1, pp. 29–41, 1989, doi: 10.1016/0140-7007(89)90009-1.

[127] C.-W. Shu and R. J. LeVeque, *Numerical Methods for Conservation Laws.*, vol. 57, no. 196. 1991. doi: 10.2307/2938728.

[128] M. M. Shah, “A General Correlation for Heat Transfer during Film Condensation inside Pipes,” *Int. J. Heat Mass Transf.*, vol. 22, no. 4, pp. 547–556, 1979, doi: 10.1016/0017-9310(79)90058-9.

[129] W. M. Kays and A. L. London, “Compact Heat Exchangers,” 1984.

[130] V. Gnielinski, “New Equations for Heat and Mass Transfer in Turbulent Pipe and Channel Flow,” *Int. Chem. Eng.*, vol. 16, no. 2, pp. 359–368, 1976.

[131] S. Kim, “Study on the Thermal Management of Motor in Electric Vehicle Using Flow Boiling Heat Transfer in Curved Channel,” 2019.

[132] J. Jung, Y. Jeon, H. Lee, and Y. Kim, “Numerical Study of the Effects of Injection-Port Design on the Heating Performance of an R134a Heat Pump with Vapor Injection Used in Electric Vehicles,” *Appl. Therm. Eng.*, vol. 127, pp. 800–811, 2017, doi: 10.1016/j.applthermaleng.2017.08.098.

[133] D. Kim, H. J. Chung, Y. Jeon, D. S. Jang, and Y. Kim, "Optimization of the Injection-Port Geometries of a Vapor Injection Scroll Compressor Based on SCOP under Various Climatic Conditions," *Energy*, vol. 135, pp. 442–454, 2017, doi: 10.1016/j.energy.2017.06.153.

[134] H. Sun, H. Hu, J. Wu, G. Ding, G. Li, C. Wu, X. Wang, and Z. Lv, "A Theory-Based Explicit Calculation Model for Variable Speed Scroll Compressors with Vapor Injection," *Int. J. Refrig.*, vol. 88, pp. 402–412, 2018, doi: 10.1016/j.ijrefrig.2018.01.016.

[135] F. M. Tello-Oquendo, E. Navarro-Peris, F. Barceló-Ruescas, and J. Gonzálvez-Maciá, "Semi-Empirical Model of Scroll Compressors and Its Extension to Describe Vapor-Injection Compressors. Model Description and Experimental Validation," *Int. J. Refrig.*, vol. 106, pp. 308–326, 2019, doi: 10.1016/j.ijrefrig.2019.06.031.

[136] Y. Yu, M. Chen, S. Zaman, S. Xing, M. Wang, and H. Wang, "Thermal Management System for Liquid-Cooling PEMFC Stack: From Primary Configuration to System Control Strategy," *eTransportation*, vol. 12, p. 100165, 2022, doi: 10.1016/j.etran.2022.100165.

[137] J. Jiang, H. Ruan, B. Sun, W. Zhang, W. Gao, L. Y. Wang, and L.

Zhang, “A Reduced Low-Temperature Electro-Thermal Coupled Model for Lithium-Ion Batteries,” *Appl. Energy*, vol. 177, pp. 804–816, 2016, doi: 10.1016/j.apenergy.2016.05.153.

[138] M. Alipour, E. Esen, A. R. Varzeghani, and R. Kizilel, “Performance of High Capacity Li-Ion Pouch Cells over Wide Range of Operating Temperatures and Discharge Rates,” *J. Electroanal. Chem.*, vol. 860, p. 113903, 2020, doi: 10.1016/j.jelechem.2020.113903.

[139] S. K. Kumar, A. A. B. M. Abduh, O. Sabih, and R. Yazami, “Temperature Effect on ‘Ragone Plots’ of Lithium-Ion Batteries,” *J. Electrochem. Soc.*, vol. 165, no. 3, pp. A674–A679, 2018, doi: 10.1149/2.0591803jes.

[140] Y. WANG, J. DONG, S. JIA, and L. HUANG, “Experimental Comparison of R744 and R134a Heat Pump Systems for Electric Vehicle Application,” *Int. J. Refrig.*, vol. 121, pp. 10–22, 2021, doi: 10.1016/j.ijrefrig.2020.10.026.

[141] B. Pattipati, B. Balasingam, G. V. Avvari, K. R. Pattipati, and Y. Bar-Shalom, “Open Circuit Voltage Characterization of Lithium-Ion Batteries,” *J. Power Sources*, vol. 269, pp. 317–333, 2014, doi: 10.1016/j.jpowsour.2014.06.152.

[142] S. Khanmohammadi, S. Ghaemi, and F. Samadi, “Research on SOC

Estimation Based on Room-Temperature SOC-OCV Curve and Capacity Normalization for Li-Ion Batteries," *DEStech Trans. Environ. Energy Earth Sci.*, 2018.

[143] V. H. Duong, H. A. Bastawrous, and K. W. See, "Accurate Approach to the Temperature Effect on State of Charge Estimation in the LiFePO4 Battery under Dynamic Load Operation," *Appl. Energy*, vol. 204, pp. 560–571, 2017, doi: 10.1016/j.apenergy.2017.07.056.

[144] S. Lee, Y. Chung, S. Kim, Y. Jeong, and M. S. Kim, "Predictive Optimization Method for the Waste Heat Recovery Strategy in an Electric Vehicle Heat Pump System," *Appl. Energy*, vol. 333, p. 120572, 2023, doi: 10.1016/j.apenergy.2022.120572.

[145] S. Lee, Y. Jeong, I. Hwang, and M. S. Kim, "Optimization of Injection-Port Design for Multi-Level Waste Heat Recovery in an Electric Vehicle Heat Pump System," *Appl. Therm. Eng.*, p. 119970, 2023.

[146] S. Lee, Y. Chung, Y. Il, Y. Jeong, and M. Soo, "Battery Thermal Management Strategy Utilizing a Secondary Heat Pump in Electric Vehicle under Cold-Start Conditions," *Energy*, vol. 269, no. January, p. 126827, 2023, doi: 10.1016/j.energy.2023.126827.

국문 초록

국제적으로 많은 국가에서 차량의 이산화탄소 발생량이나 연비를 규제함에 따라, 전기자동차가 차세대 친환경 차량으로 많은 주목을 받고 있다. 하지만 전기차는 겨울철 주행 시 차량 실내의 난방을 위한 추가적인 에너지 소모와 리튬 이온 배터리의 낮은 성능으로 인하여 주행거리가 감소하는 문제가 발생한다. 이에 따라, 히트펌프가 기존 전기 히터를 대신하는 효율적인 난방 기구로 폭넓게 적용되고 있다. 그러나 히트펌프 역시 극저온 구간에서 성능이 크게 감소하는 경향이 있기에, 전장품으로부터 발생하는 미활용열을 회수하여 부족한 실내 난방부하를 보충할 필요가 있다. 본 연구에서는 미활용열을 흡수하는 온도 레벨을 세분화하여 활용하는 다중 레벨 열관리 시스템을 제시하였다.

첫째로, 온도 레벨이 히트펌프에 미치는 영향을 분석하였다. 기상 냉매 중간주입 기술을 활용할 경우 미활용열을 중간 온도 레벨에서 회수할 수 있다. 냉매가 중간 온도 대역에서 미활용열을 흡수함에 따라 더 큰 난방용량을 확보할 수 있다. 미활용열이 없는 방식, 미활용열을 저온에서 회수하는 방식, 미활용열을 중간 온도 레벨에서 회수하는 방식에 대해 실험연구가 진행되었다. 각 방식은 외기 온도, 압축기 속도, 미활용열의 양을 포함한 다양한 조건에서

평가되었다. 실험 결과, 중간온도 레벨에서 미활용열을 회수하는 방식이 저온에서 회수하는 방식보다 72% 높은 난방용량을 확보할 수 있는 것을 확인하였다. 마찬가지로, 미활용열을 고온에서 회수하는 방식 역시 평가되었다. 플로팅 루프는 모터와 전력기기의 열관리에 응축기 후단의 액상 냉매를 활용한다. 이를 통해 겨울철 미활용열 회수와 여름철 열관리를 용이하게 할 수 있으며 이는 2상 냉매의 우수한 열전달 특성 때문이다. 제안된 시스템의 성능을 입증하기 위하여 히트펌프와 전장품 해석 모델을 개발하고 통합하였다. 해석 결과, 플로팅 루프를 활용한 시스템의 전력 소모가 겨울철에는 27.7% 여름철에는 5.8% 감소한 것을 확인하였다.

둘째로, 다중 레벨 열관리 시스템을 냉시동 조건에서 평가하였다. 앞선 연구결과에서 알 수 있듯이, 열 회수 온도는 성능에 큰 영향을 미친다. 하지만 일반적인 미활용열 회수는 한 온도 레벨만을 활용하고 이는 운행 조건에 따라 달라지는 최적 온도 레벨을 활용할 수 없다. 본 연구에서는 열 회수 레벨을 저온, 중온, 고온의 세 온도 레벨로 세분화하고 각 온도에서의 열 회수 성능을 평가하였다. 히트펌프의 동적 거동을 반영하기 위하여 실험이 진행되었고, 이를 바탕으로 히트펌프 동적 모델을 수립하였다. 전장품 동적 모델과 히트펌프 동적 모델을 통합하여 통합 열관리 모델을 구성하였다. 해당 모델을 활용하여 다양한 냉시동 조건에서

미활용열 회수 전략을 평가하였다. 평가 결과, 최적의 미활용열 회수 온도를 활용할 경우 일반적인 열 회수 전략에 비해 13%의 소모동력 절감 효과를 나타내는 것을 확인하였다.

세번째로, 다중 레벨 미활용열 회수 전략의 경우 기상 냉매 주입 기술을 활용하기에, 주입 포트의 디자인이 성능에 크게 영향을 미친다. 하지만 현재의 포트 디자인은 기액분리기나 내부 열교환기를 활용한 주입 시스템에 최적화되어 설계되었다. 기상 냉매 주입 과정을 정확하게 모사하기 위하여 새로운 주입 모델이 개발되었다. 위 모델은 압축 챔버 내의 압력 증가와 제트 충돌 거동을 반영하였다. 본 주입 모델을 포함한 스크롤 압축기 모델을 바탕으로 히트펌프 시스템이 분석되었고, 포트의 크기와 위치에 따른 시스템의 성능을 평가하였다. 평가 결과, 최적의 포트는 2mm 반경을 가진 듀얼 포트이고 위치는 600°로 나타났다.

마지막으로, 배터리 승온 전략이 제시되었다. 전기자동차의 에너지 저장 시스템이 저온에서 작동할 경우, 내부저항의 증가로 출력과 용량이 크게 감소한다. 따라서 이로 인한 주행거리 감소를 방지하기 위해서는 적절한 열관리가 필요하다. 최적의 배터리 열관리 전략을 도출하기 위해서는 배터리 승온을 통한 성능 향상과 승온을 위해 소비되는 에너지를 시스템 측면에서 고려해야 한다. 팩 단위의 배터리 열모델과 셀 단위의 배터리 성능 모델을 통합한

배터리 모델을 개발하였고 이를 히트펌프 모델과 결합하였다. 위 모델을 통해 배터리 승온, 자가 발열, 배터리 흡열 세가지 전략을 비교하였다. 비교 결과 저온 구간에서의 배터리 승온을 통해 최대 18.8%의 주행거리를 추가로 확보할 수 있었고, 히트펌프를 활용하여 배터리 예열을 할 경우 동일한 예열 성능을 38.4% 적은 에너지 소모로 구현할 수 있었다.

저자는 본 연구를 바탕으로 다중 레벨 열관리 시스템이 보급되어 전기차의 주행거리 문제의 해결에 기여하는 것을 기대한다.

주요어: 전기자동차, 통합열관리 시스템, 기상 냉매 중간주입, 온도 세분화, 다중 레벨 히트펌프, 미활용열 회수, 용량 증대, 냉시동

학 번: 2018-28030